6-2014

Star Formation in the NGC 5846 Group of Galaxies

Lucas Viani
Union College - Schenectady, NY

Star Formation in the NGC 5846 Group of Galaxies

By

Lucas Viani

****

Submitted in partial fulfillment

of the requirements for

Honors in the Department of Physics and Astronomy

UNION COLLEGE

June, 2014

ABSTRACT

VIANI, LUCAS Star formation in the NGC 5846 Group of Galaxies. Department of Physics and Astronomy, June 2014.

ADVISOR: KOOPMANN, REBECCA

Environmental interactions in groups and clusters of galaxies are thought to alter the evolution of member galaxies. The goal of this research was to analyze gas and star formation properties of galaxies in the NGC 5846 group. A sample of group galaxies was observed at CTIO (Cerro Tololo Inter-American Observatory in Chile) and KPNO (Kitt Peak National Observatory) using broadband red (R) and narrowband hydrogen emission line (Hα) filters. The images were reduced and analyzed to extract star formation rates and distributions. Neutral hydrogen data from the Arecibo Legacy Fast ALFA (ALFALFA) survey were used to measure the cold neutral gas content, which provides the raw material for star formation. The amounts and extents of star formation in the sample galaxies are compared as a function of cold gas content, galaxy type, and position in the group and compared to those of galaxies located in other environments. Of the NGC 5846 galaxies sampled using the wide-field MOSAIC camera at KPNO, 32% had Hα emission detected. The star-forming galaxies in the NGC 5846 group show a range of star formation rates, with a number that have lower mean star formation rates and gas content compared to isolated galaxies, but also a few that show enhanced star formation. Truncated star formation similar to that of galaxies in the Virgo Cluster is seen in several NGC 5846 galaxies. These results indicate the possibility of environmental interactions in this intermediate density group environment.

1. Introduction

1.1. Galaxy Morphology

Galaxies in the universe are far from uniform, exhibiting a wide variety of traits, structures, and properties. In order to make sense of the wide variety of different galaxy types, it can be useful to group galaxies together based on their characteristics (such as size, shape, mass, brightness, etc.). The study of galaxy morphology can be very useful in examining galaxy evolution, interactions, and environmental effects.

The classic Hubble classification scheme divided galaxies into 4 main types: elliptical, spiral, lenticular, and irregular (Hubble 1926). Figure 1 shows Hubble's original classification system for ellipticals, lenticulars, and spirals. Elliptical galaxies do not contain much gas and dust and therefore have fewer young stars. Spiral galaxies consist of a central bulge (which lacks gas and dust) and spiral arms containing gas, dust, and the areas of star formation. The third type, lenticular or S0 galaxies, do not have spiral arms but have a central bulge and faint disk. The fourth type, called irregular, include galaxies that do not fit into the other categories. Within these 4 categories galaxies are further divided by structural parameters such as ellipticity, size of central bulge, tightness of any spiral arms, and dynamical differences. Classically, elliptical galaxies are called "early type" and spiral galaxies are referred to as "late type" because of their locations on the Hubble tuning fork diagram.

Hubble's classification system has been modified as time progressed. Many of the "irregular" galaxies are actually members of one of the other groups that are experiencing changes, such as environmental interactions (like tidal interactions), thus making them less recognizable. Other irregulars are low mass galaxies. Low mass galaxies are now known to be the most populous type in the Universe. They are

classified into dwarf ellipticals (dE), dwarf spheroidal (dSph), and dwarf irregular (dI).

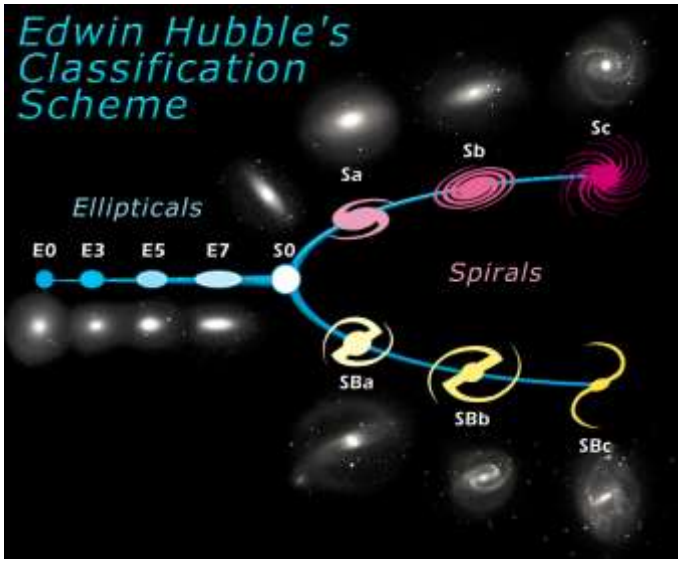

Figure 1: *Diagram illustrating the Hubble tuning fork. Galaxies on the left are referred to as "early type" while galaxies on the right are "late type" galaxies*. *(Image from* cas.sdss.org).

There are many theories as to why this variety of galaxy types exists. For example, there is debate whether different types of galaxies form in different ways or whether all galaxies form in generally the same way and then their surrounding environments dictate their morphological evolution (the nature vs. nurture debate). Galaxy evolution, and the wide variety of galaxy types, is probably the result of a mix of these two theories. As a result, studying the effects of the environment on galaxy evolution is a promising method to better understand the reasons why different morphologies exist and why (or if) galaxy types evolve over time.

1.2. Galaxy Environments and Environmental Interactions

Just as there are a wide variety of galaxy morphologies, so are there a wide variety of environments in which a galaxy can exist. The term "environment" generally refers to the relative number density of galaxies in the region. The most dense regions, clusters, contain hundreds to thousands of galaxies. Galaxies in the least dense regions of

space are referred to as isolated. Galaxy groups, containing tens to hundreds of galaxies, have densities between those of clusters and isolated galaxies.

Studies have found correlations between the density of galaxies and the distribution of the types of galaxies in that environment. As can be seen in Figure 2, denser regions have more elliptical and S0 type galaxies while having fewer spiral galaxies (Dressler 1980). Figure 2 (from Dressler 1980) also shows that in less dense regions spiral galaxies dominate over S0 and elliptical galaxies.

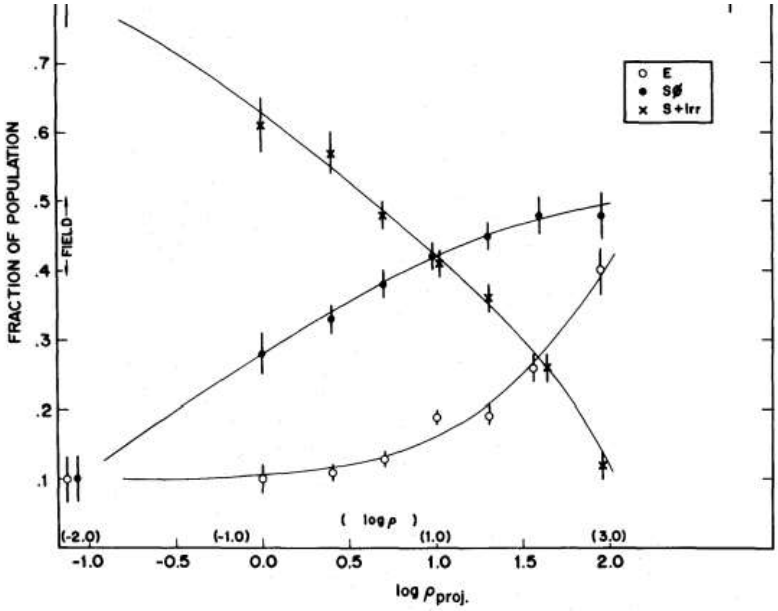

Figure 2: *The galaxy morphology-density relationship is illustrated. Denser environments have more elliptical and S0 type galaxies while less dense regions have more spiral type galaxies. (Figure from Dressler 1980).*

While galaxies may appear to be isolated systems and independent from one another, in reality interactions between galaxies play a key role in galaxy structure and evolution. Galaxy interactions include events such as tidal interactions and mergers, as well as interactions between galaxies and the environment, such as ram pressure stripping. Through the study of how galaxies interact with their environment and the effects that different environments have on galaxies, galaxy evolution and structure can

be better understood.

One type of environmental interaction is due to gravitational forces between two (or more) galaxies. In these interactions, the gravitational force resulting from the proximity of another galaxy can rearrange a galaxy's stars and gas. This can lead to the formation of tails of gas and stars (e.g., Toomre & Toomre 1972). The relative velocities of the interacting galaxies affect the gravitational strength of the interaction. Since the gravitational force takes time to act, galaxies moving past each other at high relative velocities experience less disruption while galaxies moving slowly relative to each other will experience a stronger gravitational effect. Therefore, tidal interactions are expected to be of more importance in less dense environments (Boselli & Gavazzi 2006). This is because in dense clusters, galaxies orbit the center of mass at higher speeds. In more isolated, less dense regions, where galaxies move slower, tidal interactions have a larger impact.

In the cluster and group environments, interactions with hot intracluster and intragroup media can also play a significant role in shaping galaxy evolution. As galaxies in clusters orbit the center of mass, they move through the hot intracluster medium (ICM). The ICM is a hot gas (10^7-10^8 K) heated by the strong gravitational forces due to the cluster's high mass. The process of moving through the ICM causes a pressure on the gas in the galaxy that takes the form:

$$P_{ram} \approx \rho_{ICM} * v^2,$$

where P_{ram} is the pressure on the galaxy that causes ram pressure stripping, ρ_{ICM} is the density of the intracluster medium, and v is the galaxy's velocity relative to the ICM (Gunn & Gott 1972). When this force overwhelms the gravitational force binding the

galaxy's gas, the gas is stripped from the galaxy. The galaxy's outer gas (which is more loosely bound) can be stripped off of the galaxy first, resulting in a "bow-shock" shape (as shown in Figure 3).

Another phenomenon, known as galaxy starvation, can also arise in interactions with the ICM. Over the history of a galaxy, loosely bound gas gradually falls in and provides fresh material for star formation. A galaxy traveling in even low density regions of the ICM or ISM, however, will lose this gas and cease star formation. This process can take on the order of gigayears (Larson et al. 1980).

Understanding the difference between galaxy environments is critical because the effects of each environment are not identical. For example, in less dense regions tidal interactions dominate while in denser regions the ICM makes ram pressure stripping more dominant. The wide range of effects arising due to interactions between galaxies and their environments is what makes the study of intermediate galaxy groups of such interest. While there is a great deal of understanding regarding the ICM environmental effects in dense clusters and the effects of tidal interactions on galaxies in environments where the ICM plays less of a role, the intermediate group density is much less understood. By examining groups we can determine if the group environment affects galaxy evolution in a manner more similar to the cluster environment or the isolated environment.

1.3. Effects of Environment on Star Formation

As discussed in Section 1.2, ram pressure stripping and interactions with the ICM can cause the stripping and truncation of HI gas in cluster galaxies. An example of the effects of ram pressure stripping can be seen in Figure 3. Figure 3 shows an optical (R)

image of NGC 4522 with HI contours over-plotted. NGC 4522, a member of the Virgo Cluster, has undergone ram pressure stripping and the HI gas exhibits the classic "bow shock" shape.

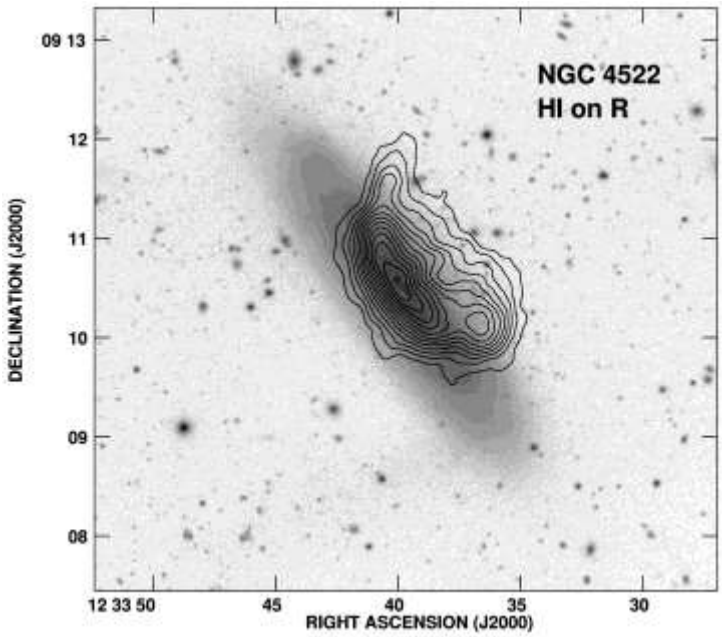

Figure 3: *HI contours on top of greyscale optical image show the removal of the gas via ram pressure stripping in NGC 4522, a galaxy in the Virgo Cluster. The resulting "bow-shock" shape in the HI gas is typical of ram pressure stripping. Note that the stars are undisturbed. Figure from Kenney et al. (2004).*

Since the HI gas being stripped from the galaxy is the raw material needed for star formation, its removal can cause truncation of a galaxy's star forming disk (Kenney et al. 2004; Boselli & Gavazzi 2006). Studies, for example Giovanelli & Haynes (1985) and Gavazzi (1987, 1989) found that galaxies in clusters had less HI than isolated samples (and therefore less material for future star formation).

There have been many studies regarding the star formation of galaxies in dense environments, such as clusters. For example, using Hα luminosities, Koopmann & Kenney (2004) and Kennicutt (1983) demonstrated that less star formation occurs in Virgo galaxies than in isolated galaxies. Truncation of star formation disks is seen much

more frequently in clusters than isolated galaxies. Koopmann & Kenny (2004) showed that 52 percent of Virgo galaxies had truncated Hα disks while this truncation only occurred in 12 percent of isolated galaxies. This supports the theory that environmental effects (such as ram pressure stripping due to the ICM) have influenced the evolution of Virgo Cluster galaxies. It is important to make the distinction between overall star formation rate and truncation of the star forming disk. Truncation means that the extent of the star forming disk is reduced and less than the optical radius, while star formation rate is referring to the amount of new stellar mass produced over time. Total star formation in a galaxy could be reduced over the whole disk or just in certain areas of the disk.

While many studies of this type have been performed on dense clusters, groups of galaxies are less well-studied. In less massive groups, member galaxies move slower than clusters of galaxies and there is less intergalactic medium (IGM). Therefore, we would expect that ram pressure stripping is less important in the group environment while tidal interactions play a larger role.

Several studies examining the relationship between environmental effects and star formation in galaxy groups have been conducted. Hunter & Elmegreen (2004) investigated 94 irregular galaxies and concluded that there was no relationship between star formation and the distance to neighboring galaxies. Cote et al. (2009) determine that star formation rates for dI group galaxies "do not depend on local environment" and the study found no link between the star formation rates of dI group galaxies and the distance to the group center. A non-correlation between distance from cluster center and Hα content was also found by Gavazzi et al. (1998) when studying the Coma and A1367

Clusters (See Figure 4).

Results of the Cote et al. (2009) study did however show that star formation rates of the Centaurus A group dI galaxies are less than the rates found in isolated dI's. Also, the Cote et al. (2009) study found that the Centaurus A, Sculptor, and Local groups had a morphology-density relationship, where dEs and dSphs were more likely to be closer to large group members while dIs were more commonly farther away from large galaxies.

1.4 The Undergraduate ALFALFA Team and NGC 5846 Galaxy Group

This question regarding how the intermediate group density effects star formation, gas distribution, and galaxy evolution has played a large role in motivating the Undergraduate ALFALFA Team (UAT) research. The UAT project is a collaborative effort among 19 universities involving the Arecibo Fast Legacy ALFA Survey (ALFALFA) for neutral hydrogen (Giovanelli et al. 2005). In this collaboration are several projects involving star formation and galaxy groups, as follow up studies to the ALFALFA survey.

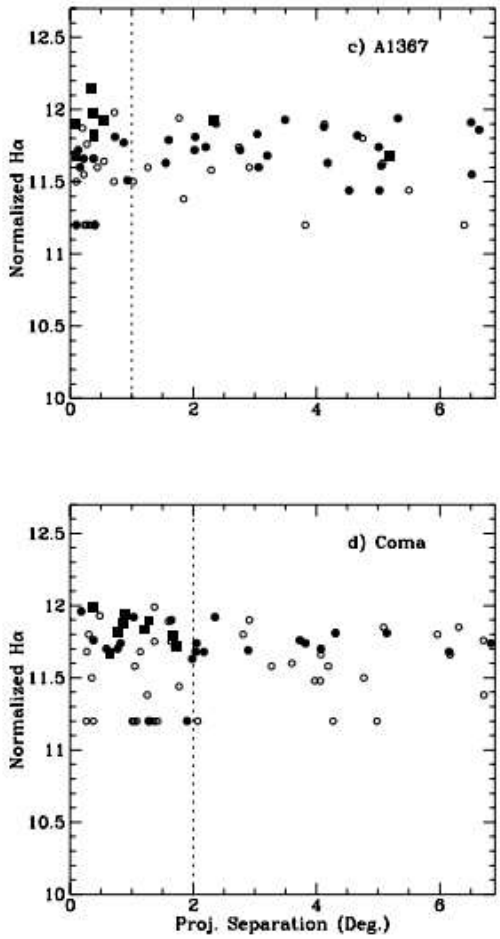

Figure 4: *The above graph shows the amount of normalized Hα emission in a galaxy as a function of angular distance from the center of the cluster. The upper panel investigates the A1367 cluster while the Coma cluster is shown in the lower panel. The dashed line indicates the extent of the cluster. Figure from Gavazzi et al. (1998).*

This thesis focuses on the NGC 5846 galaxy group, a well-defined, relatively isolated group in the Local Super cluster, located 26.1 Mpc (85 million light years) away. It is a high density, intermediate mass system containing over 300 members with a velocity dispersion of 322 km/s (Mahdavi et al. 2005). NGC 5846 contains an early-type rich population similar to the Fornax and Virgo clusters (Mahdavi et al. 2005). Determination of NGC 5846 group members was based on examining a histogram of galaxy velocities and selecting galaxies within a velocity range corresponding to the group. The X-ray center of the group, determined using the Archive of Chandra Cluster

Entropy Profile Tables (ACCEPT), is at a right ascension of 226.6208 degrees and a declination of 1.6056 degrees.

Due to its intermediate density, NGC 5846 can provide valuable information on how the group environment can affect galaxy evolution and star formation. The examination of NGC 5846 can help us understand if the environmental interactions observed in galaxy clusters are also occurring in galaxy groups.

In Section 3 the NGC 5846 group galaxies will be compared to galaxies in a number of different environments, among them another group, the Centaurus A group. Compared to the Centaurus A group (located at 3.9 Mpc away), the NGC 5846 is farther away (Cote et al. 2009). Centaurus A has around 50 known dwarf members (Cote et al. 2009; Karachentsev et al. 2007). The velocity dispersion of Centaurus A, 114±21 km/s, is less that the velocity dispersion of NGC 5846 (van den Bergh 2000).

1.5. Hα Imaging as a Tracer of Star Formation and Indicator of Environmental Effects

A useful tool for the study of star formation, and therefore also the study of environmental effects, is Hα imaging. Hα emission (at a wavelength of 656.28 nm) is produced when the electron in hydrogen falls from the n=3 to the n=2 excited state. This emission, as well as many other recombination emission lines, is produced when massive and hot O and B stars ionize nearby HI gas and the hydrogen atoms recombine. These stars only live up to about 10 million years, and therefore, the detection of Hα emission means a recent star formation event. It has been found that there is a strong connection between Hα produced in star formation regions in a galaxy and the amount of new stars created (Kennicutt 1998).

Maps of Hα and therefore star formation may be produced by obtaining two

images: one in a broad band red (R) filter and one in a narrow band filter centered on the (redshifted) Hα wavelength. The Hα images are corrected for the presence of stellar continuum light by scaling and subtracting the light from the broadband R filter.

Hα patterns can reveal important information about the location of recent star formation in galaxies. As well as providing information regarding the raw star formation rate, Hα imaging allows for investigation into the structure and radial dependence of star formation in a galaxy. The amount of Hα can also be compared to the HI content to estimate how long star formation can be sustained in a galaxy. In addition, Hα can be useful in examining environmental effects on star formation and galaxy behavior. The examination of Hα intensities, distributions, and asymmetries can reveal information about potential past environmental interactions.

1.6. Brief Outline of Thesis

In Section 2 the observational data are described, detail is given about the fields of NGC 5846 that have been observed and the galaxies within them. The CCD reduction process, continuum subtraction method, and preparation for photometry are detailed as well. Section 3 presents the results of the photometry and the star formation rate calculations, provides the broadband R and Hα continuum subtracted images, radial profiles, and compares the NGC 5846 star formation properties to other galaxies and environments. In addition, Section 3.7 provides a brief look at experimenting with different stacking methods for CCD reduction. Section 4 gives a summary of conclusions drawn from the analysis.

2. Observations and Image Reductions

2.1. NGC 5846 Field

Figure 5 shows the portions of the NGC 5846 group that we have imaged. We

have data for the 4 fields nearest the center (some of which were obtained during an observing run I participated in at Kitt Peak in 2012). The reduction procedure I describe pertains to the southernmost field (the highlighted field in Figure 5) and will be referred to as Field 4 from here on. I also combined these data with data from the other 3 fields for analysis. Images were obtained using the CTIO SMARTS 0.9-m telescope and the WYIN 0.9-m telescope (with MOSAIC CCD) at Kitt Peak National Observatory in Arizona in April 2011 and 2012 (Field 4 was imaged in April 2012). Note that for the SMARTS images we targeted HI-detected galaxies while the KPNO images were taken over a wide field and are therefore less biased in galaxy selection. The KPNO fields were imaged using the broad band R Harris filter (central wavelength of 651.354 nm and FWHM of 151.13 nm) and the narrow band Hα filter (central wavelength of 662.052 nm and FWHM of 8.048 nm). Two [NII] lines at wavelengths 654.81 nm and 658.38 nm are within the bandpass of the Hα filter (Koopmann, Kenney, & Young 2001). These data are then combined with data from several previous studies by Union College colleagues O'Brien, Darling, Warrener, and Dr. Koopmann.

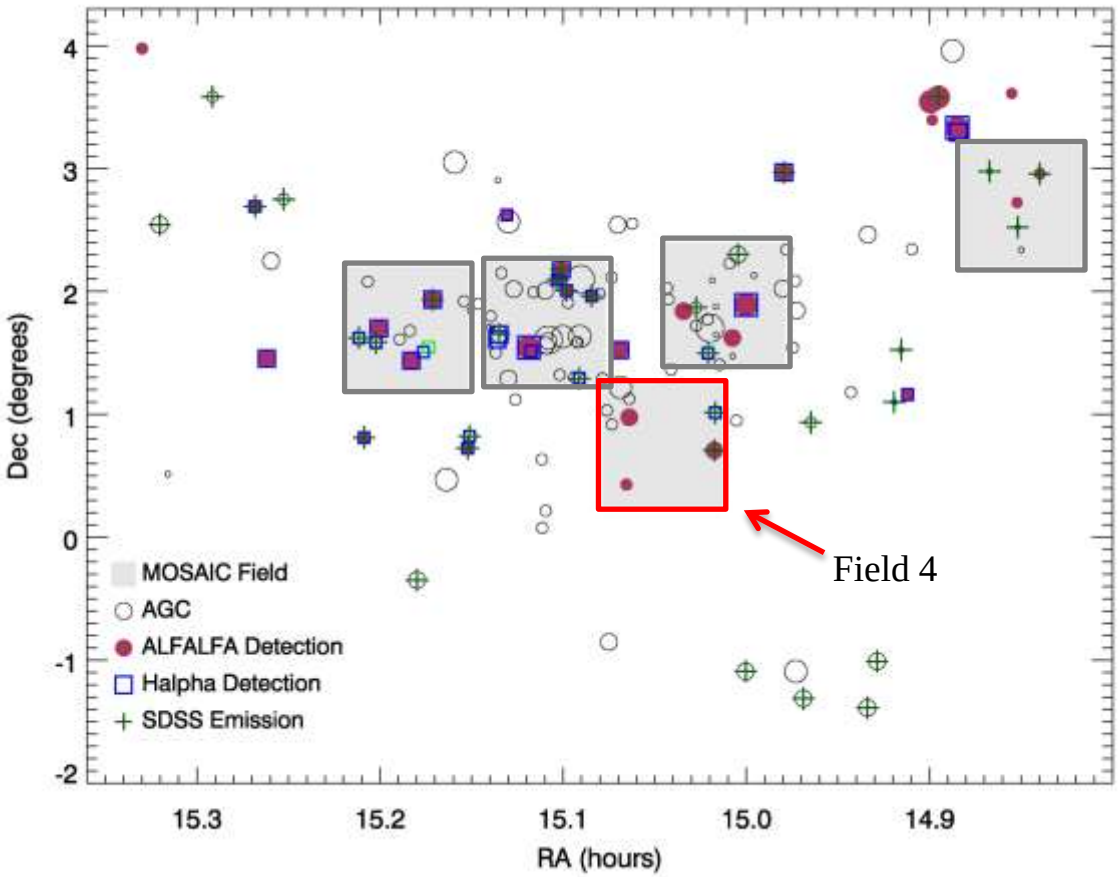

Figure 5: *The shaded grey squares show the regions of the NGC 5846 group that have been imaged. The central, highlighted red field is the data set worked with for this project (Field 4).*

To get a better sense of where our sample of NGC 5846 galaxies are in relation to other NGC 5846 members, see Figure 6. Figure 6 shows the right ascension and declination for other NGC 5846 galaxies (blue) and our sample (red). The main group area (the central region of the group) is circled in green in Figure 6.

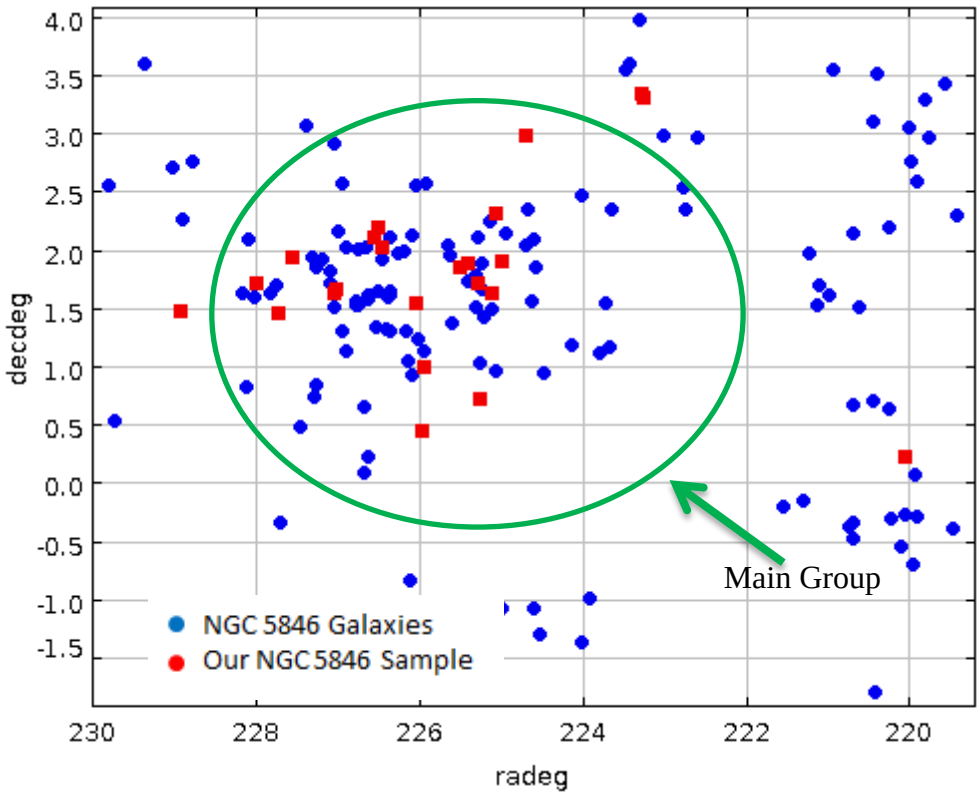

Figure 6: *The right ascension and declination of the NGC 5846 group galaxies are shown. The blue circles represent all group members while the red squares show the coordinates of the NGC 5846 sample observed and analyzed in this paper. The green oval indicates the central main group region.*

The imaging of the field was performed using dithers. This means that 5 images were taken in each filter (R and Hα) and that the images were offset (not centered on the same point). This offset removes the gaps between the MOSAIC image's chips when the different dithers are stacked (as explained in Section 2.2). Table 1 displays the information about each of the dither images (as well as the final stacked image), including seeing, exposure time, and airmass. Note that the seeing degraded significantly during the last R and Hα dither set

Field 4 contained 9 catalogued members of the NGC 5846 group. Table 2 provides a list of the galaxies in the field, their right ascension and declination coordinates, galaxy type, exposure time, airmass, seeing, and whether they had Hα

emission.

Of the 9 galaxies observed in the field, 3 were detected in Hα. These observations were combined with observations from the other 4 fields of NGC 5846 group that had previously been reduced by O'Brien, Darling, Warrener, Dr. Koopmann, and myself. Table 3 lists information about the galaxies in this combined sample that have Hα emission. Since we are investigating star formation, from this point on we will only be using the galaxies in our sample that had detected Hα emission.

Dither	**Filter**	**Seeing (arcsec) (FWHM)**	**Exposure Time (sec)**	**Airmass**
1	**R**	**2.7**	**180**	**1.27**
2	**R**	**2.4**	**180**	**1.38**
3	**R**	**2.3**	**180**	**1.39**
4	**R**	**2.6**	**180**	**1.26**
5	**R**	**3.9**	**180**	**1.46**
Stacked R Image	**R**	**4.7**	**180**	**1.26**
1	**Hα**	**2.5**	**960**	**1.31**
2	**Hα**	**2.4**	**960**	**1.36**
3	**Hα**	**3.7**	**1200**	**1.40**
4	**Hα**	**2.7**	**960**	**1.24**
5	**Hα**	**4.8**	**960**	**1.54**
Stacked Hα Image	**Hα**	**4.7**	**960**	**1.24**

Table 1: *List of dither images and the final stacked images with filter, seeing, exposure time, and airmass provide for each.*

Galaxy	**RA (hours, min, sec)**	**Dec (degrees, arcmin, arcsec)**	**Type**	**Exposure Time (seconds)**		**Airmass**		**Seeing (arcsec)**	**Hα Present?**
				R	**Hα**	**R**	**Hα**		
ACG 252423	**15 04 42.70**	**+01 17 27.00**	**dE**	**180**	**960**	**1.26**	**1.24**	**4.7**	**No**
ACG 9678	**15 04 07.001**	**+01 13 11.00**	**E3**	**180**	**960**	**1.26**	**1.24**	**4.7**	**No**
ACG 253934	**15 04 34.299**	**+01 01 57.00**	**dE**	**180**	**960**	**1.26**	**1.24**	**4.8**	**No**
ACG 253933	**15 04 28.800**	**+00 55 06.00**	**dE**	**180**	**960**	**1.26**	**1.24**	**4.5**	**No**
ACG 252422	**15 03 50.302**	**+01 07 35.99**	**E**	**180**	**960**	**1.26**	**1.24**	**4.7**	**No**
ACG 252211	**15 03 49.899**	**+00 58 37.00**	**dI**	**180**	**960**	**1.26**	**1.24**	**4.7**	**Yes**

ACG 252519	**15 03 55.704**	**+00 25 44.00**	**Irr**	**180**	**960**	**1.26**	**1.24**	**4.8**	**Yes**
ACG 253623	**15 01 00.897**	**+01 00 49.99**	**dE**	**180**	**960**	**1.26**	**1.24**	**4.8**	**No**
ACG 241031	**15 01 3.101**	**+00 42 26.99**	**SAB m**	**180**	**960**	**1.26**	**1.24**	**4.9**	**Yes**

Table 2: *Information about the 9 NGC 5846 galaxies in Field 4 is given. Each galaxy's right ascension and declination positions, the galaxy type, exposure time, airmass, and seeing is presented.*

Galaxy AGC Number	Date	Telescope/CCD	RA (deg)	Dec (deg)	Type	Airmass		Seeing (FWHM) (arcsec)	Exposure Time (sec)	
						R	Hα		R	Hα
9746	04/04/2011	KPNO/MOSAIC	227.56876	1.93361	Sbc	1.19	1.21	3.2	120	900
9751	04/04/2011	KPNO/MOSAIC	227.74333	1.4375	Scd	1.19	1.21	3.1	120	900
9760	04/04/2011	KPNO/MOSAIC	228.00958	1.69833	Sd	1.19	1.21	3.2	120	900
252399	04/04/2011	KPNO/MOSAIC	226.54666	2.09528	Sd	1.41	1.32	5.4	180	1200
250105	04/04/2011	KPNO/MOSAIC	227.03876	1.60889	Sbc	1.41	1.32	5.3	180	1200
250103	04/04/2011	KPNO/MOSAIC	227.02415	1.65139	S0	1.41	1.32	5.3	180	1200
252555	04/04/2011	KPNO/MOSAIC	226.51375	2.18472	Sm	1.41	1.32	5.7	180	1200
252550	04/04/2011	KPNO/MOSAIC	226.47166	2.0075	dI	1.41	1.32	4.5	180	1200
9573	04/04/2011	CTIO/SMARTS	223.26208	3.29556	Sab	1.22	1.20	5.0	180	1800
9574	04/04/2011	CTIO/SMARTS	223.27167	3.33111	SB(s)b	1.22	1.20	5.1	180	1800
243743	04/04/2011	CTIO/SMARTS	220.06375	0.20667	Sc	1.30	1.22	5.0	180	1800
9645	04/04/2011	KPNO/MOSAIC	225.00125	1.89111	SAB(s)b	1.16	1.18	5.4	120	1020
9655	04/04/2011	KPNO/MOSAIC	225.29666	1.70167	E1	1.16	1.18	5.4	120	1020
9661	04/04/2011	KPNO/MOSAIC	225.51459	1.84056	SB(rs)dm	1.16	1.18	5.4	120	1020
241018	04/04/2011	KPNO/MOSAIC	225.06876	2.30056	S0	1.16	1.18	5.4	120	1020
241022	04/04/2011	KPNO/MOSAIC	225.11417	1.62278	SB(s)m	1.16	1.18	5.4	120	1020
254078	04/04/2011	KPNO/MOSAIC	225.41083	1.87028	dE	1.16	1.18	5.4	120	1020
9787	04/19/2009	CTIO/SMARTS	228.92833	1.45528	SABm	1.35	1.56	5.0	180	1800
243026	04/19/2009	CTIO/SMARTS	224.69208	2.96889	E	1.30	1.24	4.8	180	1800
251419	04/30/2009	CTIO/SMARTS	226.03459	1.52444	S0	1.19	1.22	4.5	150	1500
252211	4/17/2012	KPNO/MOSAIC	225.95792	0.97694	dI	1.26	1.24	4.7	180	960
252519	4/17/2012	KPNO/MOSAIC	225.98209	0.42889	Ir	1.26	1.24	4.8	180	960
241031	4/17/2012	KPNO/MOSAIC	225.26291	0.7075	SABm	1.26	1.24	4.9	180	960

Table 3: *Information about the NGC 5846 galaxies that had Hα emission. The date and location of the observation, the RA and Dec, galaxy type, airmass, seeing, and exposure time for each galaxy is presented.*

2.2. Image Reduction

The KPNO MOSAIC images were processed by Dr. Koopmann and myself using the IRAF package *mscred.* The MOSAIC camera has a one degree field-of-view. This is achieved using eight 2038 x 4086 pixel CCD chips, each with two amplifiers, for a total of sixteen images per exposure, stored in a 16-extension fits file. The chips are separated by gaps. In order to produce a gap-free image of a field, five dithered exposures are taken in each filter. The dither pattern can be seen in Figure 7. By observing using this dither pattern, when the images are properly aligned and stacked, the gaps between the

chips will be "filled in" by the other dithers. The reduction process consists of typical CCD processing followed by alignment and stacking of the dithered images. Images were corrected for cross-talk between the chips, bias subtracted, and flattened using a combination of domeflats and skyflats. Bad pixel masks and cosmic ray masks were created for each of the images. Because of the large field-of-view, it is necessary to correct the images for distortion. Each image was registered in the WCS (World Coordinate System) coordinates. The WCS calibration files were downloaded from the KPNO website and the tasks *mscgetcatalog* and *mscmatch* (within the *mscred* pacage) accessed the online U.S. Naval Observatory stellar catalog over the input field and matched these catalog positions to pixel positions of stars. A transformation was determined that converts pixel values to the WCS coordinate system. The chips in each image were then merged to create one image using *mscimage*.

Dither 1	+120	-120
Dither 2	-240	0
Dither 3	0	240
Dither 4	240	0
Dither 5	-120	-120

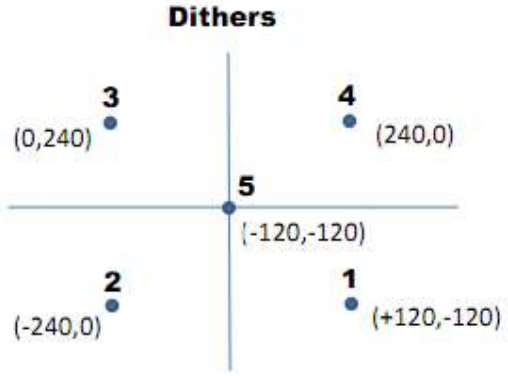

Figure 7: *In order to correct for the gaps between the chips 5 dithers of each field are taken. The center of each dither is indicated in the above figure, with dither 5 being at the center of the field. The table to the left provides the offsets in arcseconds. Image From: ALFALFA Undergraduate Group Webpage.*

Before stacking all the individual images by filter type the images needed to have the same seeing. In IRAF, the *imexam* task was used to measure the full width half-maximum (FWHM) of each image and then *gauss* was used to convolve all the individual

images to the one with the worst seeing. *Gauss* operates by convolving images using an elliptical Gaussian function (where the sigma of the function is chosen by the user). Once this was completed, images of the same filter type were combined (using a median combination operation) with the task *mscstack*. This left two images, one in the broad band R filter and the other in the narrow band Hα filter, both with a seeing of 4.7 arcseconds.

The images were then sky subtracted using a Python program, *measureSky.py*, created by Ryan Muther. Using a coordinate list of points which were blank sky in each image, the program determined the mean sky background value at those points using *fitsky* and then used *imarith* to subtract the mean sky value from the entire image.

2.3. Continuum Subtraction

In order to obtain an image in which just the Hα emission (the star formation regions) could be observed, the images needed to be corrected for the presence of stellar continuum in the Hα filter. Foreground stars are used to determine this correction because they do not (usually) emit Hα and therefore their emission in the Hα filter is due solely to the stellar continuum. This is accomplished by determining the fluxes for 25 stars in each image and finding the ratio of the fluxes in the Hα and R images. This ratio is then used in a scaled subtraction. The broad band R filter image is multiplied by this ratio and then subtracted from the Hα image. This leaves an image where only the Hα+[NII] wavelengths (referred to in the rest of the thesis as Hα) are visible, removing stellar light.

This continuum subtraction was accomplished using Ryan Muther's Python program *contSub.py*, which read in the R and Hα images, aligned them with *imalign* by

finding the centers of bright stars using the *daofind* package, found the fluxes of these stars in both images, determined the average scale factor of the R and Hα images, and then applied this scale factor using *imarith*. When a continuum subtraction has been performed, it is clear if the image was over subtracted or under-subtracted by examining the Hα continuum subtracted image. If the images were over subtracted, then dark negative residuals will be apparent and if the image was under-subtracted then foreground stellar (non-Hα) sources will still be visible. So, the scale factor found using the *contSub.py* program was used as an approximation and a starting point for the final continuum subtraction. By starting with the program's estimate of the scale factor, through inspection of the Hα image, and by trial and error with tweaking the subtraction factor, the best possible Hα continuum subtracted images were produced.

It is important to acknowledge that the continuum subtraction factor is a source of significant error. As Waller (1990) describes, there are several sources of error to account for in the continuum subtraction process. Uncertainties arise from atmospheric extinction (±5% for R), sky-brightness subtraction (±5%), NII contamination (±5%), which occurs since the NII line is very close to the Hα emission line, standard-star calibration conversion (±5%), and the fact that different parts of the chip have different continuum values (±30%) (Waller 1990; Bushouse 1985). The variation in the continuum presents the largest error in regions where the Hα is low, since most of the light detected in the Hα filter is due to the continuum. Therefore, even a slight error in the scale factor will produce a large error in the Hα. It is also useful to note that on bright or over-saturated foreground stars, it is common for the Hα continuum subtracted image to have residuals. Similarly, bright galaxy centers can also often leave residuals, a result

of a mismatch in the PSF of different filters (and also due to the fact that the colors of the galaxy's nucleus and outer regions can be different).

I next rotated the images to give them the proper orientation (North at the top and East to the left of the image). Each image needed to be rotated 90 degrees and inverted across the x-axis. This was done on the Hα continuum subtracted images and the broadband R filter images using the tasks *imtranspose* and *imcopy*.

In order to make the file size of the image more manageable, the images were split up into sections (using *imcopy*) with each section containing one or two galaxies. The galaxies in the field were located using TOPCAT (Tool for Operations on Catalogues and Tables) and confirmed using the IDL program *agcbrowse*. Then cutouts of the image, using *imcopy*, were made for each galaxy. To ensure that there were no other galaxies or objects in the field that TOPCAT had failed to locate, I scanned the whole Hα continuum subtracted image, searching for emission. For each of these sections I also made sure that the sky background had been properly subtracted (using *imexam* and *implot)* and made small corrections (using *imarith*) when the sky background had been over or under subtracted. Due to the size of the MOSAIC images, removing the sky background was not a trivial task. The sky values varied over the field, with a range of about 6 counts in the R image and 9 in the Hα.

2.4. Masking

Masks were created so that stellar residuals and foreground stars would not interfere with photometry. Using IRAF and the ds9 display, for each galaxy I found the galaxy center (both by eye and using *center*) and then fit an ellipse around the galaxy's R filter image. Using the ellipse tool in ds9 I determined the semi-major and semi-minor

axes of each galaxy as well as the galaxy's position angle and eccentricity. I also determined the farthest extent of each galaxy in both the R and Hα images. Using this information as input, two Python programs *maskstars.py* and *handmask.py* (written by Ryan Muther) were used to create masks for the images. The program *maskstars.py* reads in the R and Hα images along with a file that contained the coordinates of the center of the galaxy, the galaxy's semi-major axis, eccentricity, and position angle to automatically mask stars that are outside the galaxy's radius (as defined by the ellipse information from the input). The programs uses *daophot* in IRAF to find stars and creates a circular masked region that is 5 times the size of the FWHM around each star.

The *handmask.py* program was used to improve the results of the initial mask. For example, masking stars that were very close to the galaxy in the image and those that were saturated and need a larger aperture mask. This program used *imedit* to allow the user to place additional circular masks on the image through the use of the ds9 display. The user has the ability to control the size and location of each added masking region. The final mask is saved as a separate image with pixels set to either 1 for a masked pixel or 0 for a good pixel, and is read into the photometry program with the original image.

2.5. Photometry

Before performing photometry to analyze the flux of each galaxy, the calibration factor to absolute flux units needed to be found. The calibration factor corrects for atmospheric extinction and instrumental effects. The calibration is based on observations of two to three spectrophotometric standard stars (during photometric nights). Spectrophotometric standard stars have been observed in filters at 5-nm intervals (for example by Massey et al. 1988 and also work done by Hamuy et al. 1992). To determine

the expected flux, the "spectrum" of the standard is convolved with the transmission curve of the filter. This result is compared with the aperture photometry from the spectrophotometric standard stars, corrected for airmass. For field 4 the calibration factors were 964 x 10^{-18} erg cm^{-2} s^{-1} / counts s^{-1} for the R filter and 1028 x 10^{-18} erg cm^{-2} s^{-1} / counts s^{-1} for Hα. To find the factor for each galaxy in the field, these values were divided by the exposure time of the image and were divided by the value $10^{-(0.1*Airmass)/2.5}$, where airmass and exposure time were obtained from the image headers. The resulting factors can be multiplied by fluxes in units of counts to convert to units of erg cm^{-2} s^{-1}. These factors were used in the input file for the photometry. The photometry on the galaxies was performed in two methods. The IRAF task *polyphot* was used to find the total fluxes of the galaxies (yet since this program does not provide radial analysis, just total flux, the results of *polyphot* served more as a verification check and are not presented in this paper) while IDL programs (written by Dr. Koopmann) were used to determine the surface brightness of each galaxy as a function of distance from the galaxy's center. Surface brightness, a quantity independent of an observer's distance away from a source, is the value of flux divided by area.

The task *polyphot* in IRAF was used to calculate the total flux of each galaxy, both in the broad band R image and the Hα continuum subtracted image as well. This task works by allowing the user to define a polygonal region around the galaxy and IRAF outputs the total flux within the outlined region. The polygonal region for each galaxy was determined using the elliptical regions previously created for the masking process, which defined the outer extents of the galaxies.

In addition to the total flux, it was also of interest to examine the galaxy's star

formation regions (Hα regions) in terms of radial dependence. This could give insight into the possibility of environmental interactions, since interactions, such as ram pressure stripping, can remove gas from the outer regions of the galaxy and truncate star formation. Radial profiles were created using the IDL programs *sphotr* and *sphotha*, written by Dr. Koopmann. These programs worked by measuring fluxes in elliptical annuli around the galaxy. Ellipse center, position angle, and inclination were defined by examination of contour plots of R light in ds9 and center in IRAF. The same set of ellipses was used for the R and Hα images. The program reads in the x and y coordinates of the galaxy's center, the position angle and the inclination of an ellipse, the image's FWHM (found using the *imexam* task), the sky background uncertainty (found using *implot, fitsky,* and *imexam*), distance, pixel scales, and image calibration factor. The program creates a small ellipse of semimajor axis equal to the seeing and centered on the galaxy and determines the flux within that first ellipse. Then the program creates another ellipse with a larger radius and again finds the flux inside the new annulus. The radius of the ellipses increased by the seeing value plus a small increment of 10% of the seeing (this increase in the number of pixels reduces the increased random error in the pixels detecting less light, since the noise is Poissonian and equals the square root of the signal). The program iterates until the value of the flux from the galaxy in the annulus is less than the estimated noise. The estimated noise is the standard deviation of the mean sky value added in quadrature to the user-determined systematic error in the sky background. The estimated error in the sky background is an input to the IDL program. The program calculated the surface brightness in each annulus by summing the flux and dividing by the surface area. The program also measure isophotal radii (such as r_{24}). An isophotal

radius is the distance at which the average surface brightness at that distance is some specific value (Loveday 2007). So, r_{24} is the distance from the center of the galaxy at which the average surface brightness is 24 mag arcsec^{-2}. The isophotal magnitude is the magnitude of light measured within that radius (Loveday 2007). In Hα, the photometry program calculated the r_{17} value, the isophotal radius in Hα where the surface brightness reaches 17 x 10^{-18} erg cm^{-2} s^{-1}. The radius containing 95% of the flux in Hα is also calculated. The C_{30} concentration value in the R filter is calculated as an indicator of the morphological type. C_{30} is found by taking the R flux at 0.3 times the r_{24} radius and then dividing by the R flux at r_{24}, and can be written as $C_{30} = \frac{F_R(0.3r_{24})}{F_R(r_{24})}$ (Koopmann, Kenney, & Young 2001). The concentration for Hα was also calculated by taking the Hα flux at a radius of 0.3xr_{24} and dividing by the total Hα flux.

The final piece of photometry was to correct for each galaxy's inclination on the sky. This was accomplished through the use of two IDL programs, *interphot* and *interphotha* (both written by Dr. Koopmann). If a galaxy is inclined, then the observer is looking through more of it compared to if the galaxy was face on. Therefore, for an inclined galaxy the observer will see an increase in brightness. To correct for this, we assume the disk is transparent and correct to make it face-on by dividing by the value: $\cos(\frac{minor\ axis}{major\ axis})$. The corrective process does however neglect the galaxy's internal extinction and to adjust for this estimates are made during the star formation calculations. The inclination correction programs used the existing photometry results from the *sphotr* and *sphotha* programs and corrected them based on the galaxy's angle of inclination of the sky.

The star formation rates (SFR) were also calculated using an IDL program, *sfr_calc_inc*, written by Dr. Koopmann. This program corrected for internal extinction, NII contamination, filter transmission, and then used the conversion factor:

SFR (Solar Mass / year) = 7.9×10^{-42} L(Hα) ergs/sec (Kennicutt 1998).

3. Results and Discussion

3.1. Methods of Galaxy Comparisons

Due to their vast differences in size, morphology, and stellar composition, comparing galaxies with one another can be a difficult task. For example, if you had a large galaxy (call it galaxy A) and a small galaxy (galaxy B) then comparing the raw HI mass would not be useful since unless galaxy A is very HI deficient, it will likely have more HI mass. A more useful comparison would be the HI mass divided by the galaxy's total mass. This concept of scaling and normalizing different parameters before comparing different galaxies is critical for meaningful analysis. Common factors to scale by include size (such as isophotal radius), mass (gas mass, stellar mass, etc.), and luminosity (assuming that luminosity traces or scales with mass). In the past, luminosity was a common scale factor practice in many studies because it was more easily available than stellar mass. Scaling by stellar mass, while it can be subject to systematic errors, is now possible due to advances in modeling and the use of multi-filter imaging. Another useful parameter for comparing galaxies is HI deficiency. HI deficiency is defined as log(HI Mass Expected / HI Mass Observed) (Haynes & Giovanelli 1986). The amount of HI mass "expected" is an estimation based on the galaxy's morphology and size. HI deficiency is a negative number for galaxies with higher than expected HI mass and positive for galaxies with lower than expected HI masses. Galaxies in clusters tend to be HI deficient.

An extremely useful tool in the comparison of galaxies is the use of large surveys, such as ALFALFA and the Sloan Digital Sky Survey (SDSS). The SDSS is a drift survey in 5 wavelength bands of much of the sky visible from its 2.5-meter telescope located at Apache Point Observatory in New Mexico. It has gathered and publically archived observations of over 930,000 galaxies, with followup spectroscopy for a large subset. The NASA-Sloan Atlas (NSA) provides a downloadable archive of photometry and spectroscopy results. This survey provides, for example, photometry, stellar masses, and emission-line information for galaxies. The NGC 5846 group lies within its survey area.

In this study, we also used the Arecibo General Catalog (AGC), a private catalog of galaxies that contains HI detections and is maintained at Cornell University by Dr. Martha Haynes. The AGC was originally based on the Uppsala General Catalog (UGC). It uses UGC numbers where available and galaxies are added using a 6-digit numerical code.

3.2. Overview and Detection Rate

The four KPNO MOSAIC fields together survey a large portion of the core of the NGC 5846 group. Combining the NGC 5846 group data in the KPNO images (produced by O'Brien, Darling, Warrener, Dr. Koopmann, and myself) there were a total of 79 galaxies. Of these galaxies 25 had Hα emission, corresponding to a detection rate of 32 percent. Many of the undetected galaxies are early-types that typically do not have star formation (or Hα emission) or HI gas. According to Mahdavi et al. (2005), NGC 5846 is composed of 80±5% early-type dwarf galaxies. Since this study of NGC 5846 is concerned with star formation, this thesis only examines the galaxies with detected Hα

emission.

3.3. Radial Profiles and Initial Analysis

The photometry results were used to construct radial profiles, in which surface brightness in mag arcsec^{-2} is plotted as a function of distance from the center of the galaxy. Figure 8 shows these surface brightness profiles, with the solid line representing the R image and the dashed line the Hα image. In the upper right the galaxy's morphological type is given. The Hα profile is plotted on the same graph as the R profile, but with an offset so that it lies near the R profile (the same offset is used for all graphs). The isophotal radius in R, r_{24}, (with error) is indicated by an arrow, and the isophotal radius in Hα, r_{17}, is indicated by a solid black dot. In the radial profiles, the diamonds indicate azimuthally averaged Hα below noise value (so where the signal was less than the uncertainty in the annulus), as was done in the Koopmann, Kenney, & Young (2001) study. In addition, all the radial profiles are graphed on the same scale in order to indicate the relative sizes of the galaxies. Also included in Figure 8 are the broadband R image and the Hα continuum subtracted image for each galaxy. In each set of images the broadband R filter is on the left and the Hα continuum subtracted image is on the right.

Figure 8: Galaxy R and Hα images with accompanying radial profiles

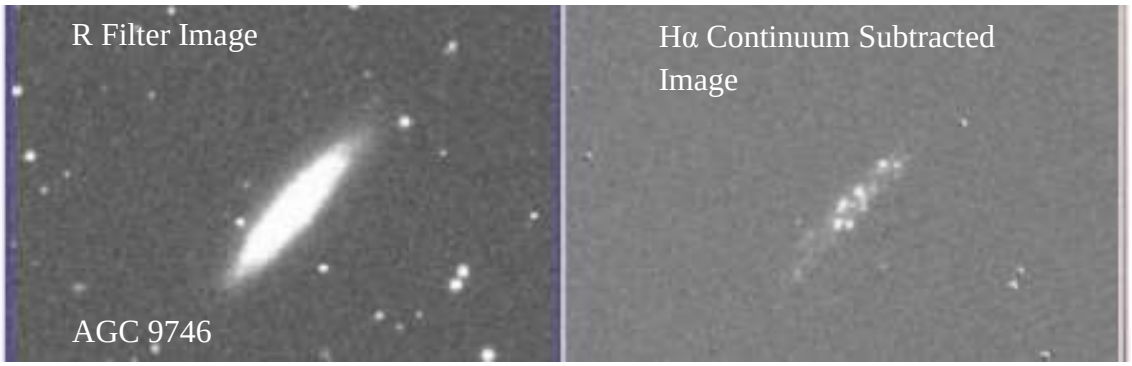

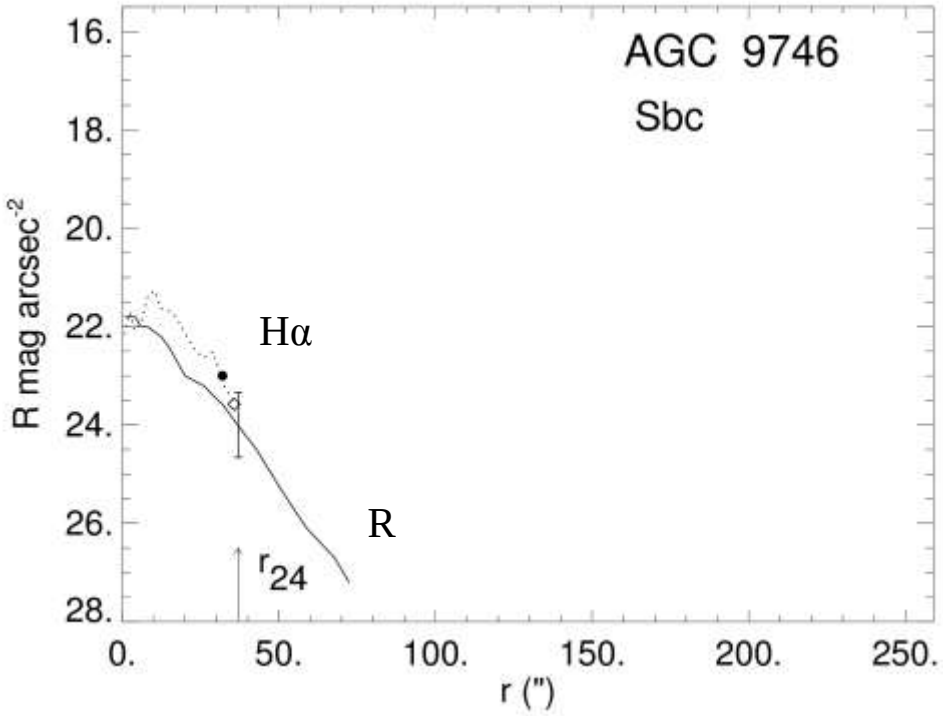


AGC 9751

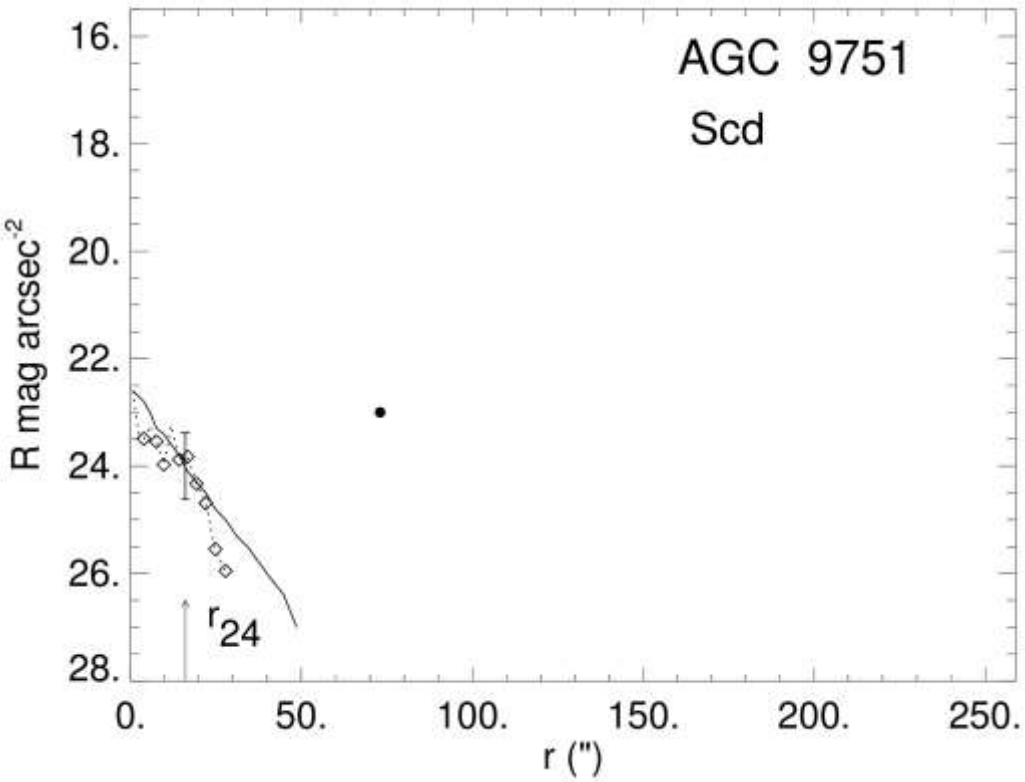
AGC 9751
Scd
R mag arcsec^{-2}
16.
18.
20.
22.
24.
26.
28.
r_{24}
0.
50.
100.
150.
200.
250.
r (")

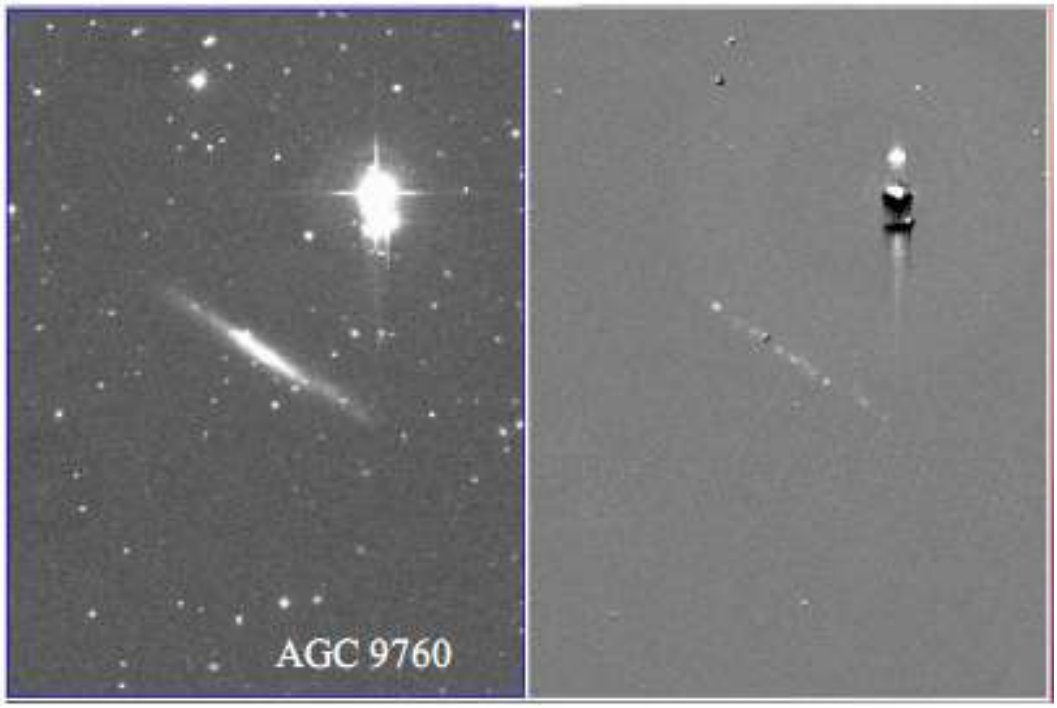

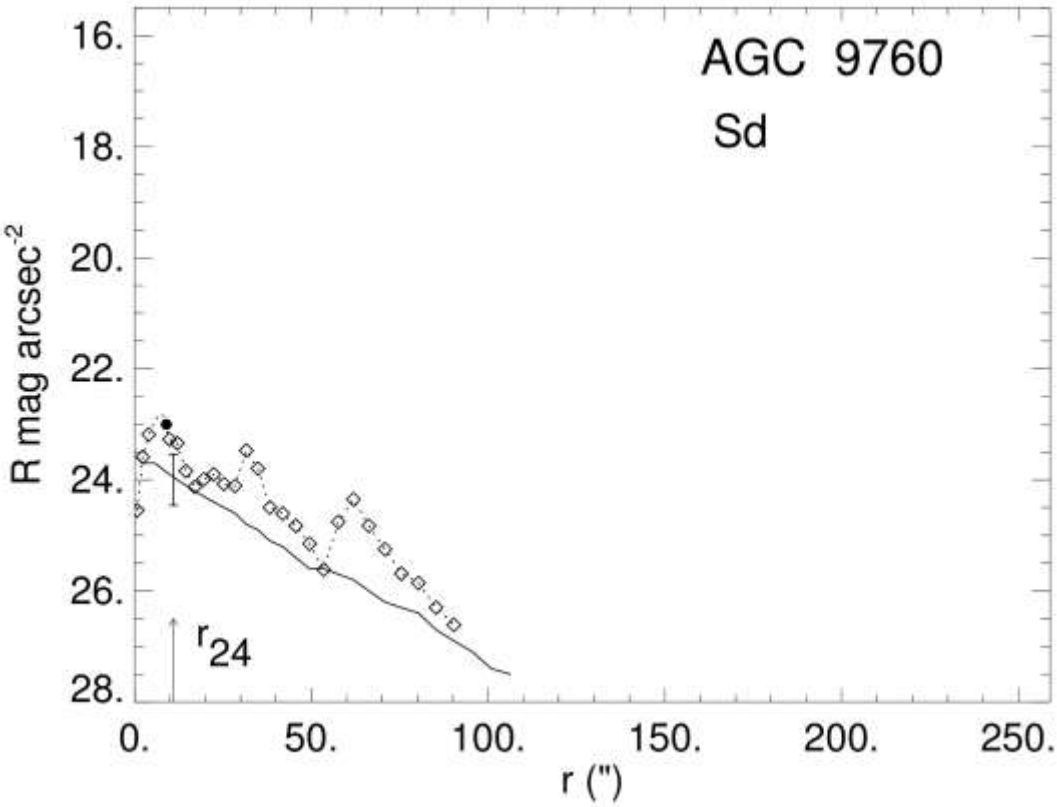

Note: The Hα radial profile for AGC 9760 looks atypical in that the surface brightness appears unusually noisy. This could possibly be due to the edge-on nature of AGC 9760. This galaxy should be reexamined.

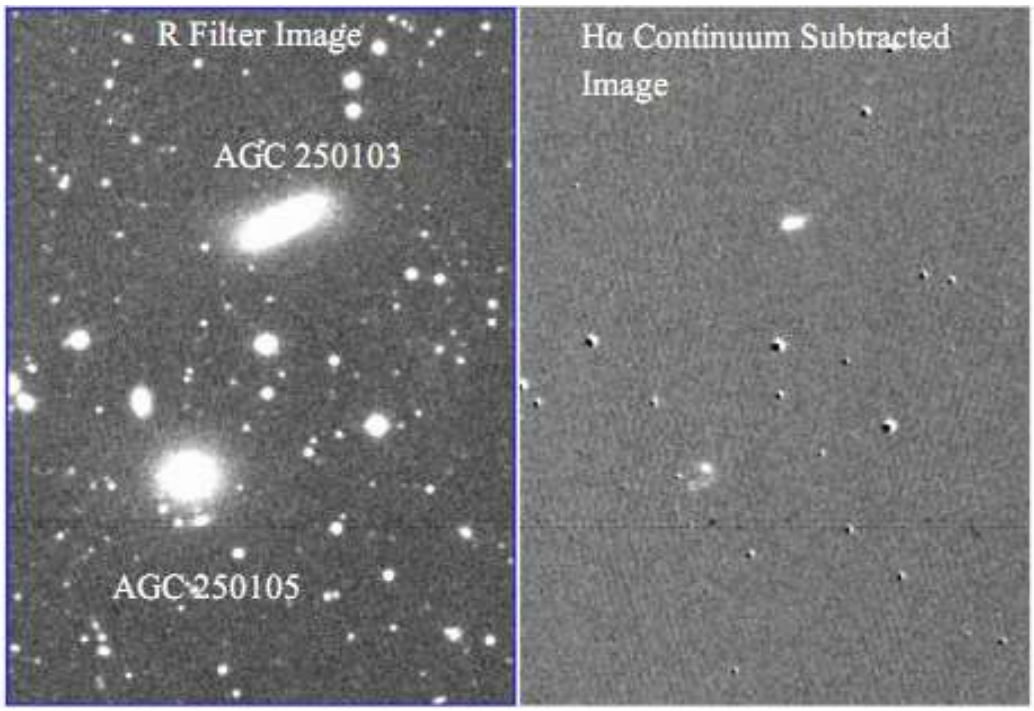
R Filter Image
AGC 250103
AGC 250105
Hα Continuum Subtracted Image

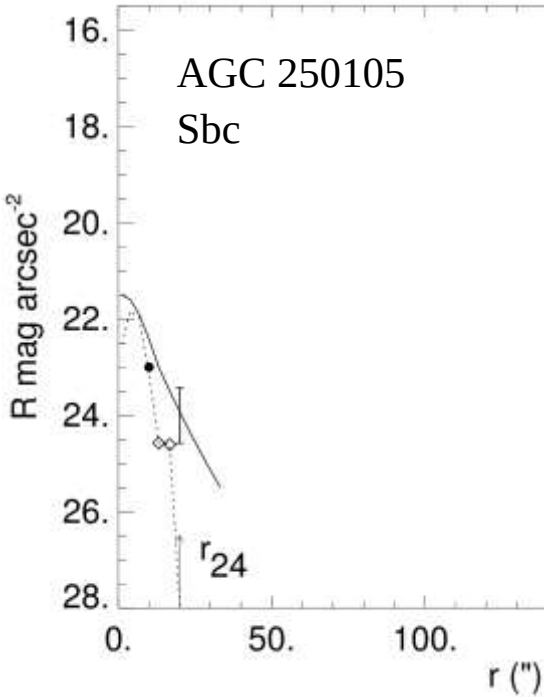
AGC 250105
Sbc
R mag arcsec^{-2}
16.
18.
20.
22.
24.
26.
28.
0.
50.
100.
r (")
r_{24}

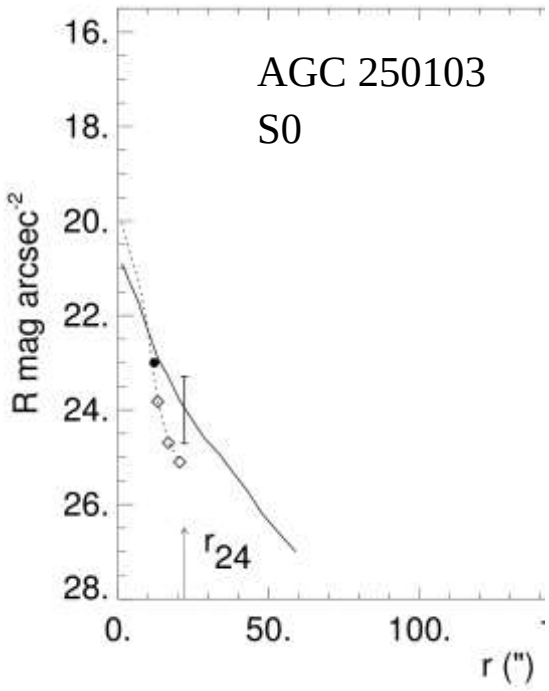
AGC 250103
S0
R mag arcsec^{-2}
16.
18.
20.
22.
24.
26.
28.
0.
50.
100.
r (")
r_{24}

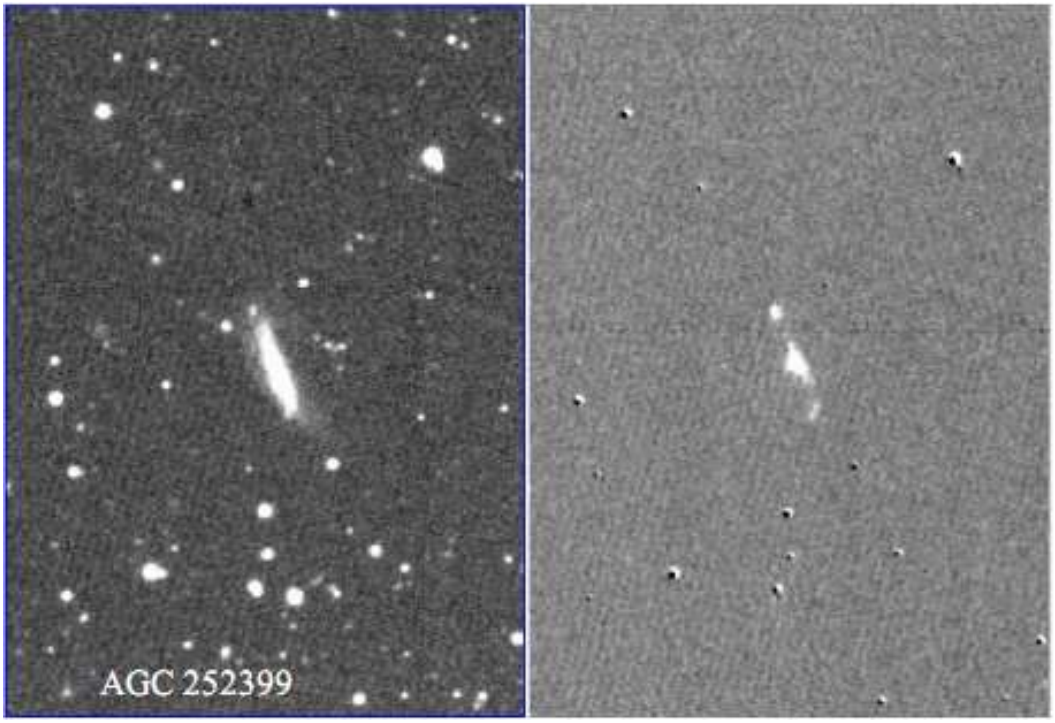
AGC 252399

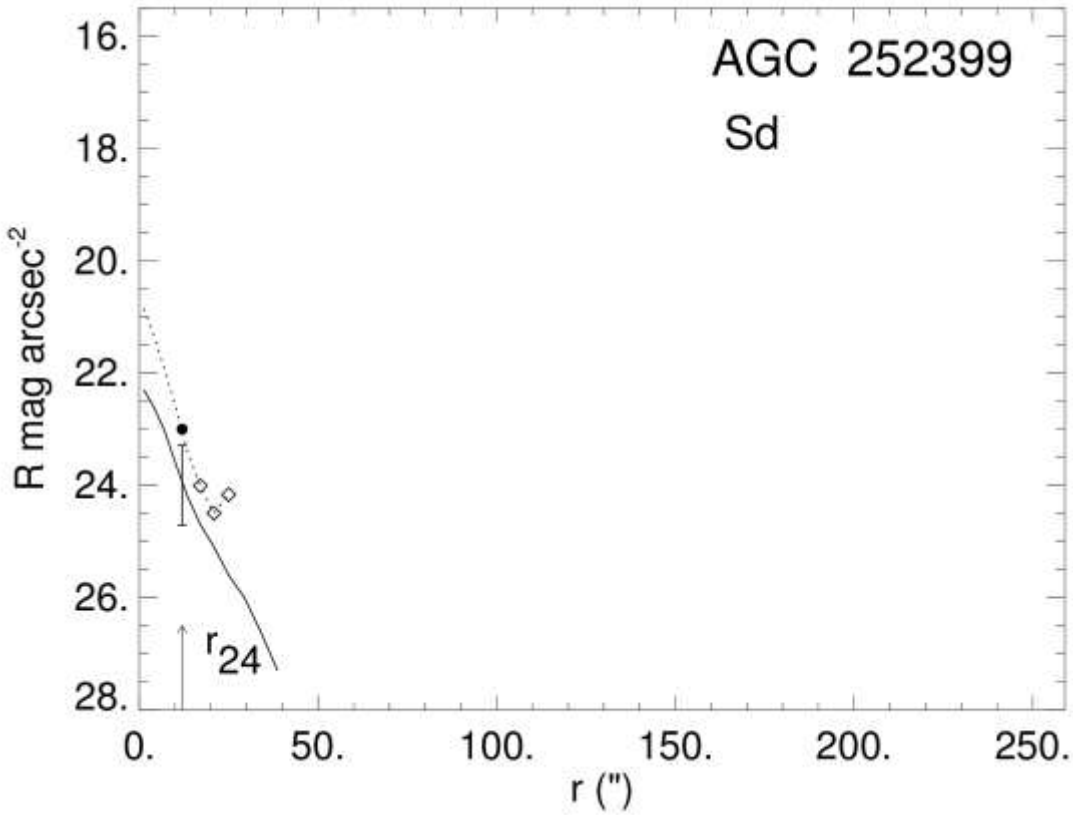
AGC 252399
Sd
R mag arcsec^{-2}
16.
18.
20.
22.
24.
26.
28.
0.
50.
100.
150.
200.
250.
r (")
r_{24}

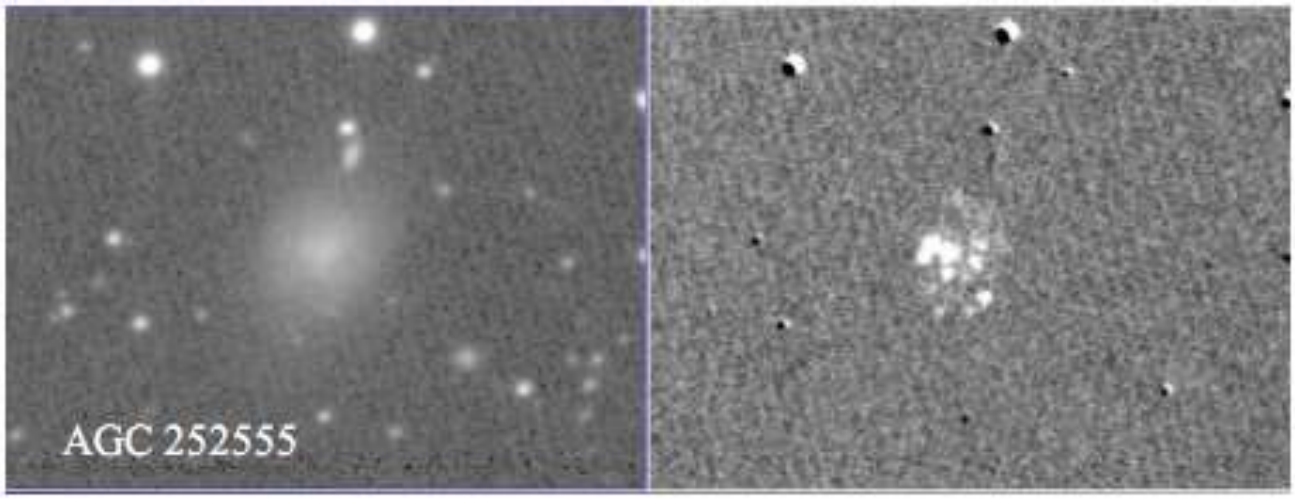
AGC 252555

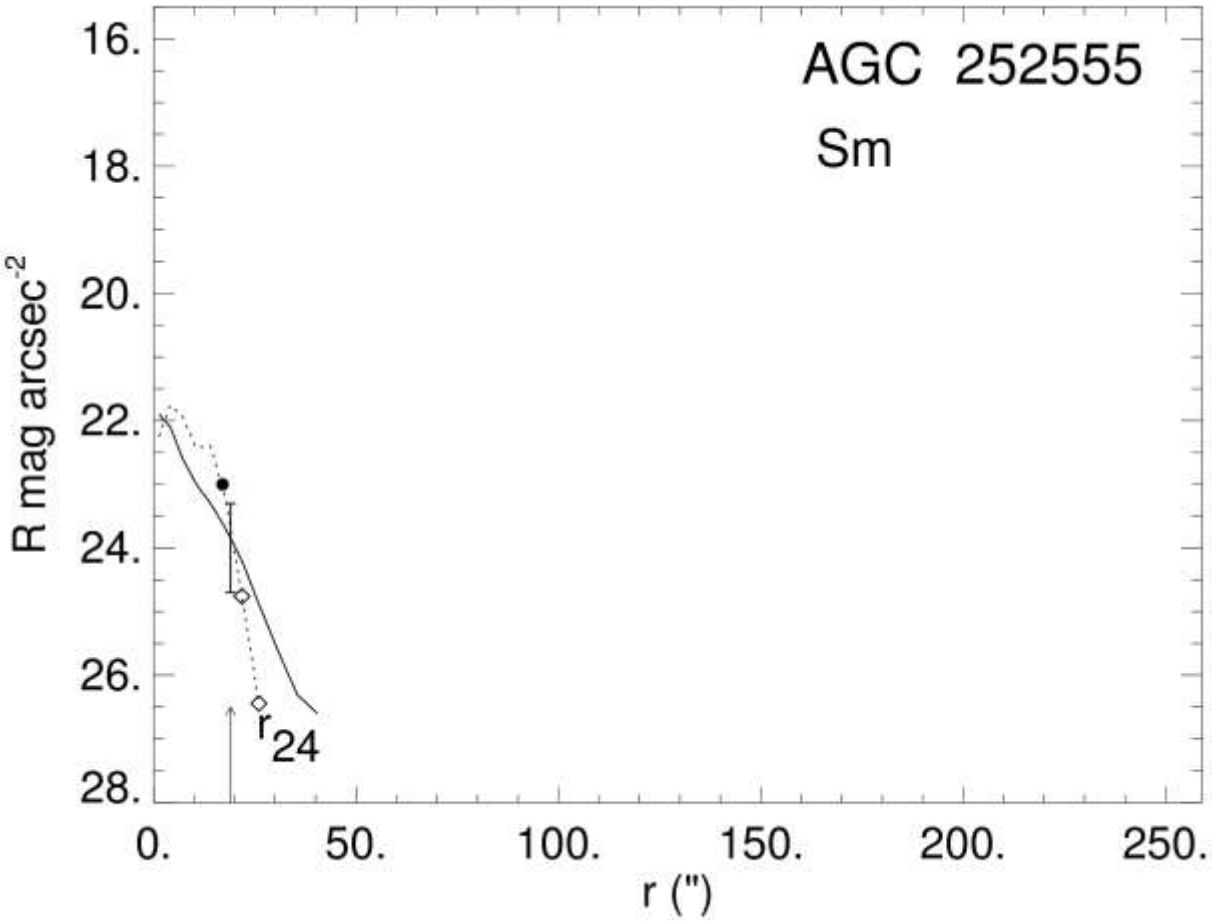
AGC 252555
Sm
R mag arcsec^{-2}
16.
18.
20.
22.
24.
26.
28.
0.
50.
100.
150.
200.
250.
r (")
r_{24}

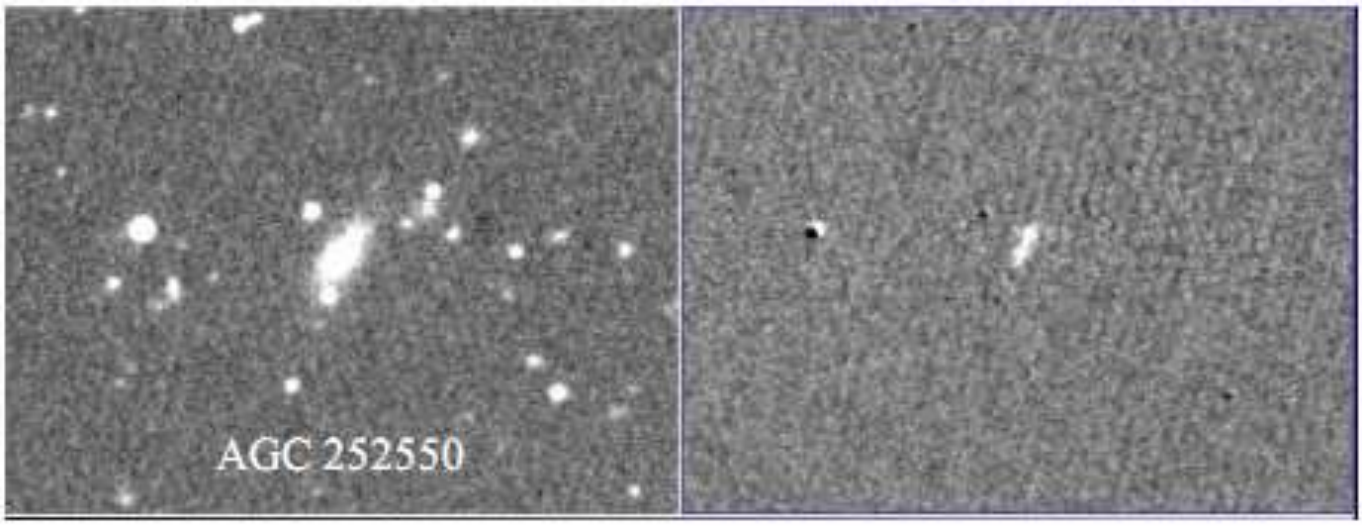
AGC 252550

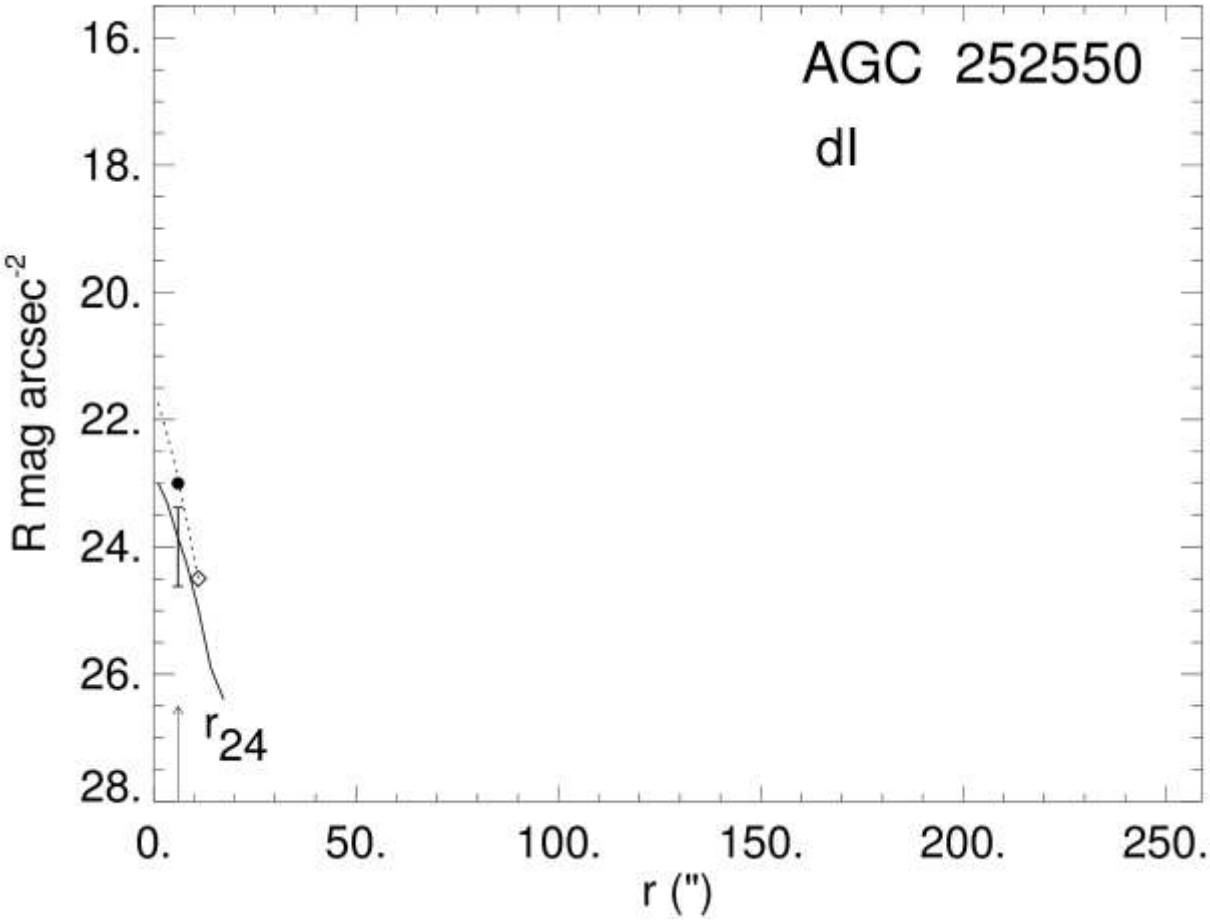
AGC 252550
dI
R mag arcsec^{-2}
16.
18.
20.
22.
24.
26.
28.
0.
50.
100.
150.
200.
250.
r (")
r_{24}

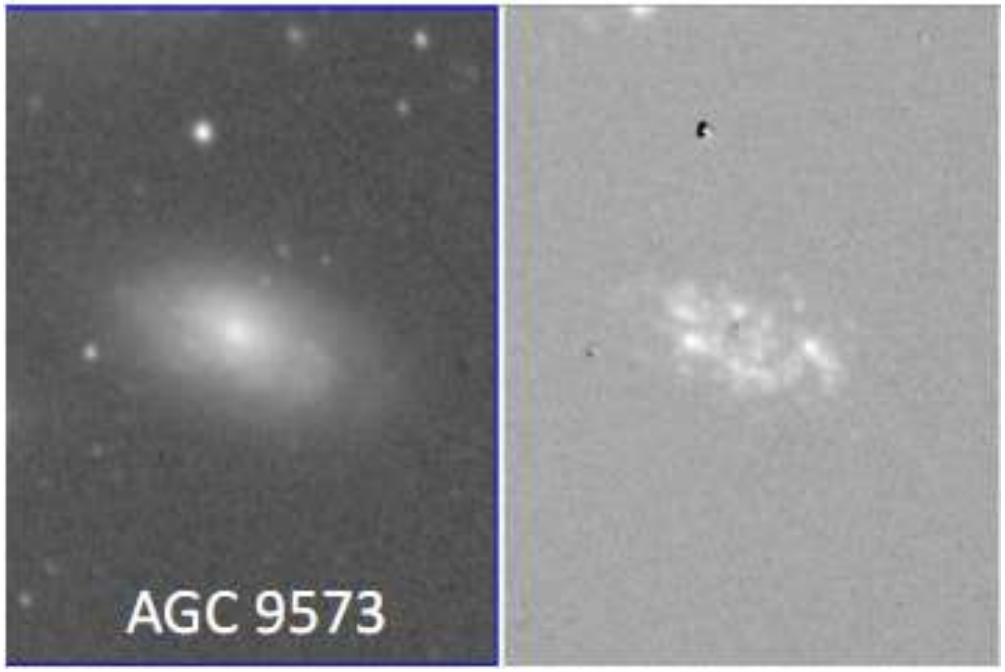
AGC 9573

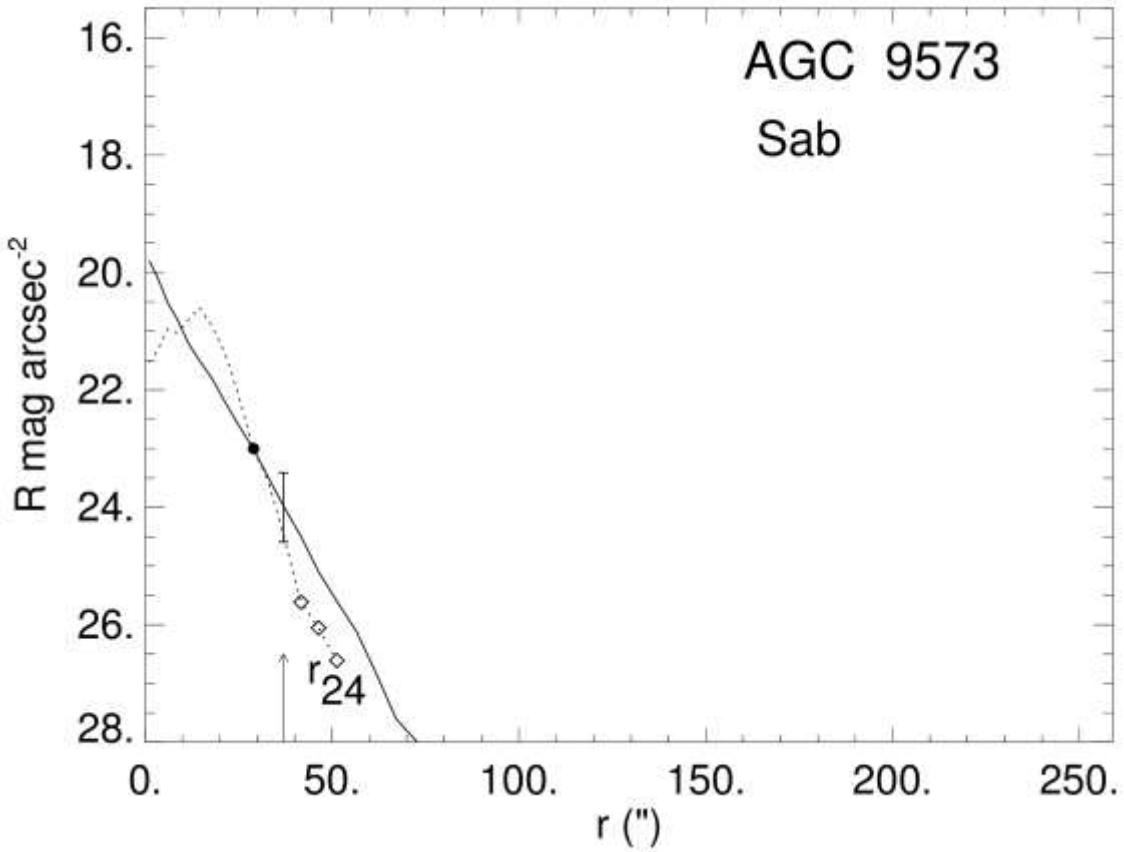
AGC 9573
Sab
R mag arcsec^{-2}
16.
18.
20.
22.
24.
26.
28.
0.
50.
100.
150.
200.
250.
r (")
r_{24}

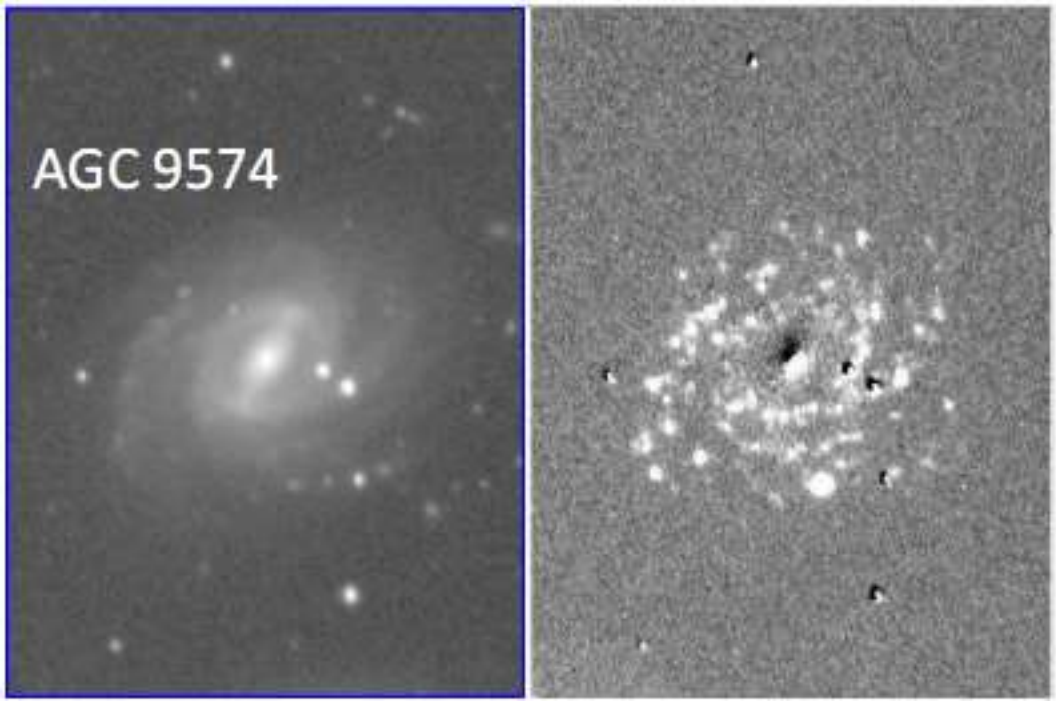
AGC 9574

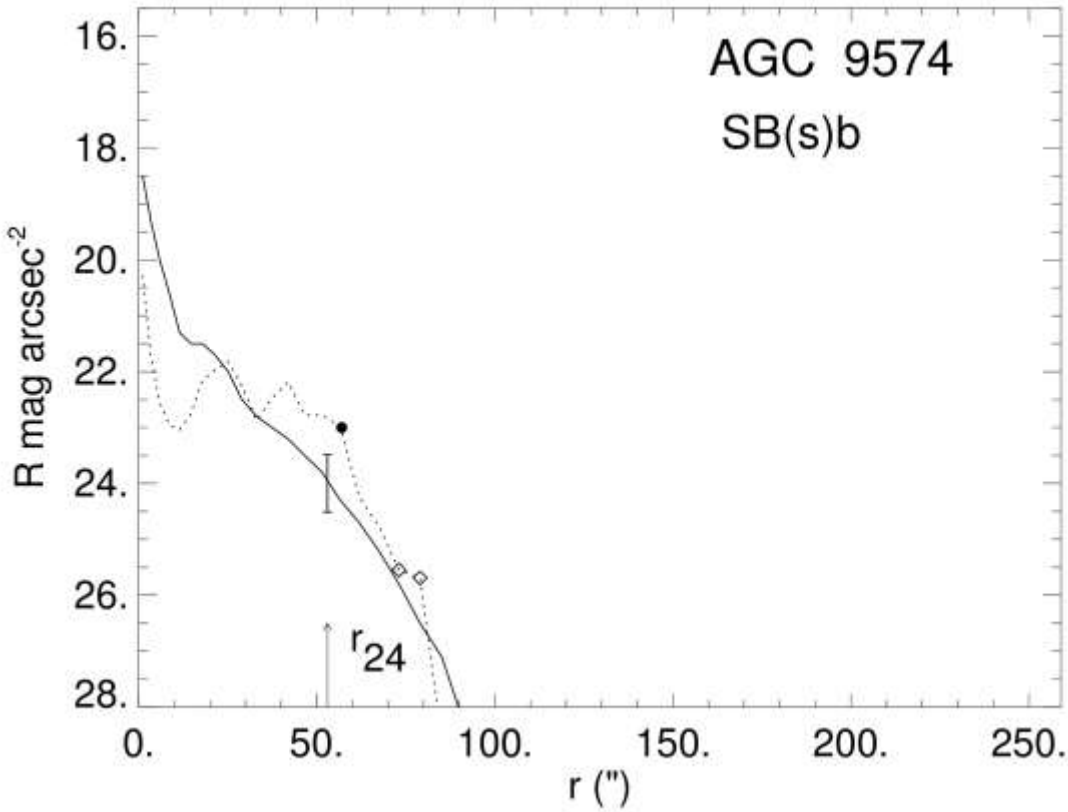
AGC 9574
SB(s)b
R mag arcsec^{-2}
16.
18.
20.
22.
24.
26.
28.
0.
50.
100.
150.
200.
250.
r (")
r_{24}

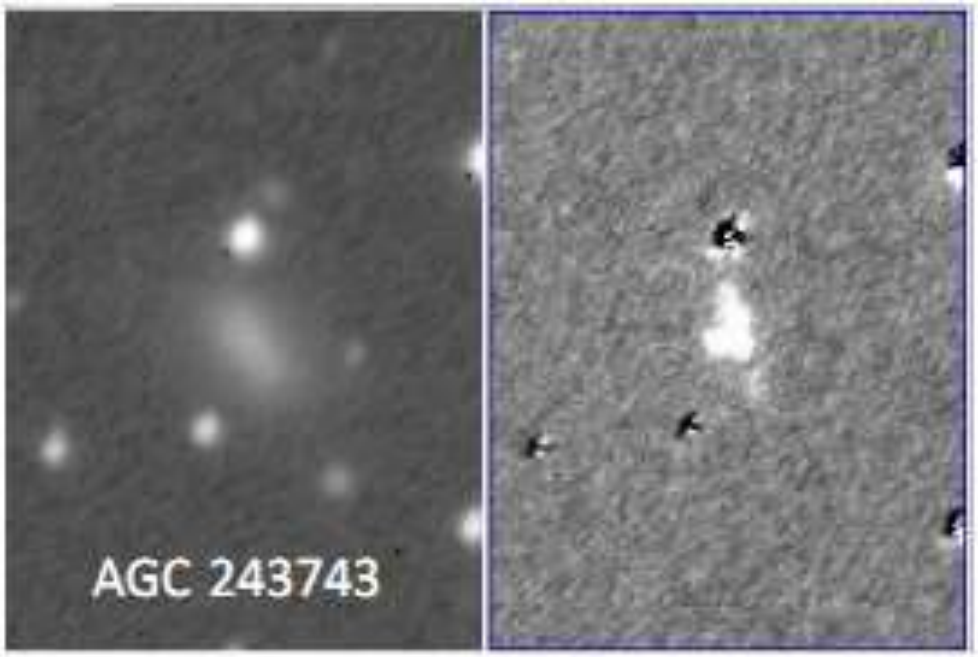
AGC 243743

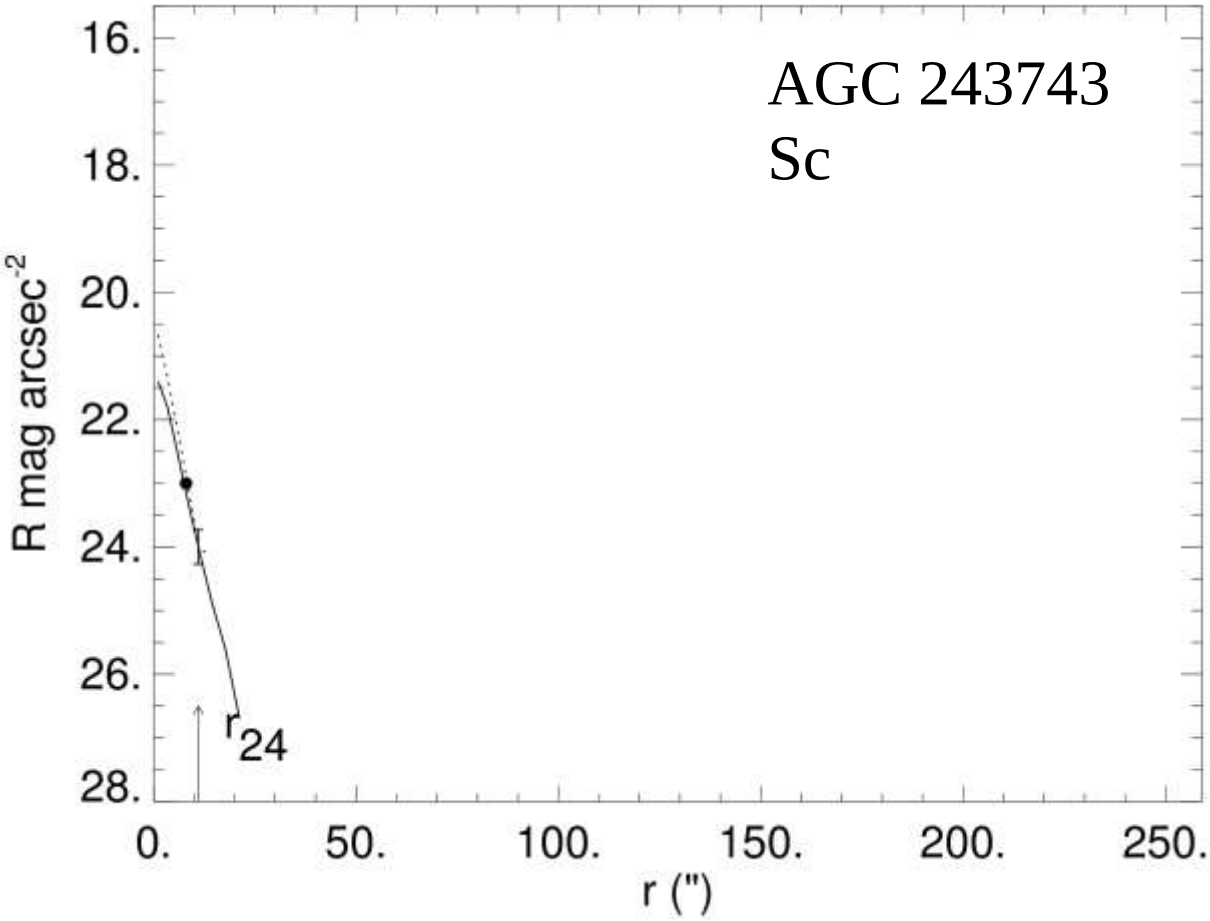
AGC 243743
Sc
R mag arcsec^{-2}
16.
18.
20.
22.
24.
26.
28.
0.
50.
100.
150.
200.
250.
r (")
r_{24}

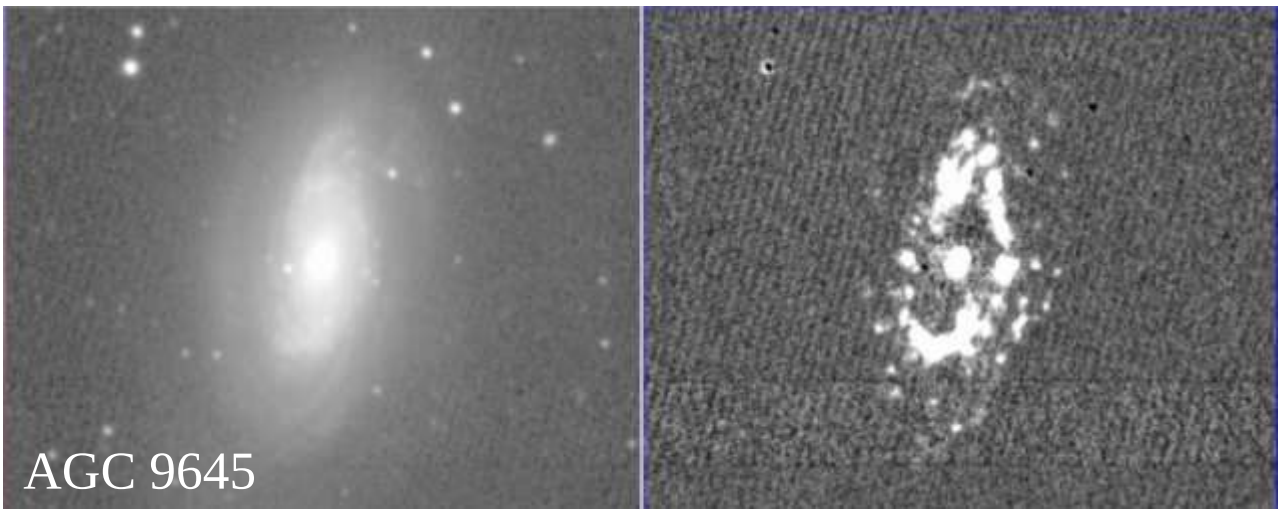

Image Reduced by Warrener, M. Union College Summer Research Paper

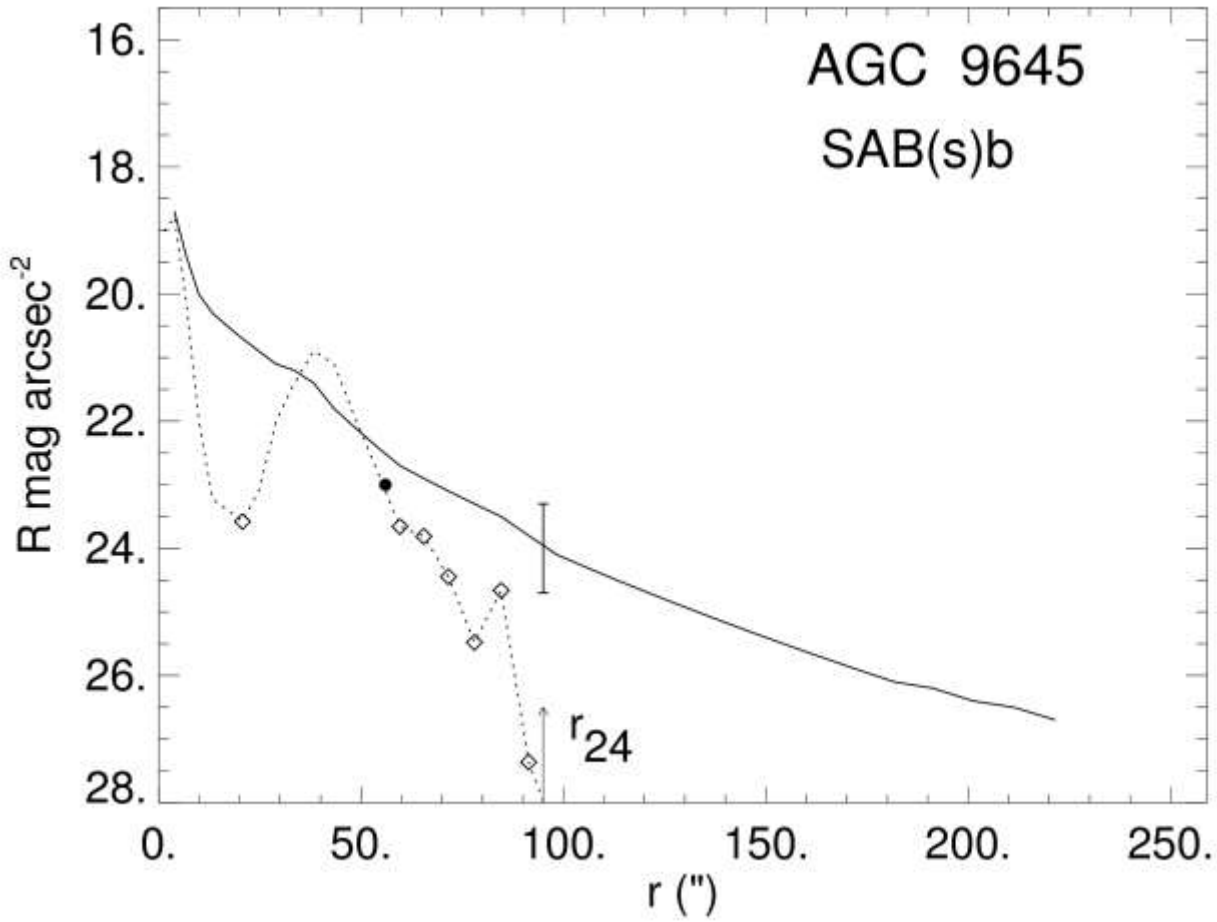

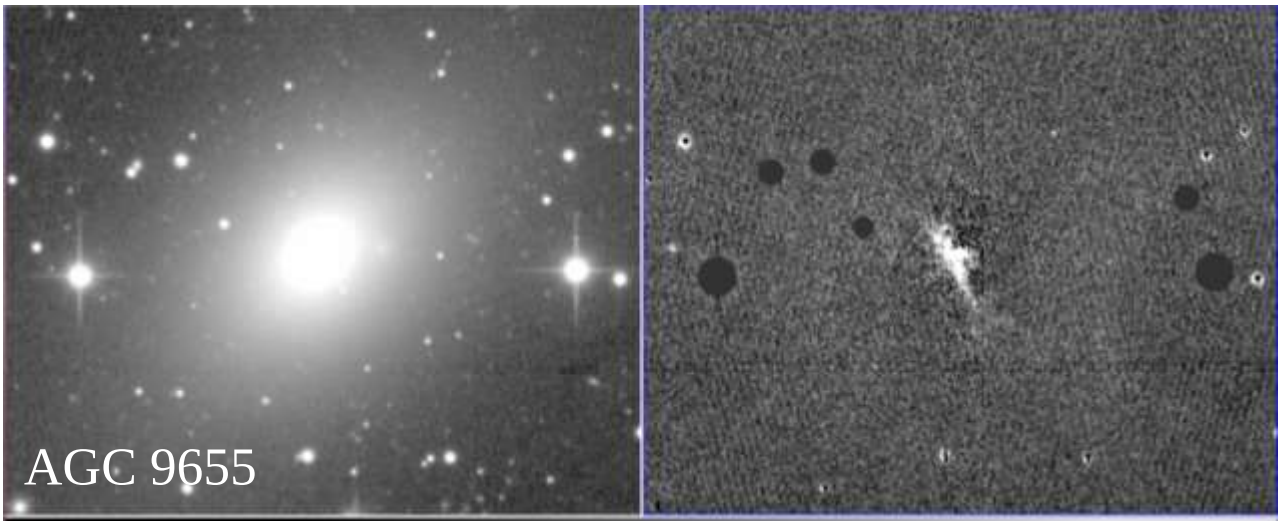

Image Reduced by Warrener, M. Union College Summer Research Paper
Note that AGC 9655 appears to have some sort of outflow, possibly AGN activity.

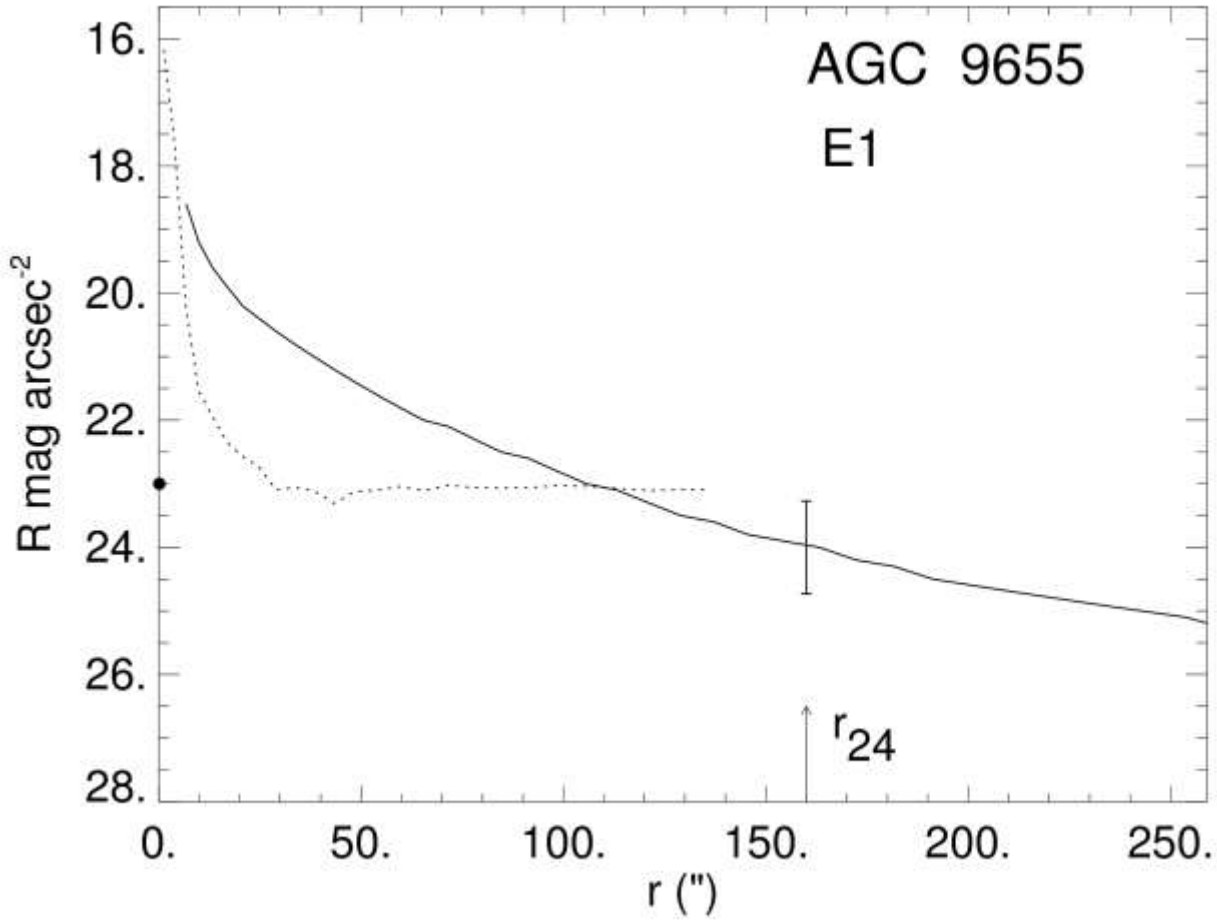

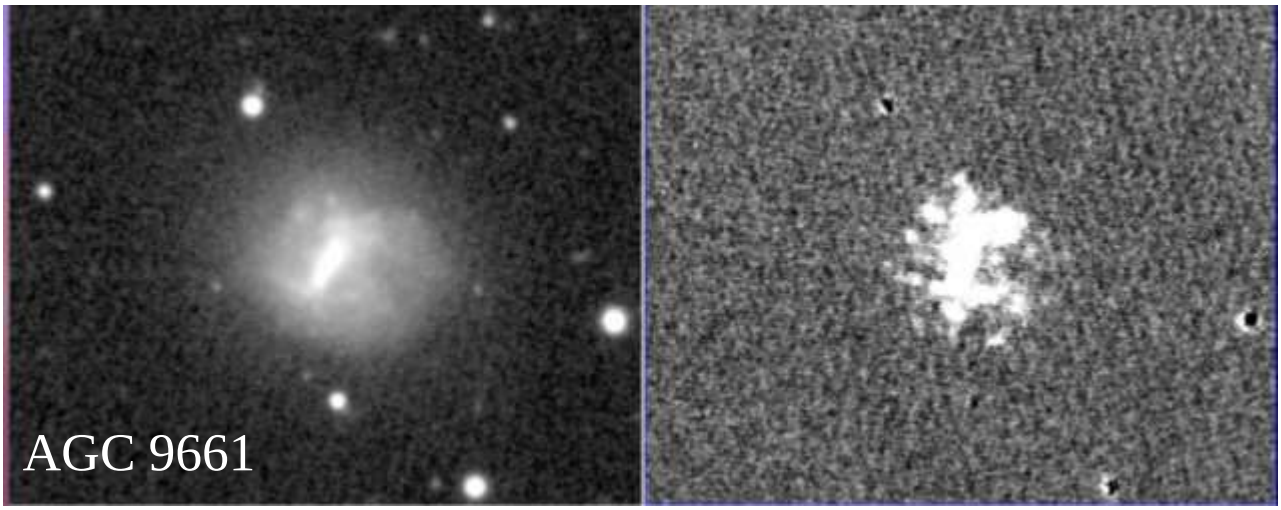

Image Reduced by Warrener, M. Union College Summer Research Paper

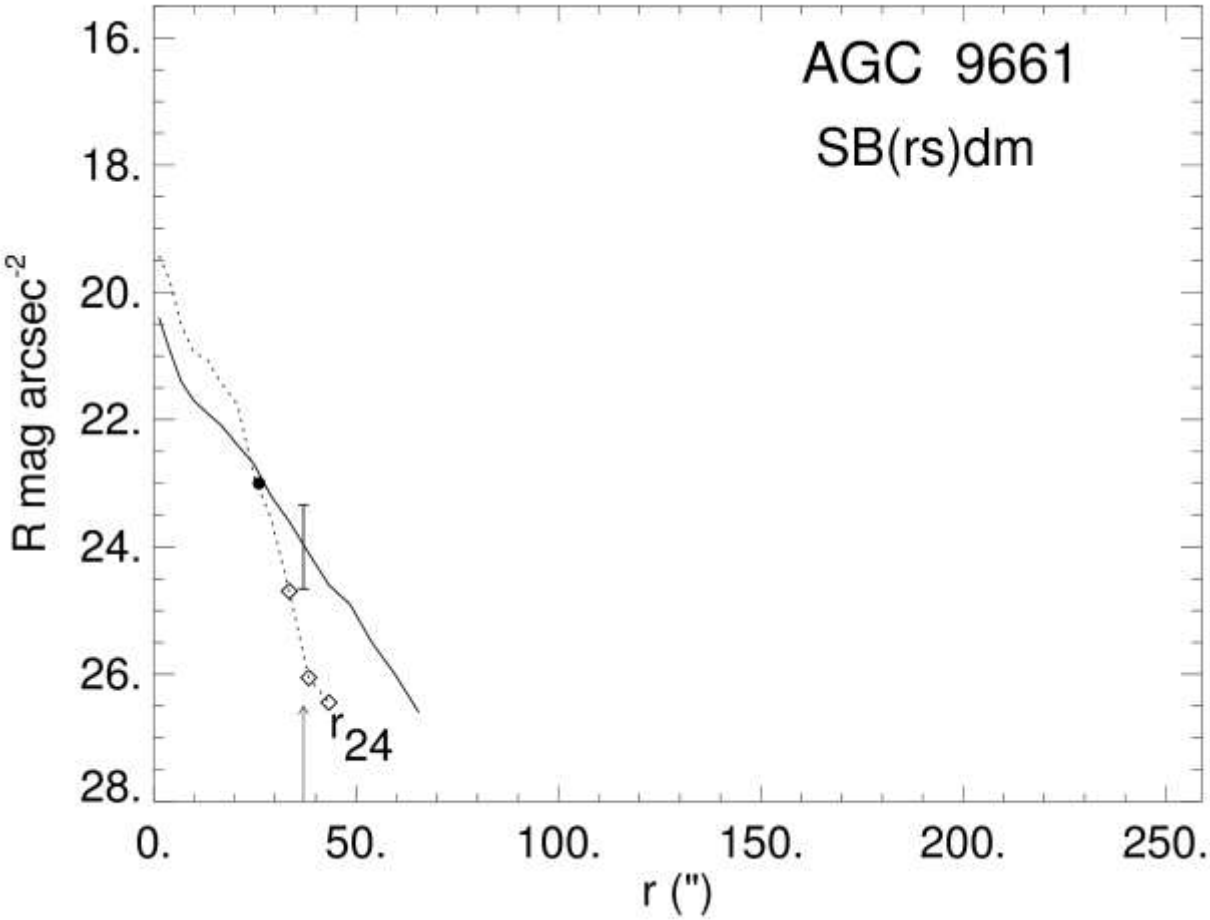

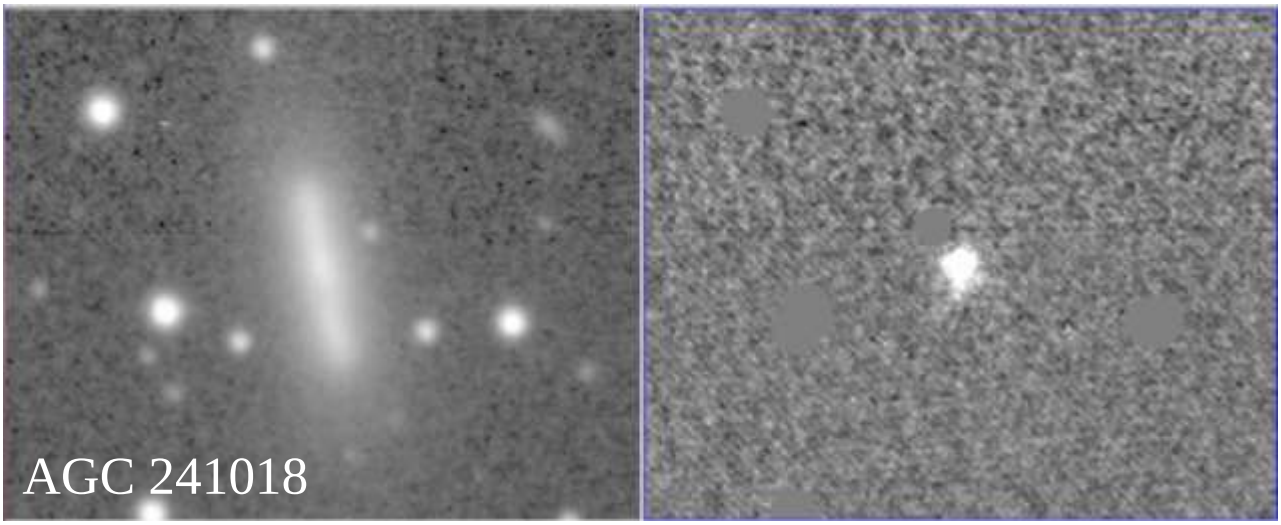

Image Reduced by Warrener, M. Union College Summer Research Paper

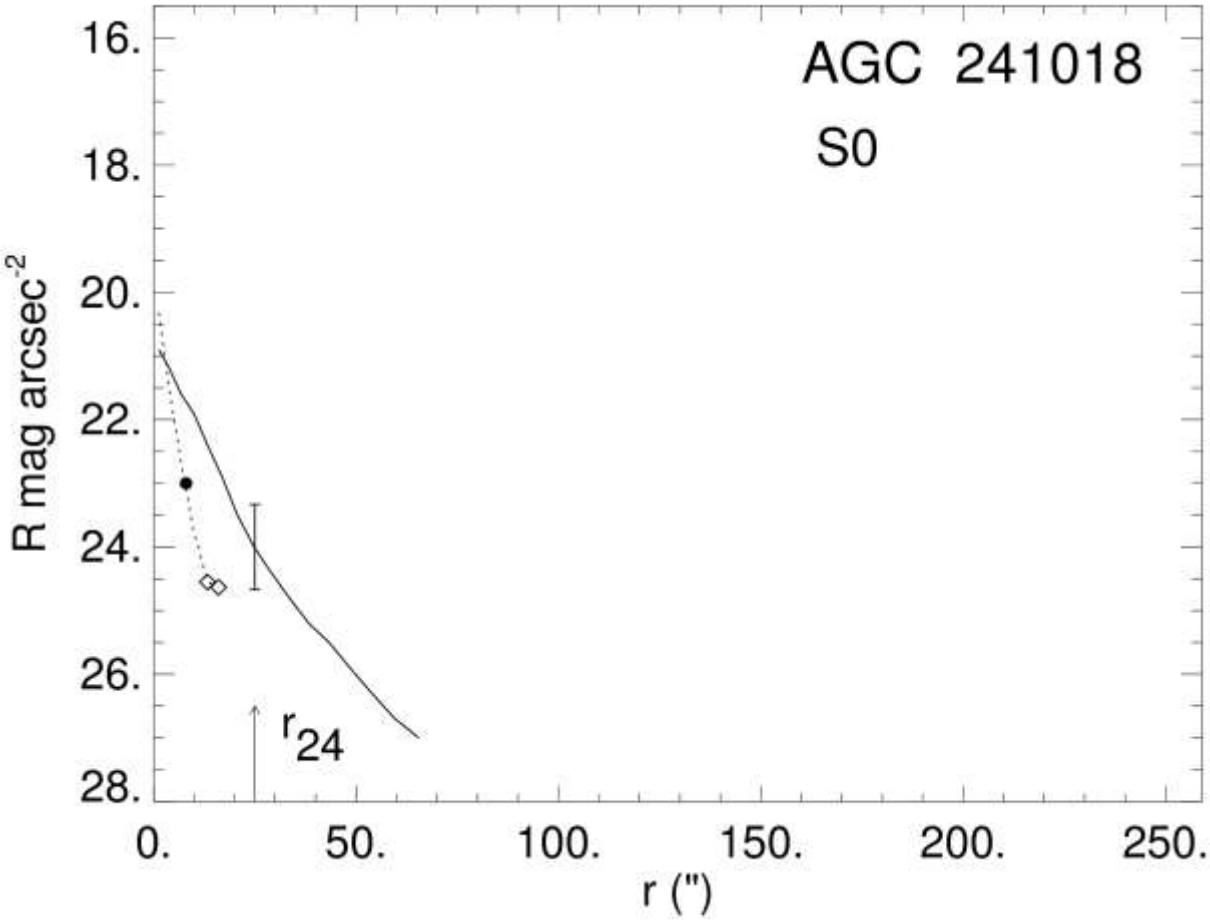

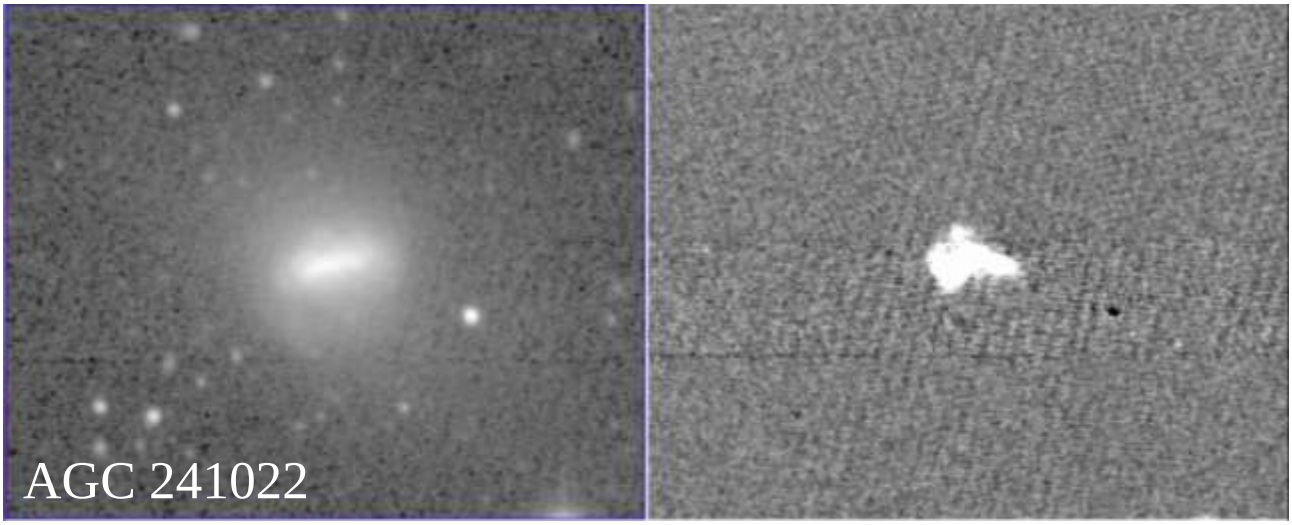

Image Reduced by Warrener, M. Union College Summer Research Paper

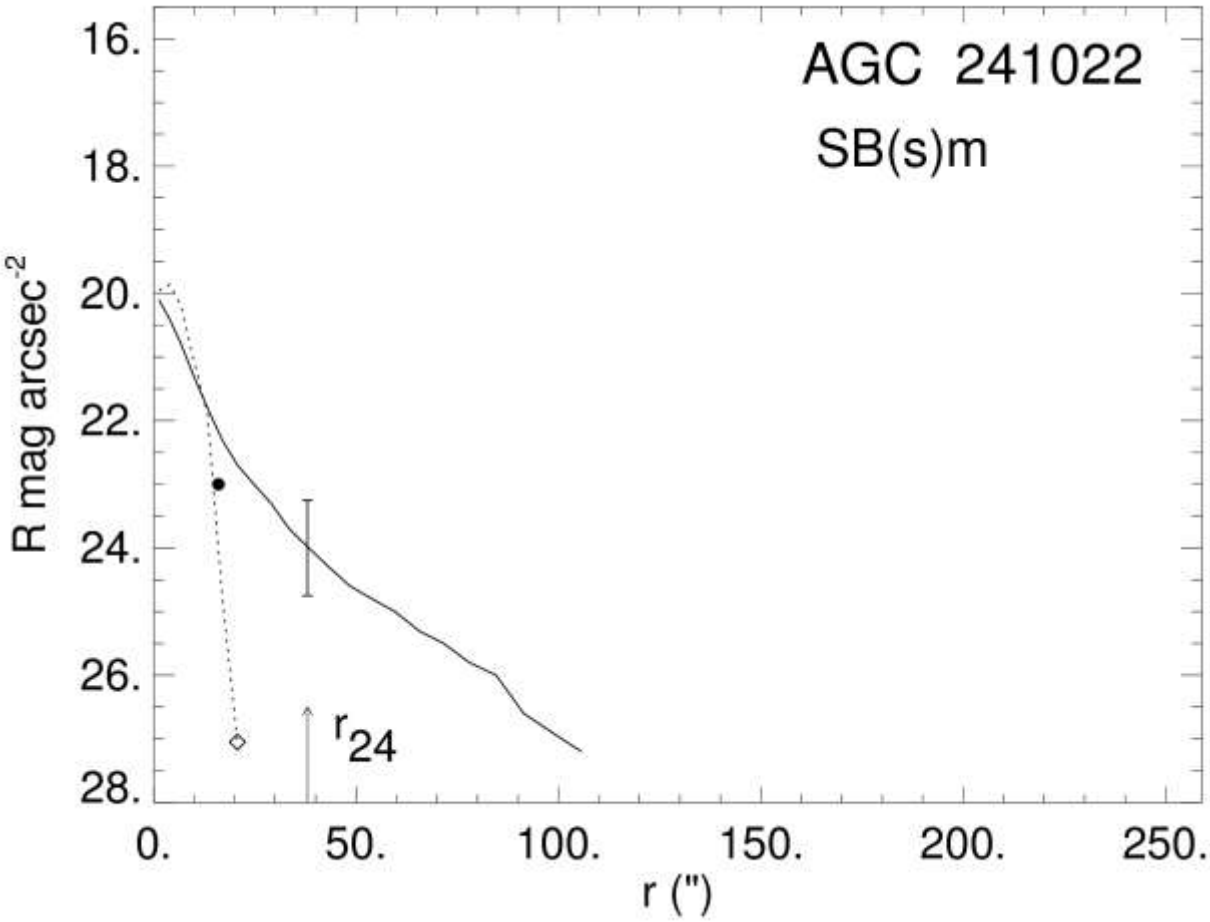

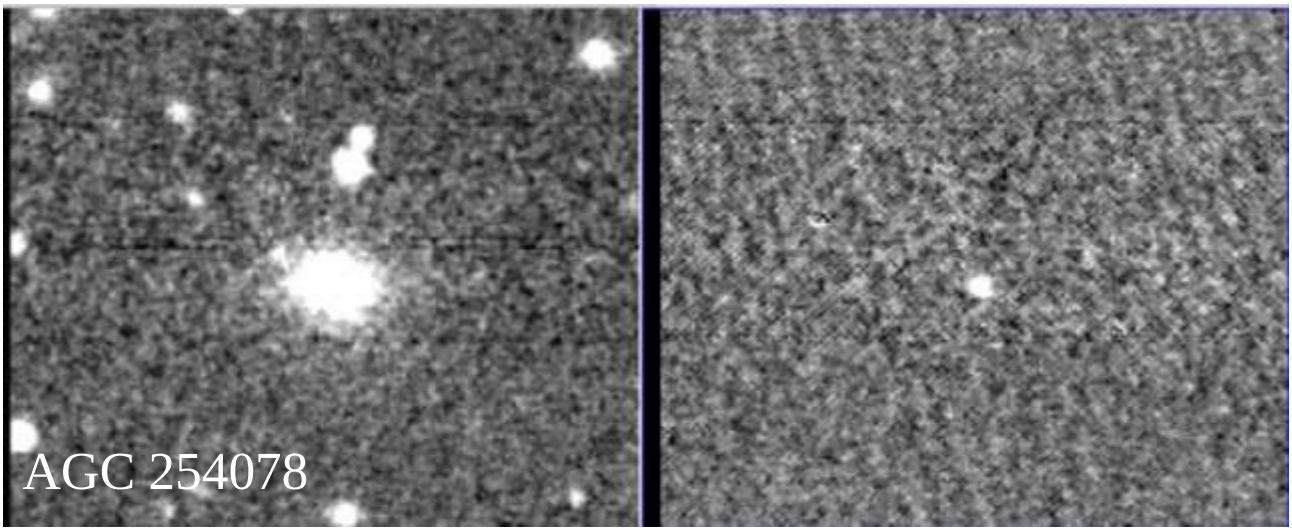

Image Reduced by Warrener, M. Union College Summer Research Paper

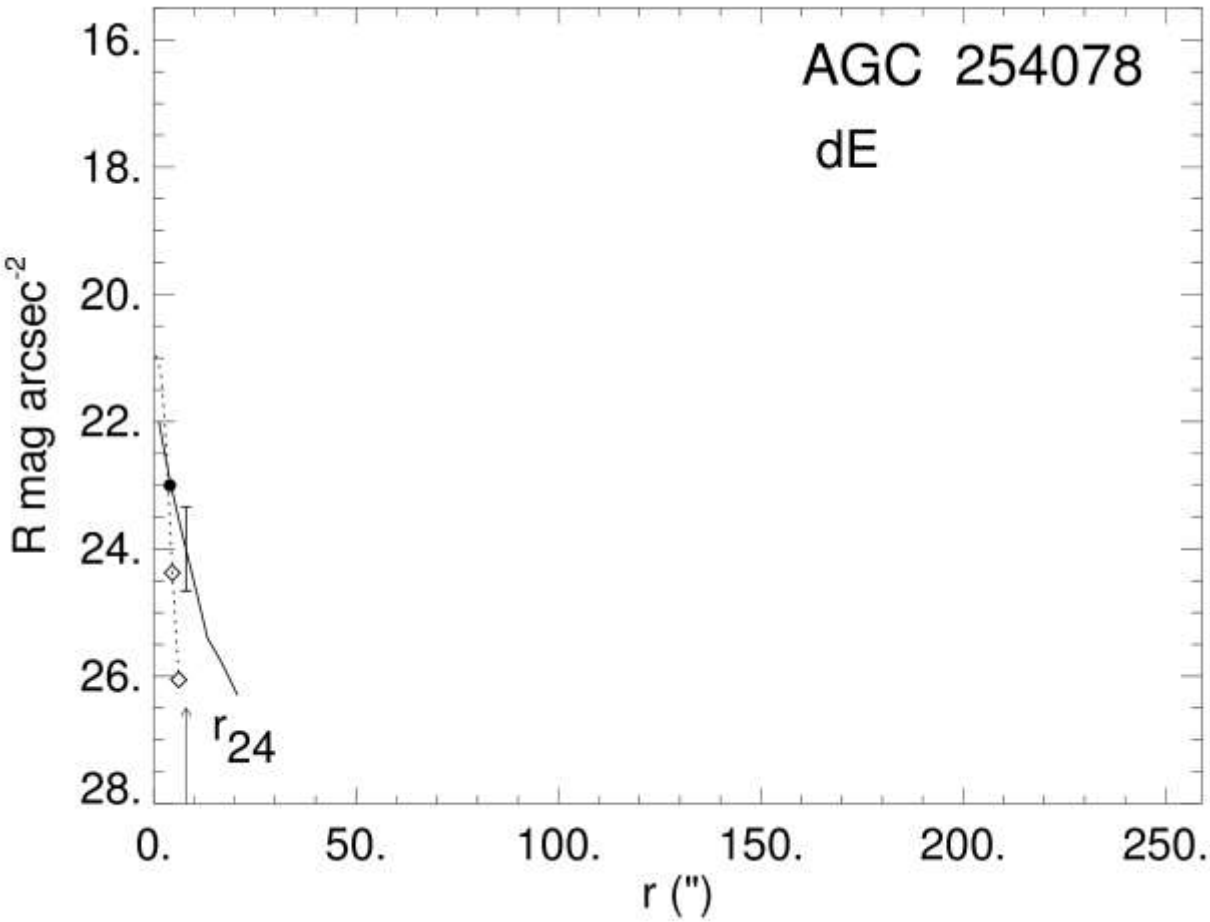

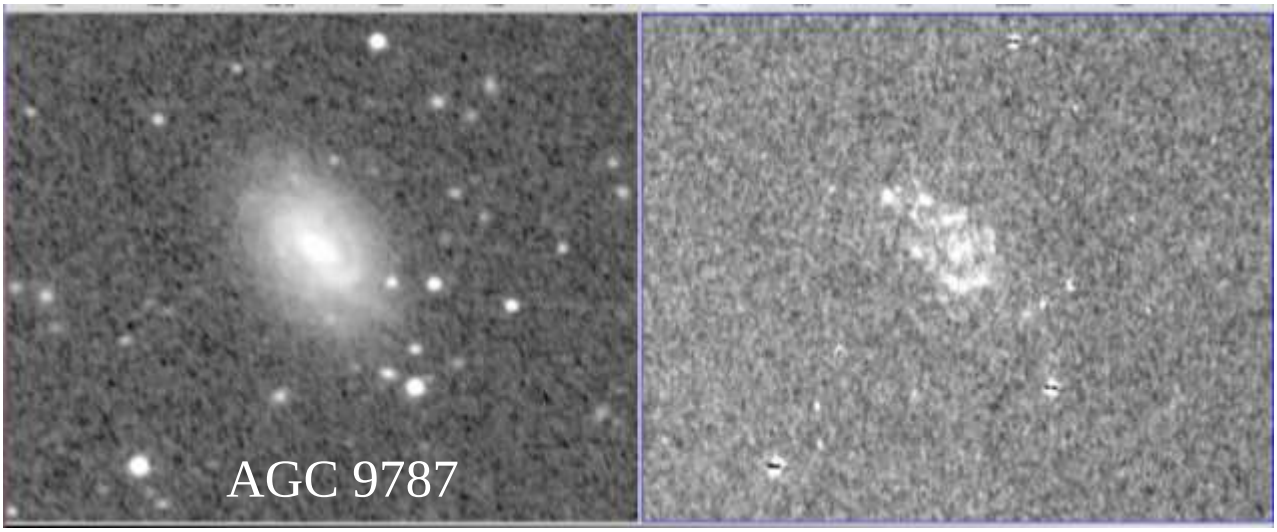

Image reduced by O'Brien, K. 2012 Union College Senior Thesis

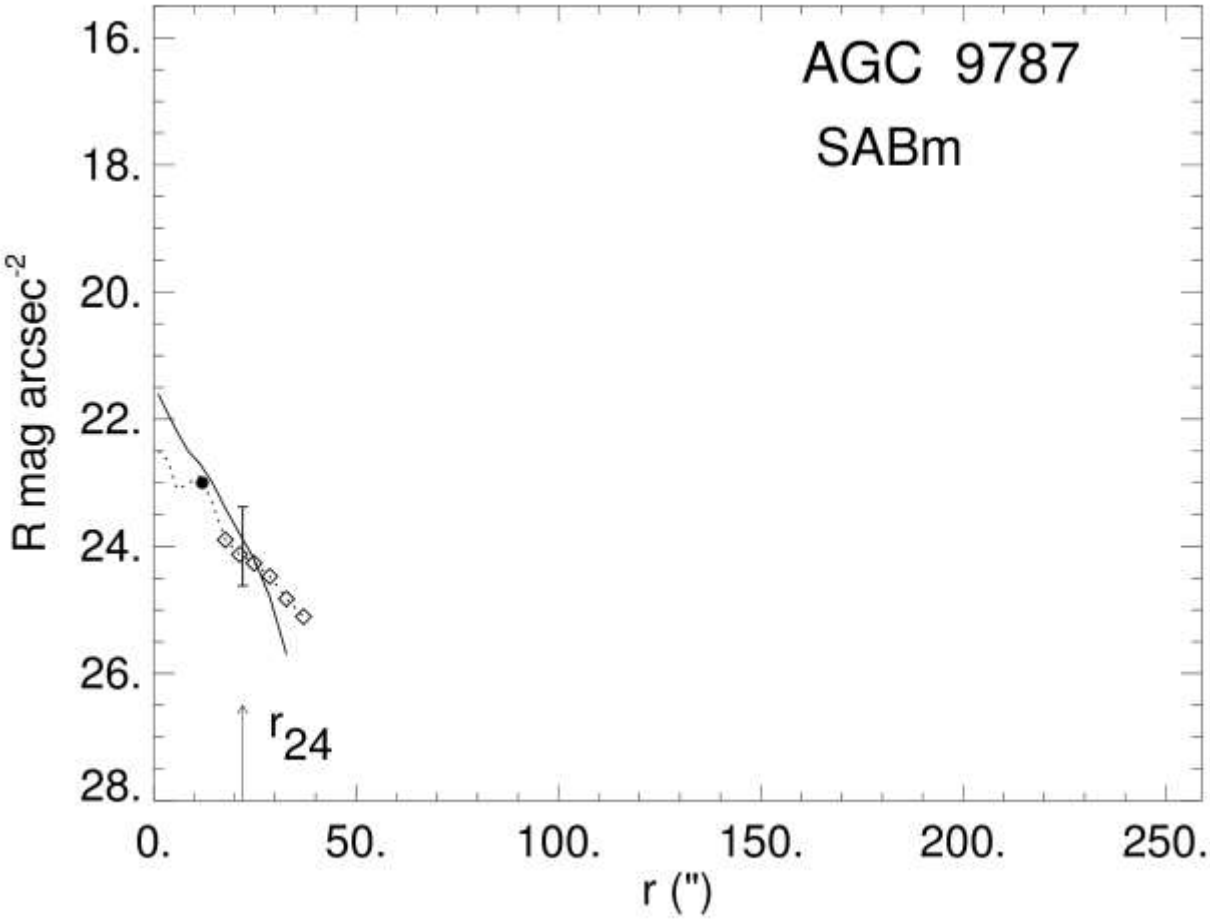

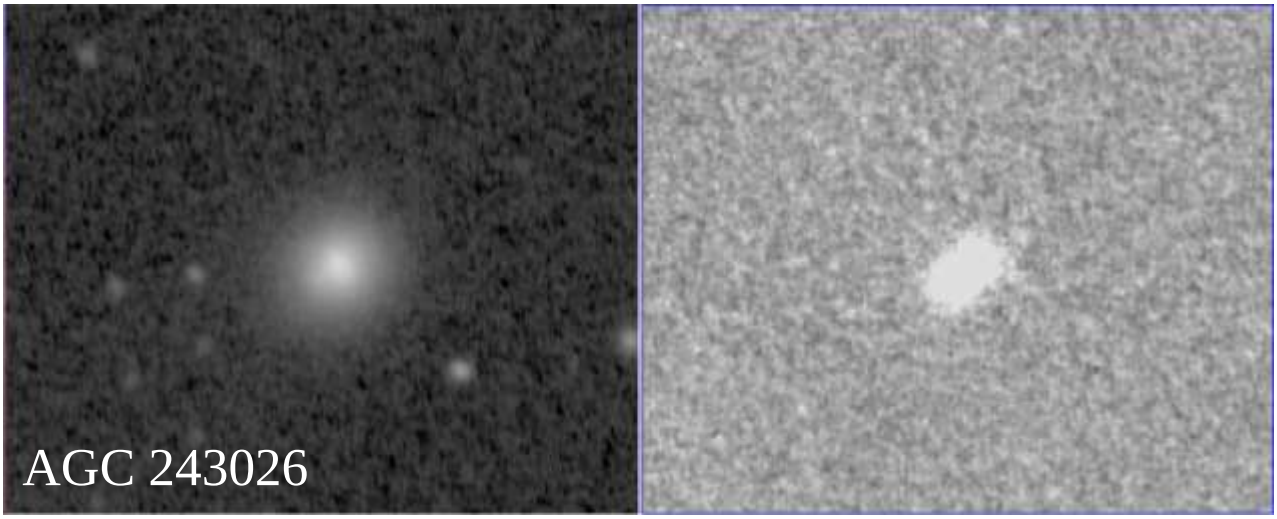

Image reduced by O'Brien, K. 2012 Union College Senior Thesis

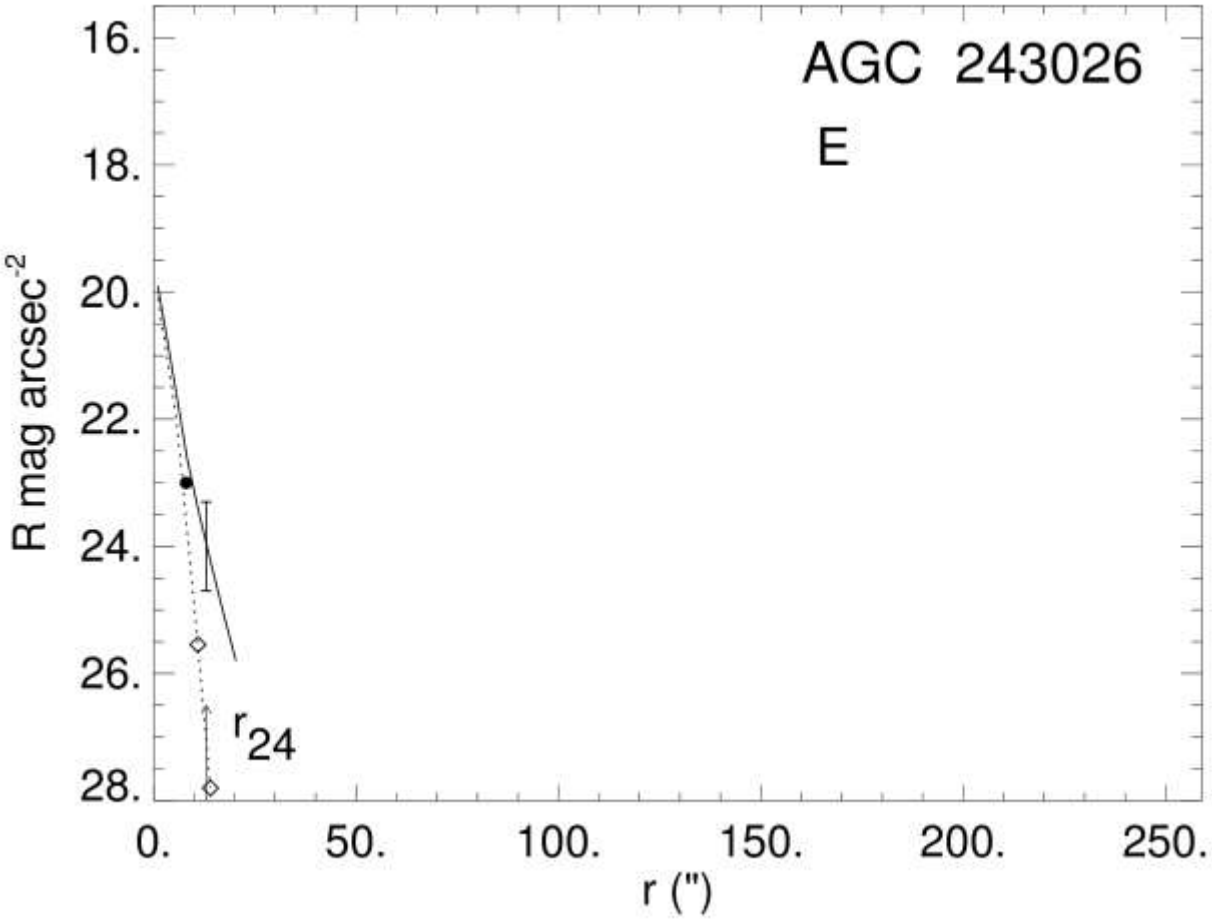

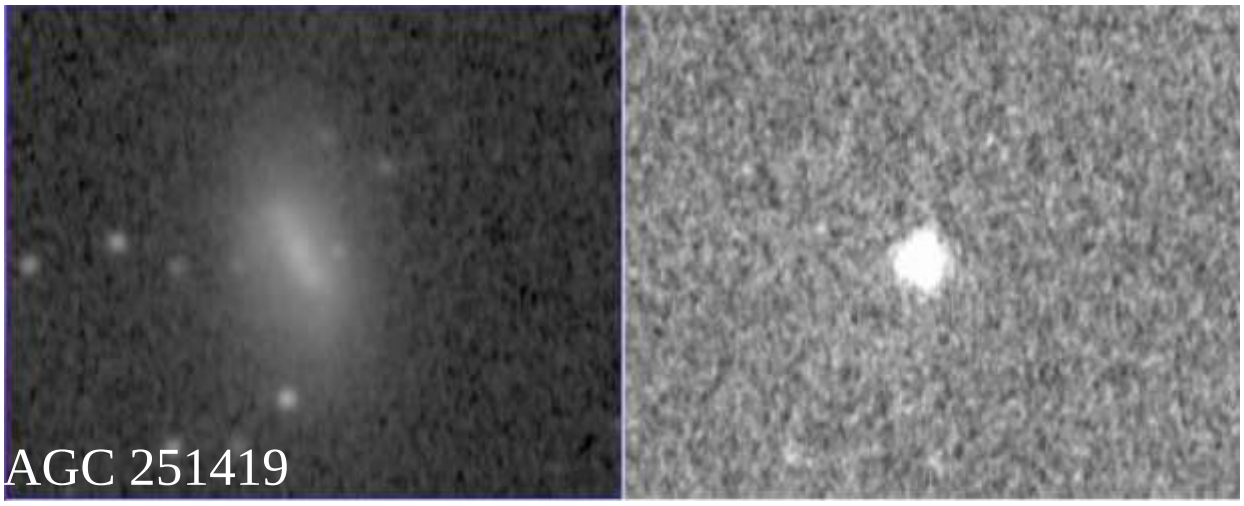

Image reduced by O'Brien, K. 2012 Union College Senior Thesis

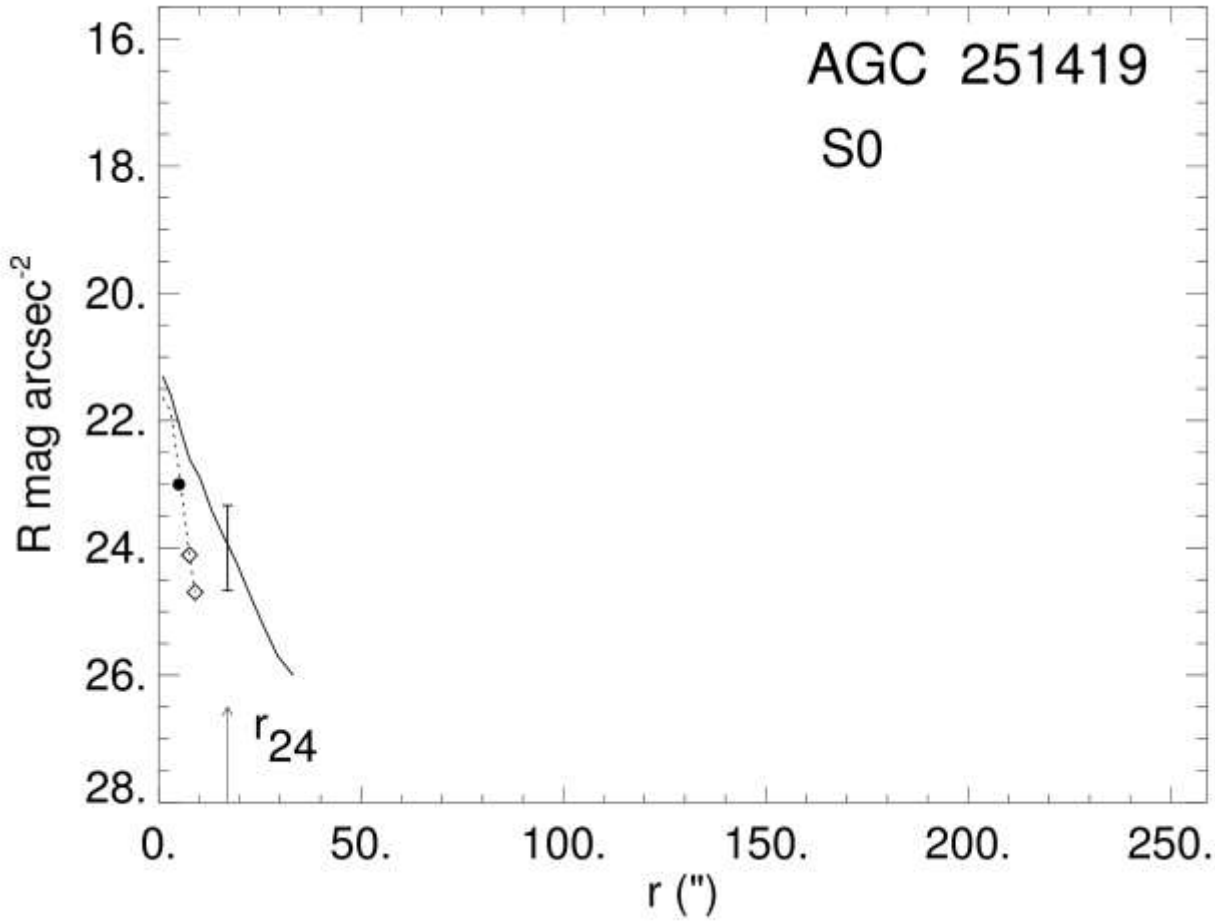

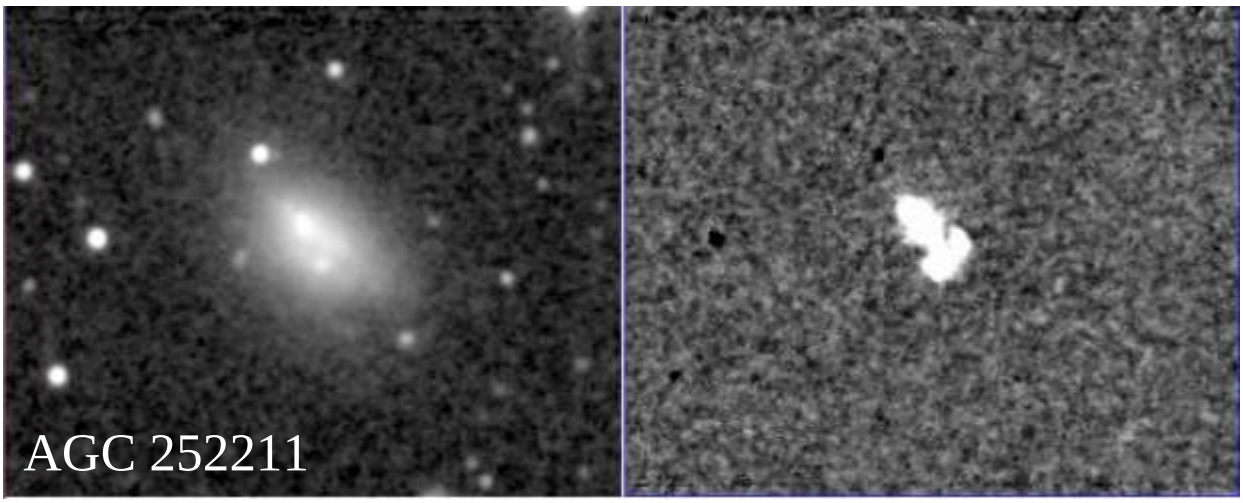
AGC 252211

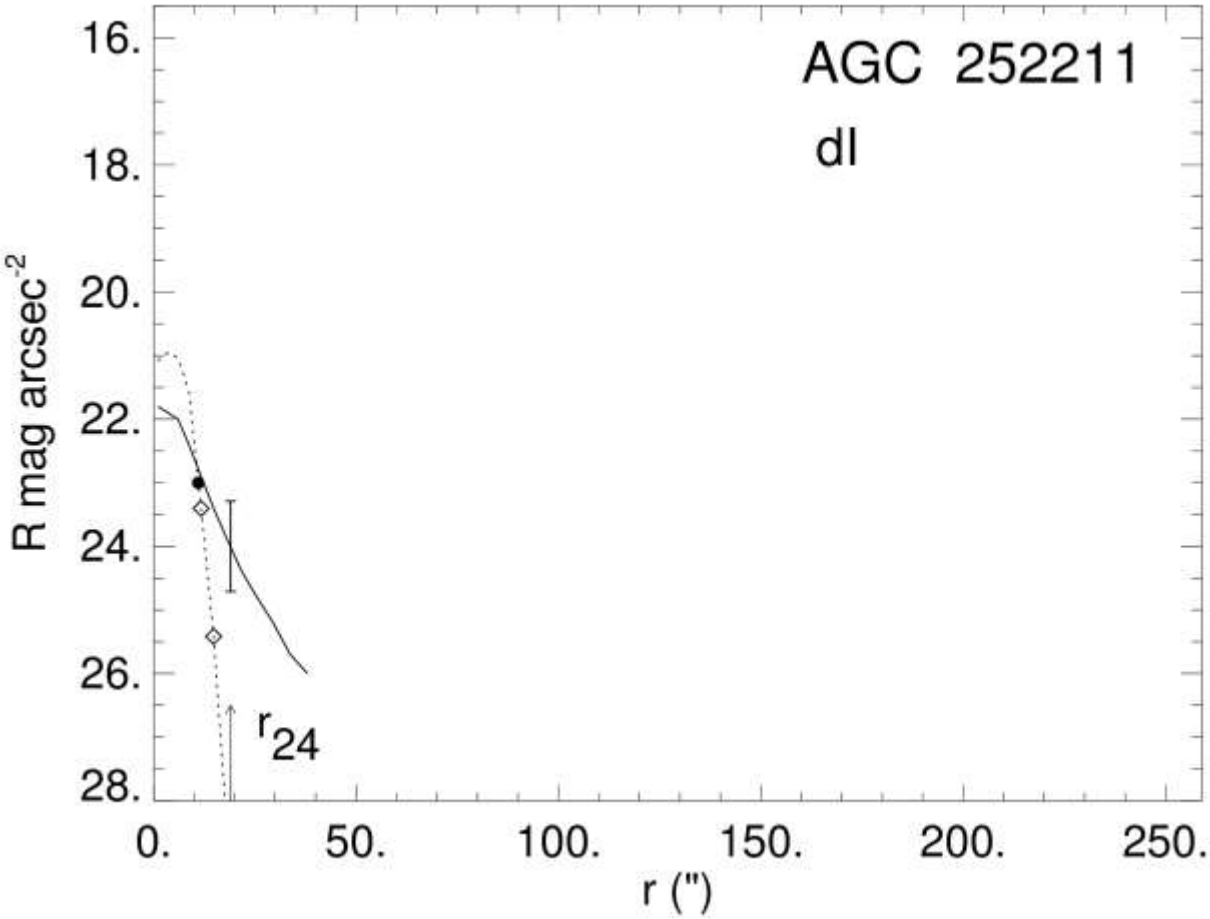
AGC 252211
dI
R mag arcsec^{-2}
16.
18.
20.
22.
24.
26.
28.
0.
50.
100.
150.
200.
250.
r (")
r_{24}

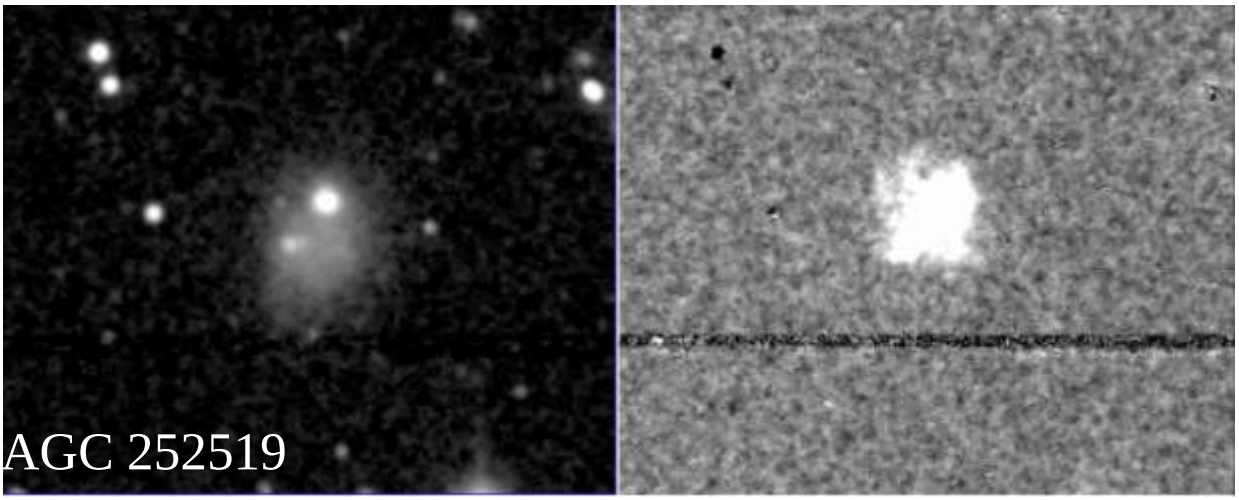
AGC 252519

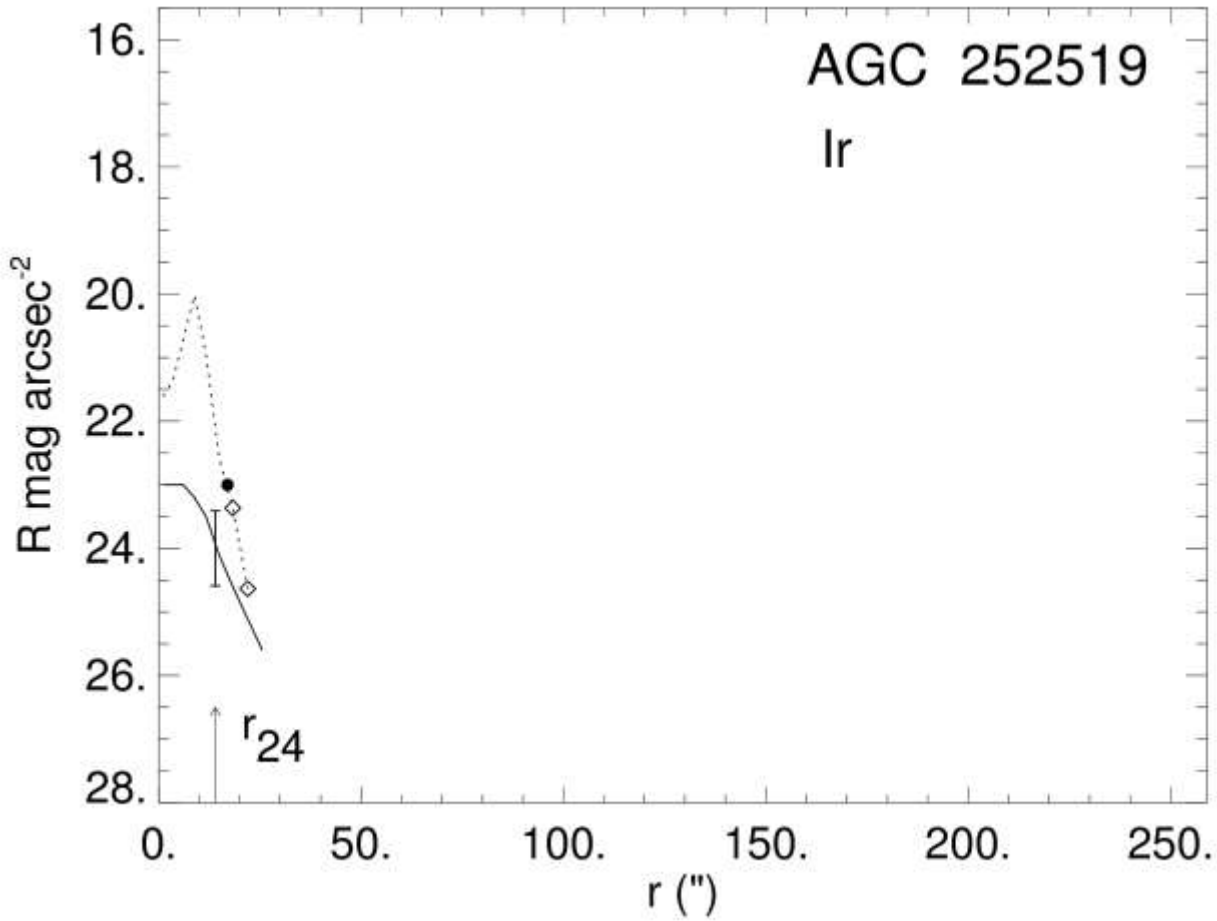
AGC 252519
Ir
R mag arcsec^{-2}
16.
18.
20.
22.
24.
26.
28.
0.
50.
100.
150.
200.
250.
r (")
r_{24}

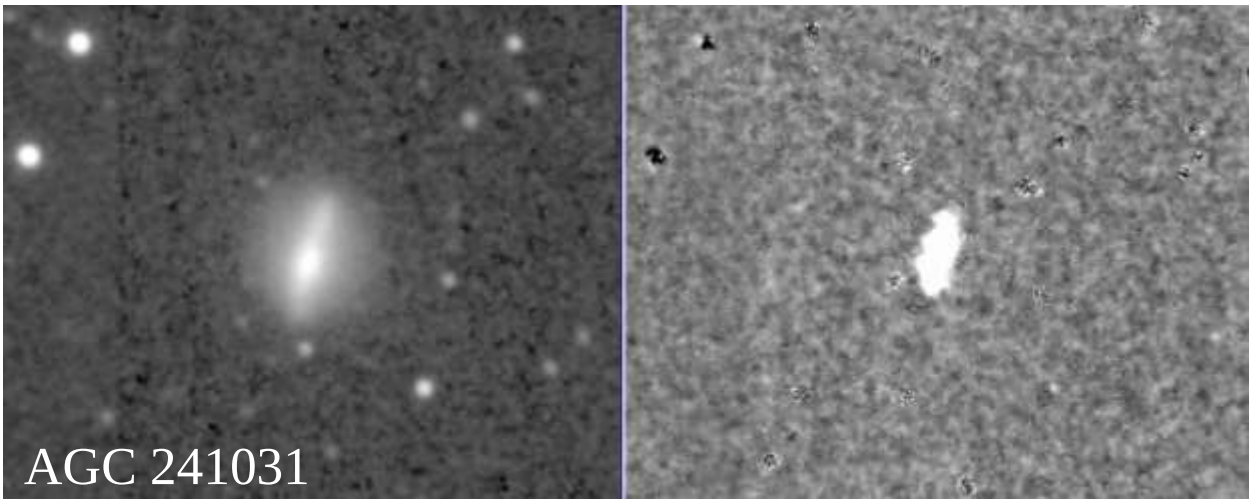
AGC 241031

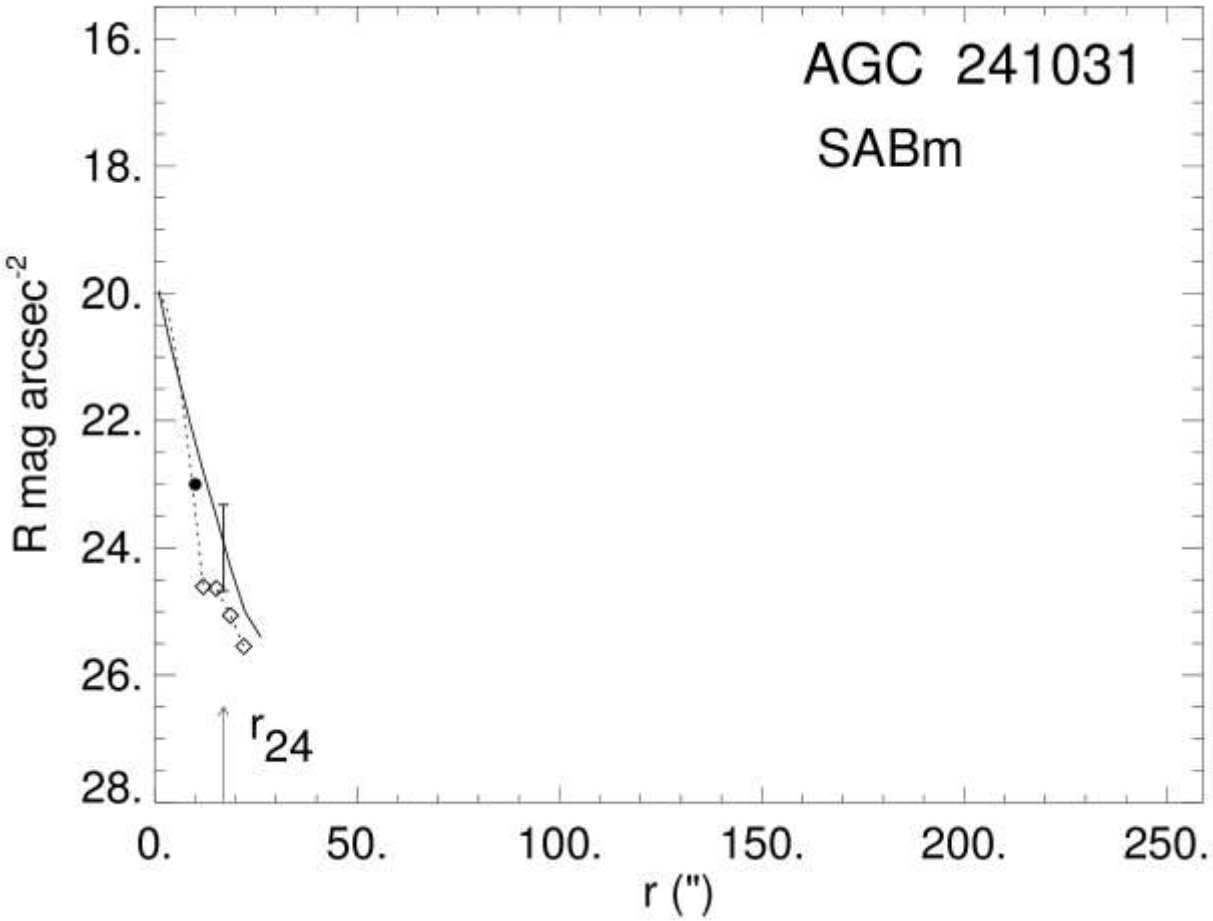
AGC 241031
SABm
R mag arcsec^{-2}
16.
18.
20.
22.
24.
26.
28.
0.
50.
100.
150.
200.
250.
r (")
r_{24}

From the radial profiles it is evident that out of the 23 galaxies, 7 have clearly truncated profiles (AGC 250105, 250103, 252550, 9655, 241018, 254078, 251419). A more detailed analysis of which galaxies are truncated appears in Section 3.6.2. Also note that several galaxies classified as early-type, AGC 252550, 254078, 9655, 243026, and 252211, show evidence of star formation. Additionally, it appears that AGC 9655 has some sort of outflow, which could be AGN activity.

3.4. Summary of Photometry Results

To date, the photometry programs have been run on 23 of the NGC 5846 member galaxies with Hα emission. Out of the 25 galaxies with detected Hα emission from the KPNO sample, photometry has been performed on 17 galaxies. AGC 252473, 252398, 9706, 258549, 258550, and 9715 have not yet been masked and AGC 253667 and 253645 had Hα emission too faint to successfully run the photometry program. Therefore, these galaxies are not included in this sample. Six NGC 5846 group galaxies with Hα obtained using CTIO have been added to the 17 KPNO galaxies making a total of 23 galaxies in the sample on which photometry has been performed. A summary of the photometry results, displaying the r_{24} value, total flux for the R filter image and the Hα image, the calculated star formation rate, and concentration (C_{30} and $C_{H\alpha}$) can be seen in Table 3.

Galaxy AGC Number	C_{30}	r_{24} (arcsec)	Total R Flux ($x10^{-18}$ erg cm^{-2} s^{-1})	Total Hα Flux ($x10^{-18}$ erg cm^{-2} s^{-1})	$C_{H\alpha}$	r17 (arcsec)	Log(SFR) (M_{solar}/year)
9746	0.26	37	$(2.186\pm0.007)x10^{6}$	$(2.6\pm0.2) \times 10^{4}$	0.18	32	-10.41
9751	0.21	16	$(4.67\pm0.03)x10^{5}$	$(9.6\pm0.1) \times 10^{4}$	0.03	73	-9.6
9760	0.14	11	$(4.10\pm0.06)x10^{5}$	$(7.6\pm0.4) \times 10^{4}$	0.07	9	-10.99

252399	0.29	12	$(4.81\pm0.05)\times10^{5}$	$(1.10\pm0.2)\times10^{4}$	0.34	12	-10.02
250105	0.39	20	$(2.80\pm0.01)\times10^{6}$	$(1.40\pm0.5)\times10^{4}$	0.20	10	-10.4
250103	0.42	22	$(2.21\pm0.01)\times10^{6}$	$(1.8\pm0.2)\times10^{4}$	0.40	12	-10.64
252555	0.29	19	$(2.114\pm0.009)\times10^{6}$	$(2.9\pm0.5)\times10^{4}$	0.21	17	-10
252550	0.25	6	$(1.69\pm0.02)\times10^{5}$	$(3.5\pm0.6)\times10^{3}$	0.30	6	-10.47
9573	0.41	37	$(1.0474\pm0.0004)\times10^{7}$	$(1.41\pm0.03)\times10^{5}$	0.14	29	-10
9574	0.46	53	$(2.2752\pm0.0007)\times10^{7}$	$(2.15\pm0.07)\times10^{5}$	0.10	57	-10.05
243743	0.4	11	$(6.58\pm0.01)\times10^{5}$	$(9.6\pm0.8)\times10^{3}$	0.39	8	-10.51
9645	0.46	95	$(6.309\pm0.005)\times10^{7}$	$(2.8\pm0.3)\times10^{5}$	0.19	56	-10.22
9655	0.52	160	$(1.886\pm0.002)\times10^{8}$	$(9.2\pm0.2)\times10^{5}$	0.85	28	-14.68
9661	0.32	37	$(1.130\pm0.001)\times10^{7}$	$(1.6\pm0.1)\times10^{5}$	0.34	26	-9.62
241018	0.36	25	$(2.574\pm0.007)\times10^{6}$	$(6.0\pm0.6)\times10^{3}$	0.50	8	-11.19
241022	0.47	38	$(1.101\pm0.003)\times10^{7}$	$(8.5\pm0.1)\times10^{4}$	0.38	16	-10.28
254078	0.41	8	$(4.17\pm0.03)\times10^{5}$	$(2.3\pm0.5)\times10^{3}$	0.42	4	-10.7
9787	0.28	22	$(2.305\pm0.003)\times10^{6}$	$(2.2\pm0.7)\times10^{4}$	0.16	12	-10.34
243026	0.55	13	$(2.0204\pm0.002)\times10^{6}$	$(1.1\pm0.1)\times10^{4}$	0.49	8	-10.76
251419	0.36	17	$(1.084\pm0.002)\times10^{6}$	$(2.7\pm0.4)\times10^{3}$	0.34	5	-11.33

252211	0.3	19	$(1.86\pm0.01) \times 10^6$	$(1.9\pm0.4) \times 10^4$	0.24	11	-10.86
252519	0.19	14	$(8.47\pm0.08) \times 10^5$	$(6.8\pm0.5) \times 10^4$	0.12	17	-9.26
241031	0.49	17	$(3.16\pm0.01) \times 10^6$	$(2.6\pm0.7) \times 10^4$	0.48	10	-10.18

Table 3: *List of NGC 5846 galaxies included in this sample, with photometry results provided for each.*

3.5. Photometry Analysis For NGC 5846 Galaxies

To first get a sense of the galaxies in the sample, a color-magnitude diagram can provide a rough measure of the star formation of the galaxies based on color (g-i in this case). Figure 9 is a color magnitude diagram plotting our star-forming NGC 5846 sample (red), other NGC 5846 galaxies (blue) (including galaxies in the central group region and the outskirts), and other AGC galaxies with data from the NSA catalogue (grey). In the color magnitude diagram the y-axis (g-i) represents how red or blue a galaxy is (with redder being higher) and the x-axis represents the absolute magnitude (with higher luminosity galaxies being farther to the right). In a color-magnitude diagram, most galaxies fall into two main areas. Red galaxies tend to lie along a diagonal line called the "red sequence" with brighter galaxies having the reddest colors. Blue galaxies tend to fall in a less defined clump, known as the "blue cloud". The red sequence and the blue cloud are outlined in Figure 9. These two regions are separated by an area with relatively few galaxies, which is called the "green valley". The red sequence and blue cloud can be seen in the large NSA/AGC sample in Figure 9. Note that while the NGC 5846 sample extents to fainter magnitudes, the NSA comparison sample is complete only to a magnitude of -17.7 and therefore there are few grey points at fainter magnitude.

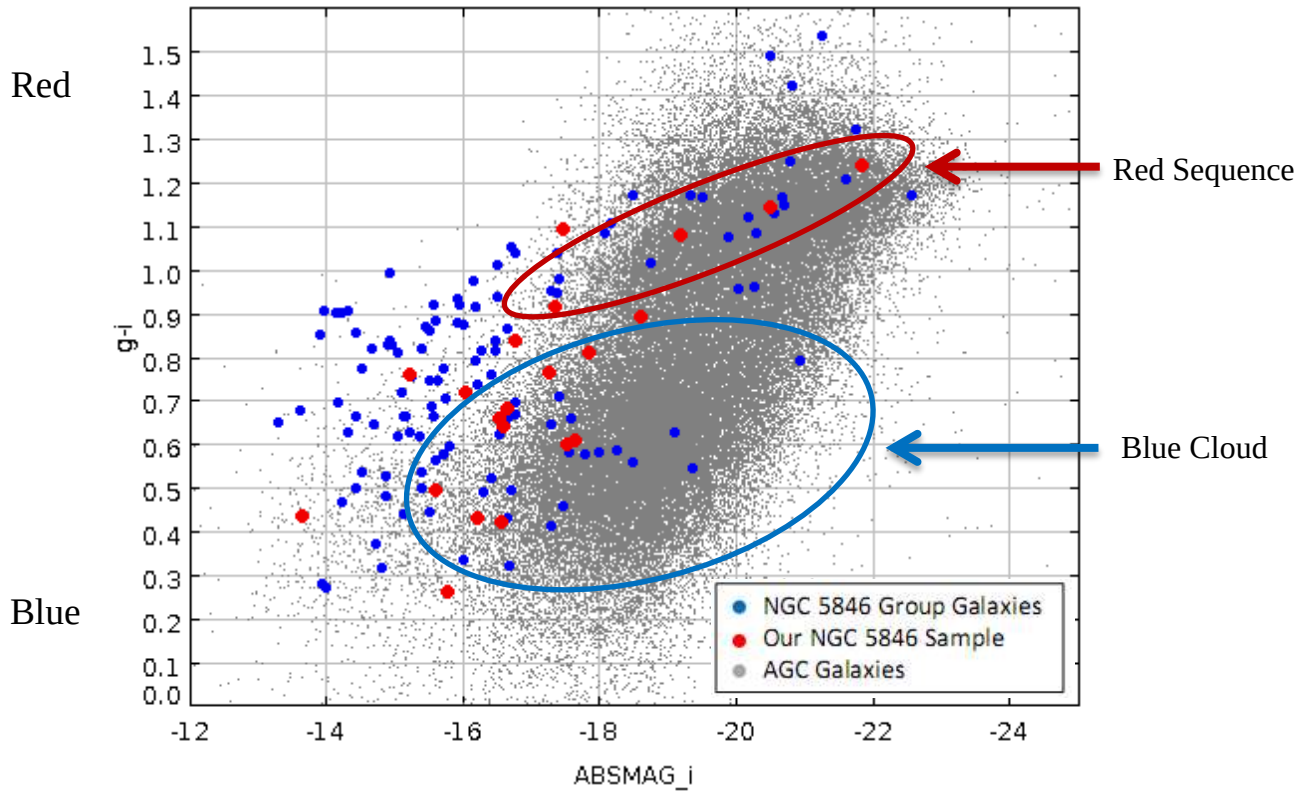

Figure 9: *A color-magnitude diagram for the NGC 5846 galaxies (blue), our NGC 5846 sample (red), and other AGC galaxies in the NSA (grey). The NSA comparison sample is complete only to a magnitude of -17.7. The red sequence and blue cloud are outlined.*

Figure 9 shows that most of the NGC 5846 sample falls at fainter magnitudes and is therefore made up of rather low-mass galaxies. It also shows that about 22% of the sample falls in the red sequence (AGC 9655, 9645, 9574, 250103, and 241018). There appears to be an absence of galaxies in the brighter part of the blue cloud as well. This is consistent with downsizing, in which more massive galaxies become passive (i.e., star formation ceases or decreases) more quickly than less massive galaxies (Cowie et al. 1996). Downsizing has also been shown to happen more quickly in over-dense environments (Bundy et al. 2006).

While AGC 9655, 9645, 9574, 250103, and 241018 all are on the red sequence, they each have star formation, with AGC 9655, 250103, and 241018 having truncated star forming disks. This demonstrates why color is not the best approach for measuring star formation – if we were using only color, we would mistakenly have classified these particular galaxies. Thus while a

color magnitude diagram can provide useful insights, Hα imaging is a much better method for studying star formation than global color.

Since the HI gas is the "raw material" needed for star formation, one would expect that galaxies with higher HI content will exhibit more star formation. Figure 10 examines the relationship between star formation rate and HI mass for the NGC 5846 sample. Here, the star formation rate is normalized by the stellar mass (obtained from the Sloan Digital Sky Survey, as discussed in Section 3.1), a quantity known as the specific star formation rate.

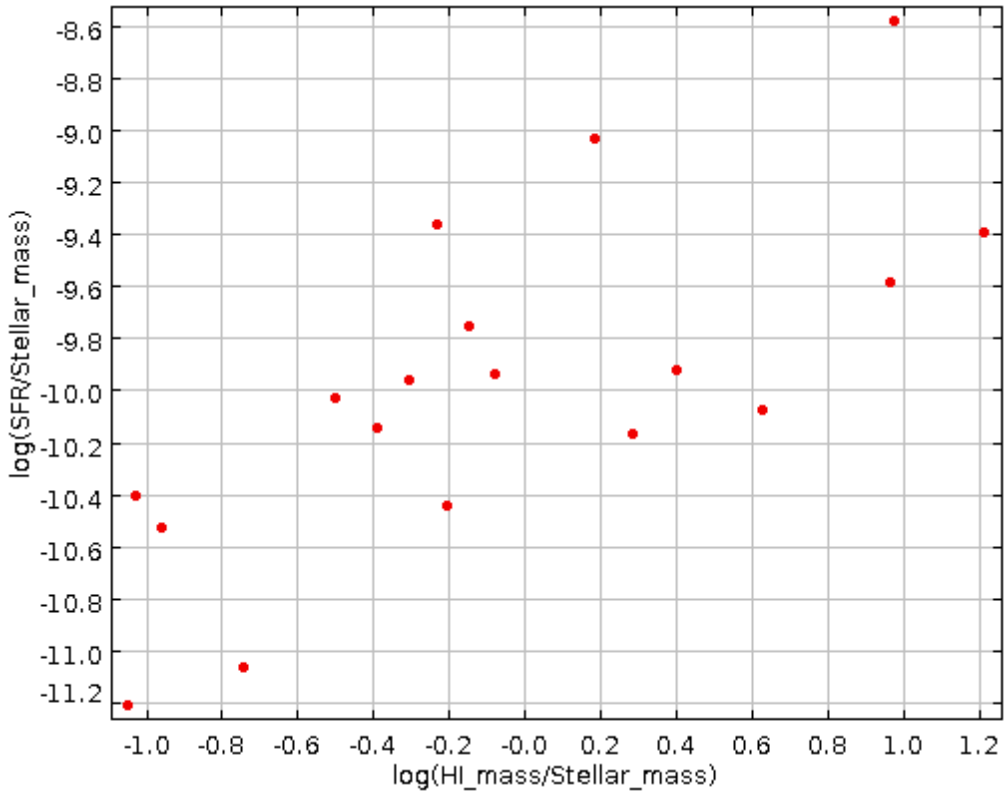

Figure 10: *The star formation rate as a function of HI mass (both normalized by stellar mass) for the NGC 5846 galaxy sample. Galaxies with more HI tend to have higher star formation rates.*

As seen in Figure 10, and as expected, the data show a trend that higher HI content corresponds to higher star formation rates.

The star formation rate can also be examined in relation to stellar mass, as seen in Figure

11. Figure 11 indicates a slight trend where the more massive galaxies in the sample have lower star formation rates. This relationship, where specific star formation rates are lower in more massive galaxies, has been found in many surveys, including Bauer et al. (2005) and Buat et al. (2008). It is also important to note that the galaxies in this sample are of generally low mass (in contrast, the Milky Way for example has a stellar mass of 4.6 x 10^{10} solar masses and the Large Magellanic Cloud disk has a stellar mass of 2.7 x 10^{9} solar masses) (Licquia & Newman 2013; van der Marel 2004).

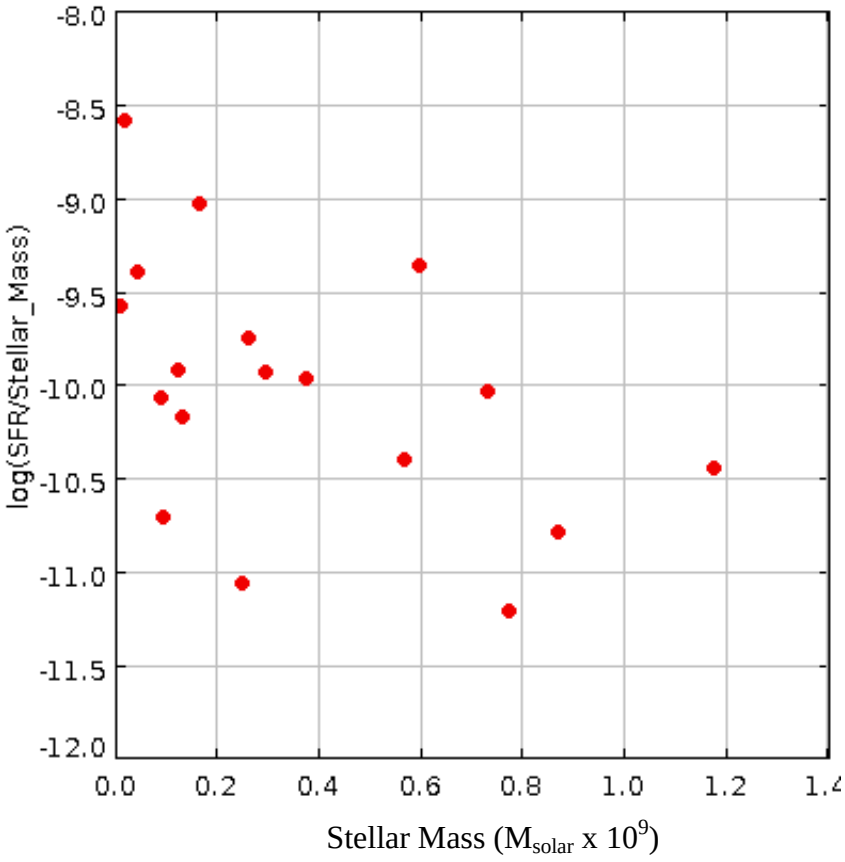

Figure 11: *The specific star formation rate (star formation rate normalized by the galaxy's stellar mass) is examined as a function of stellar mass for out sample of NGC 5846 group galaxies. There is a weak trend for more massive galaxies to have lower star formation rates.*

The position of a galaxy relative to the center of a group or cluster is a measure of the environment of a galaxy, and could indicate a stronger interaction with the intragroup medium.

Note, however, that galaxies projected near the center on the sky could be significantly behind or in front of the group and therefore not experiencing a strong environmental interaction. Figures 12 and 13 examine the relationship between a galaxy's apparent distance from the center of the NGC 5846 group and the galaxy's corresponding star formation rate and HI deficiency. The center of the NGC 5846 group refers to the group's X-ray center, as explained in Section 1.4.

Figures 12 and 13 show that there is no dependence between a galaxy's distance from the center of the group and a galaxy's star formation rate or HI deficiency. This is consistent with results found by Cote et al. (2009) for the Centaurus A group.

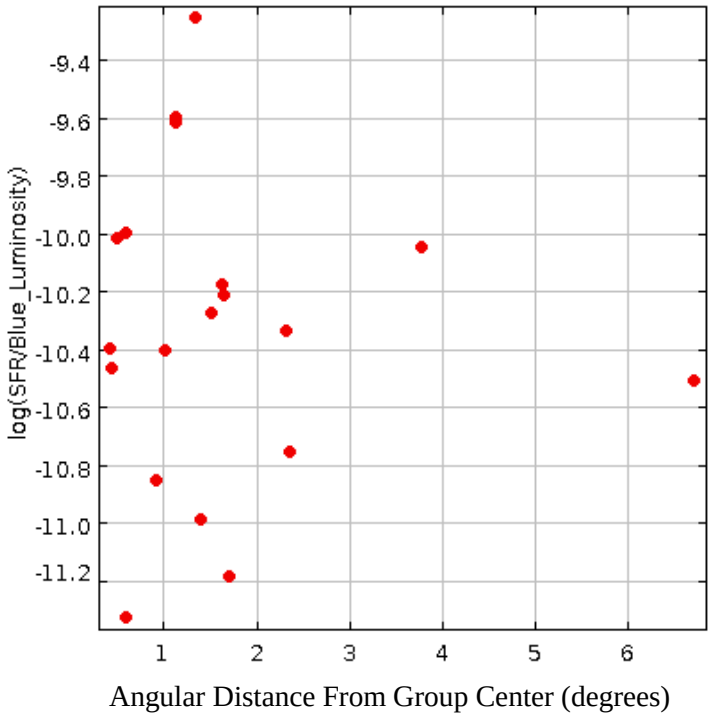

Figure 12: *The relationship between star formation rate and angular distance from the center of the group is examined for the NGC 5846 sample. There is no apparent correlation.*

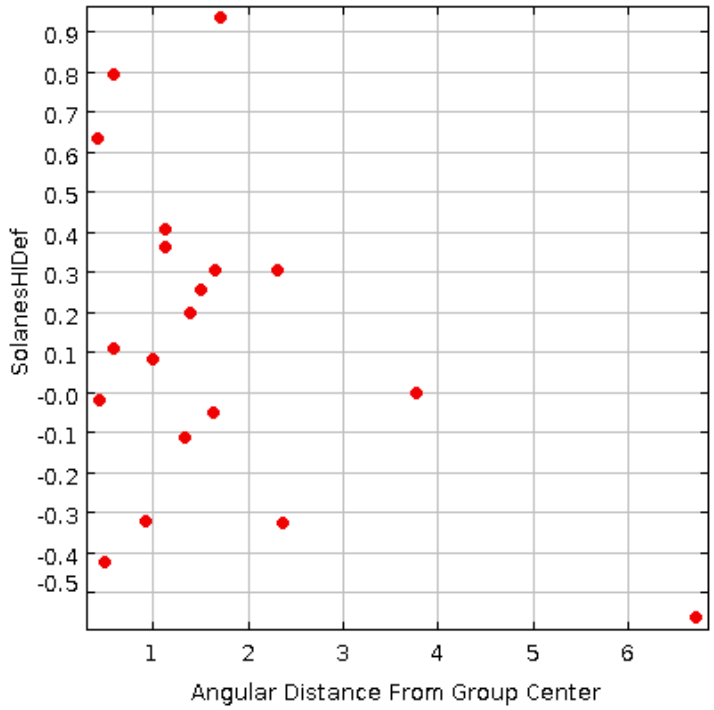

Angular Distance From Group Center (degrees)

Figure 13: *The relationship between HI deficiency and angular distance from the center of the group is examined for the NGC 5846 sample. There is no apparent correlation.*

Another useful method for analyzing galaxies is a Baldwin, Phillips, and Terlevich (BPT) diagram (Baldwin, Phillips, & Terlevich 1981). In a BPT diagram the ratio $[O_{III}]/H_{\beta}$ is compared to the ratio $[N_{II}]/H\alpha$. The resulting graph can then be used to determine if the ionization is due to star forming regions or an active galactic nucleus (AGN). The BPT diagram has a "sea gull" pattern, with galaxies whose emission is due to star formation falling on the left side of the plot and galaxies whose emission is due to AGN falling on the right side of the plot (as labeled in Figures 14 and 15). We can examine NGC 5846 galaxies using the NSA/SDSS data. However, SDSS spectroscopy fibers sample only within 3" of the center of each galaxy, which corresponds to 0.38 kpc at the distance of NGC 5846. Therefore, this method samples ionization only within this radius. Figure 14 is a BPT diagram with our NGC 5846 sample (red), other NGC 5846 galaxies (blue), and AGC galaxies (grey). Note that the blue points, the other NGC 5846

galaxies, also contains galaxies in the group outskirts.

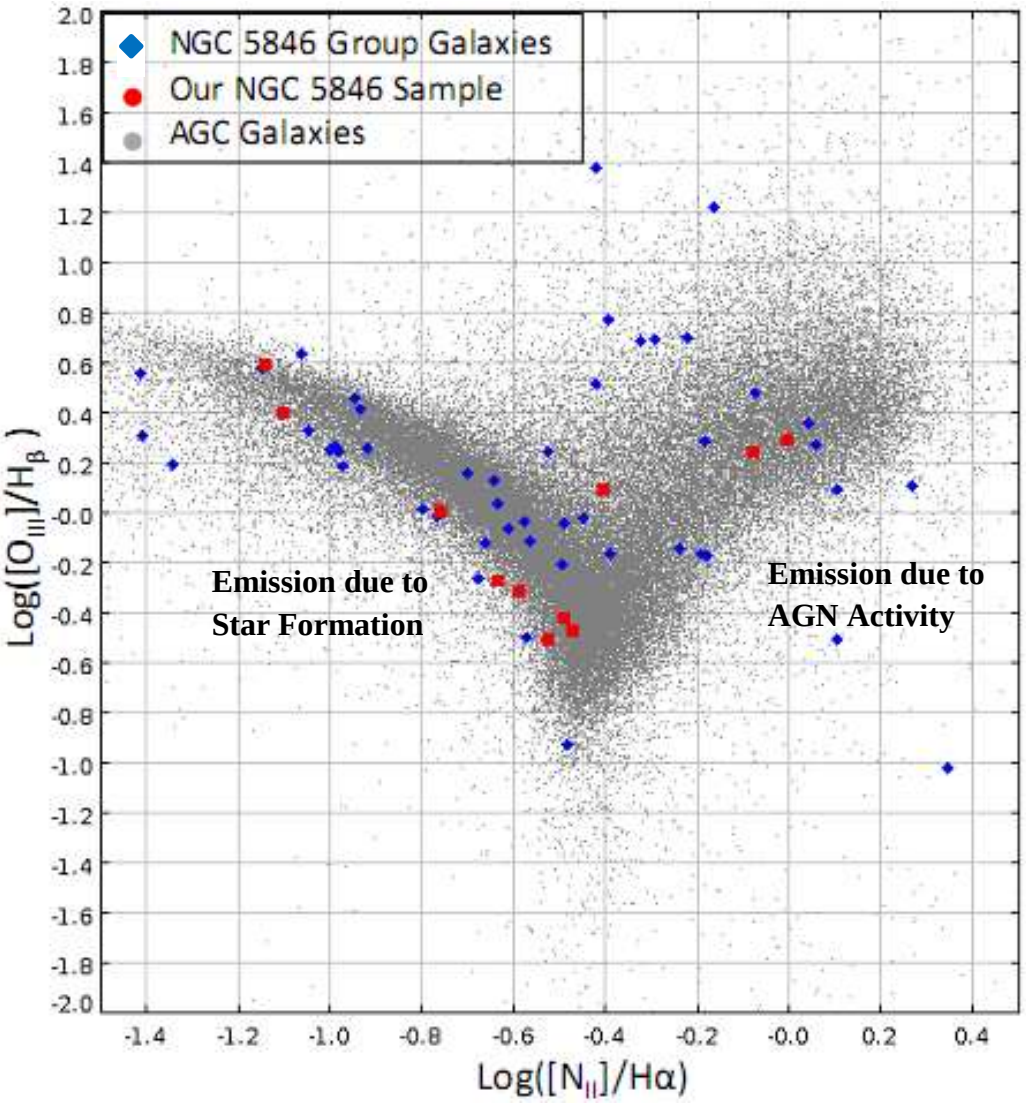

Figure 14: *A BPT (Baldwin, Phillips, & Terlevich) diagram for NGC 5846 galaxies (blue), our NGC 5846 sample (red), and other AGC galaxies (grey). BPT diagrams compare the ratios* $[O_{III}]/H_{\beta}$ *and* $[N_{II}]/H\alpha$*. Star forming galaxies fall on the left side of the plot and galaxies with emission due to AGN fall on the right side of the plot. Most of the galaxies with global star-forming activity also have ionization due to star formation in their nuclei.*

The BPT diagram in Figure 14 shows that the central regions of most of the NGC 5846 star-forming galaxies fall in the region of star forming activity (the left side of the "sea gull" pattern). Only two NGC 5846 galaxies from this sample, the galaxy pair ACG 9573 and 9574, fall along the right side of the "sea gull", indicative of AGN activity. Figure 15 is another BPT diagram, but with the "other" NGC 5846 galaxies (the blue points) only including the main

group region (the central region of NGC 5846).

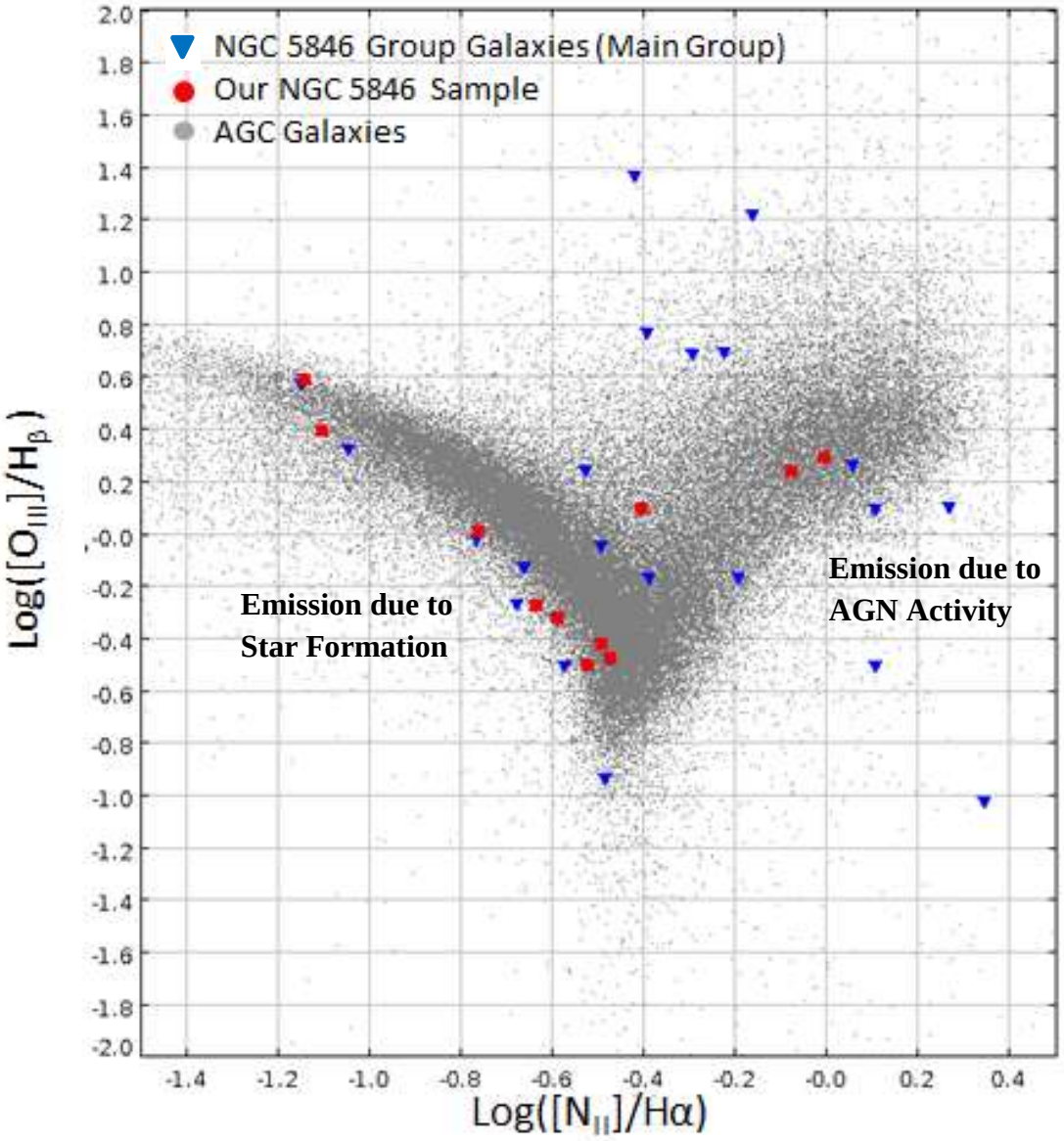

Figure 15: *A BPT diagram of our NGC 5846 sample (red), the rest of the main group region of NGC 5846 (blue), and other AGC galaxies (grey). Galaxies on the left side of the "sea-gull" pattern have emission due to star formation activity and galaxies on the right have emission due to AGN activity. Comparing to Figure 14 it is evident that the main group region of NGC 5846 has less star forming galaxies than the outskirts of the group.*

Comparing Figures 14 and 15, it is clear that the galaxies in the group outskirts heavily populate the star formation side of the sea-gull pattern. While the main group does have galaxies

that fall on the left side of the plot, the outskirts had a higher portion of galaxies with emission due to star formation activity.

3.6. NGC 5846 Group Galaxies in comparison to Galaxies in other Environments

We are also interested in how the NGC 5846 sample compares to galaxies observed in other studies. In this section I compare the observations to various studies of galaxies in a variety of environments, including other groups, clusters, and more isolated samples. These comparisons examine the effect of the group environment on star formation extents and rates. Comparisons are made between the NGC 5846 galaxies and galaxies from studies by Huang et al. (2012), Cote et al. (2009), van Zee et al. (2001), and Koopmann & Kenny (2004). Huang et al. (2012) examined the star formation properties of 229 dwarf galaxies, in a variety of environments, detected in the ALFALFA survey. Cote et al. (2009) examined 17 dI galaxies in the Centaurus A group, which, as mentioned in Section 1.4, is located 3.9 Mpc away with a velocity dispersion of 114±21 km/s (van den Bergh 2000). The survey done by van Zee et al. (2001) examined isolated dI galaxies. The NGC 5846 sample is also compared to more massive galaxies, such as the isolated spiral galaxies and Virgo Cluster spiral galaxies from Koopmann & Kenny (2004).

3.6.1. NGC 5846 Galaxies compared to ALFALFA Dwarf Galaxies, Centaurus A Group Dwarf Galaxies, and Isolated Dwarf Galaxies

Figure 16 examines the masses in the NGC 5846 sample as compared to the masses of the dwarf galaxies in Huang et al. (2012) sample.

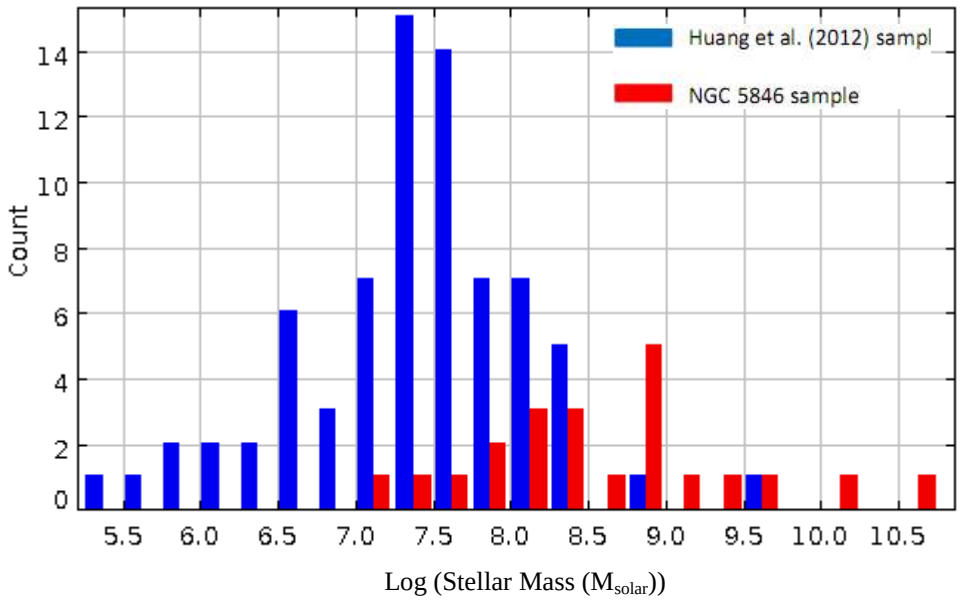

Figure 16: *The mass of our NGC 5846 sample (red bars) is compared to the mass of the Huang et al. (2012) sample (blue bars).*

The histogram in Figure 16 shows that the stellar mass of our sample is on average higher than the stellar mass of the Huang et al. (2012) galaxies. This is not surprising since the Huang et al. (2012) sample consists only of dwarf galaxies. However, when examining the HI masses normalized by stellar mass the NGC 5846 sample is found to have lower masses than the Huang et al. (2012) sample. This can be seen in Figure 17. This inverse relationship between gas fraction and stellar mass is typical, as seen for example in Catinella et al. (2010).

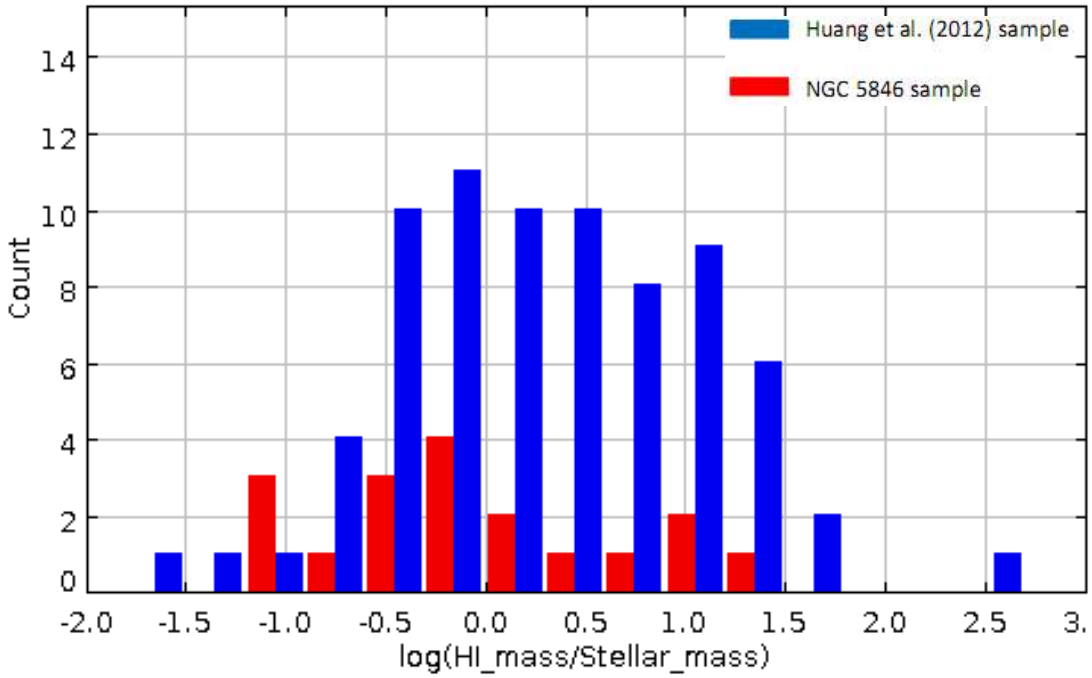

Figure 17: *The log of the HI mass (normalized by the stellar mass) is displayed for the NGC 5846 sample (red) and the Huang et al. (2012) galaxies (blue).*

With a smaller HI/(stellar mass) ratio than the dwarf galaxies analyzed by Huang et al. (2012), we could predict that the normalized star formation rates for NGC 5846 would be lower that the Huang et al. (2012) sample. As expected, this is seen in Figure 18, which compares the specific star formation (star formation divided by stellar mass) for the two samples.

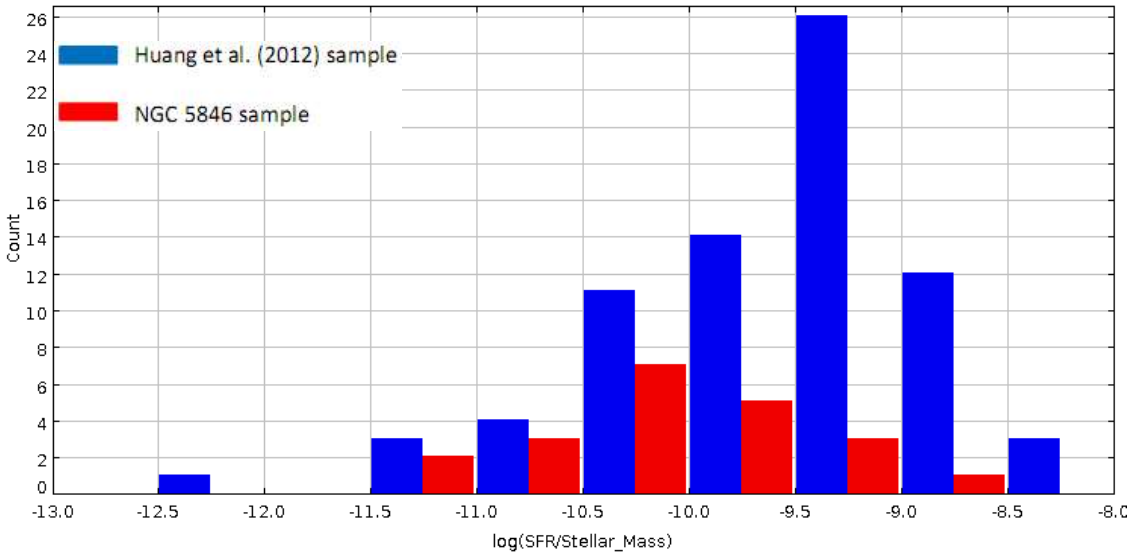

Figure 18: *The log of the star formation rate (normalized by stellar mass) is shown for both our NGC 5846 sample (red) and the Huang et al. (2012) galaxies (blue).*

We can also compare the relationship between star formation rates and HI content for both samples, shown in Figure 19.

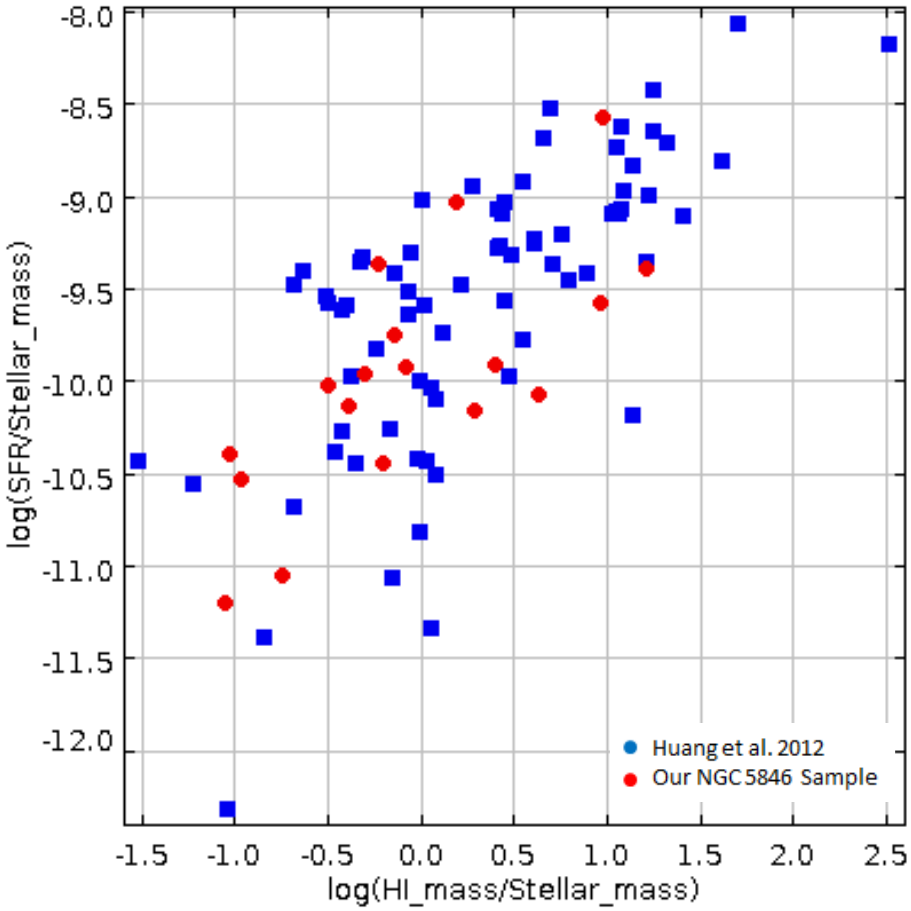

Figure 19: *The star formation rate normalized by stellar mass is examined as a function of HI mass normalized by stellar mass. In the above figure, the blue circles represent the Huang et al. (2012) sample and the NGC 5846 sample are the red circles.*

As expected, for both the NGC 5846 sample and the Huang et al. (2012) sample, there is a clear trend where the more HI massive galaxies have higher star formation rates. Figure 19 also shows that the NGC 5846 sample falls within the same range as the Huang et al. (2012) dwarf galaxies (which consists of galaxies in a mix of environments).

Additionally, it is interesting to note that for this sample of NGC 5846 galaxies, the galaxies with more HI mass than stellar mass lie either along the upper or lower edges of the region populated by the Huang et al. (2012) sample. It will be of interest to see if the results for

the other galaxies being studied by the UAT will follow this trend.

Figure 20 shows the NGC 5846 sample, along with the van Zee et al. (2001) isolated dI galaxies and the Cote et al. (2009) Centaurus A dI galaxies in an examination of star formation rates and HI mass both normalized by blue luminosity.

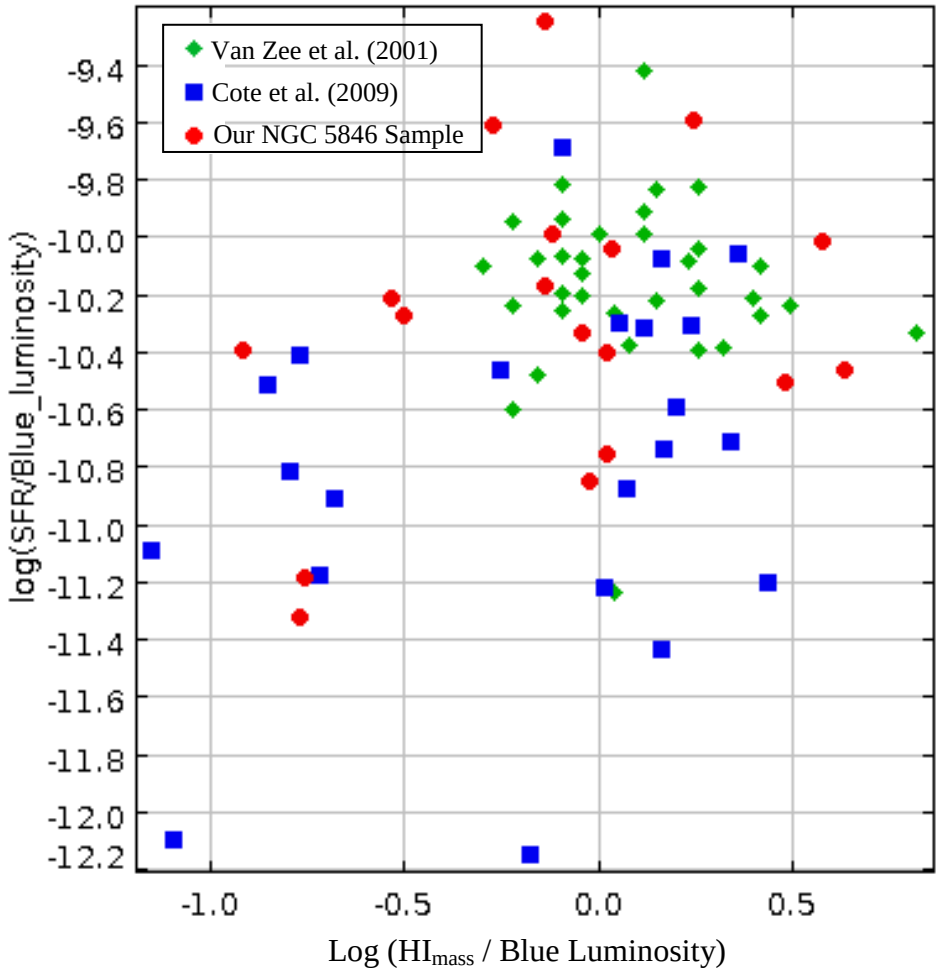

Figure 20: *The star formation rate is examined as a function of the HI mass (both normalized by blue luminosity). In the above figure, the red circles are the sample of NGC 5846 group galaxies, the blue squares are the Cote et al. (2009) galaxies, and the green diamonds are the van Zee al. (2001) sample.*

Figure 20 shows that for galaxies of similar HI gas content, the NGC 5846 sample has a larger range in star formation compared to the isolated galaxies (green diamonds from van Zee et al. 2001). Several are especially lower in star formation (AGC 252211, 243026, and 243743)

and several are significantly enhanced (AGC 9661, 252519, and 9751). The NGC 5846 sample has star formation and HI content comparable to the Centaurus A sample (Cote et al. 2009). Most of the galaxies from the van Zee et al. (2001) sample fall in a range of $\log(SFR/L_B)$ between -10.4 and -9.8.

3.6.2. NGC 5846 Sample Compared to Isolated and Virgo Spiral Galaxies

The NGC 5846 sample is also compared to sample isolated spiral galaxies and Virgo Cluster spiral galaxies (from Koopmann & Kenny 2004). Since many of the NGC 5846 sample were dwarf or low mass galaxies, keep in mind that these comparisons are to a more massive sample. Figure 21 compares the Hα fluxes as a function of C_{30}. The NGC 5846 sample is compared to isolated spiral galaxies in the top panel and to spiral galaxies from the Virgo Cluster in the bottom panel. The dashed lines show the upper and lower limits for isolated Sa-Sc galaxies.

In the top panel of Figure 21, the NGC 5846 sample falls mostly within the range of isolated galaxies. None are as low as Virgo early-type spirals, as can be seen in the bottom panel. None of the NGC 5846 galaxies are in the higher range of isolated spirals.

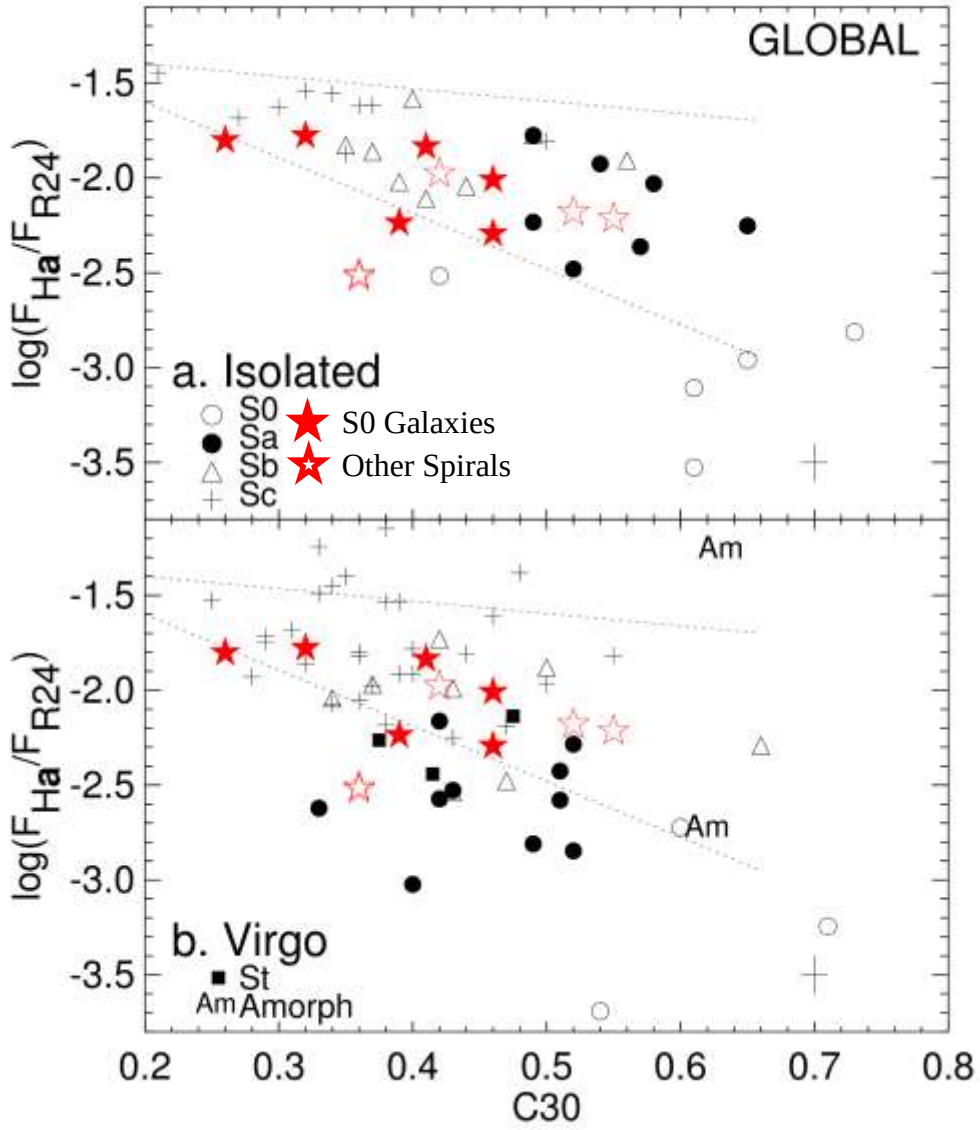

Figure 21: *The Hα flux, normalized by r_{24} is examined as a function of* C_{30}*. The top panel compares the NGC 5846 sample (red stars) to isolated spiral galaxies (from Koopmann & Kenney (2004) while the bottom panel compares the NGC 5846 sample (red stars) to spiral galaxies in the Virgo Cluster (from Koopmann & Kenney (2004)). The dashed lines show the region in which isolated Sa-Sc galaxies fall.*

This examination of Hα flux can be investigated as a function of radius in the galaxy, as seen in Figure 22. The top panels compare the star formation rates of NGC 5846 galaxies to those of isolated galaxies while the bottom panels compare the NGC 5846 sample to Virgo galaxies. The first column examines the Hα flux for the entire galaxy, the middle column

examines the Hα flux for the inner 30% of the galaxy, and the last column examines the Hα flux for the outer 70% of the galaxy. The dashed lines show the upper and lower limits for isolated Sa-Sc galaxies.

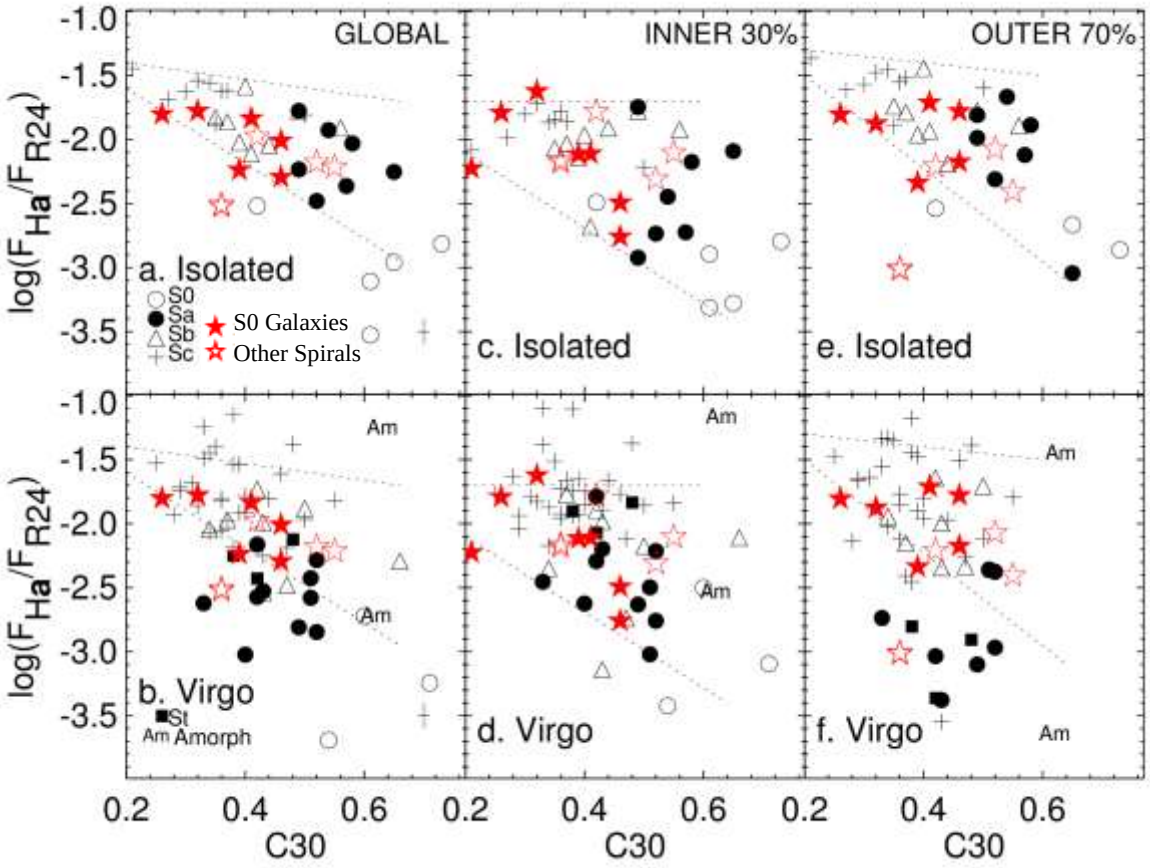

Figure 22: *The relationship between Hα flux and* C_{30} *concentration is examined between the NGC 5846 sample (red stars), isolated galaxies (top panels), and Virgo Cluster galaxies (bottom panels, from Koopmann & Kenney 2004). Moving from left to right, the first column looks at Hα flux throughout the entire galaxy, the second column investigates Hα flux for the galaxy's inner 30 percent, and the last column is the outer 70 percent of the galaxy. The dashed lines identify the upper and lower limits for isolated Sa-Sc galaxies.*

In the inner 30 percent of galactic disks $F_{H\alpha}/F_{r24}$ for the NGC 5846 sample spans a similar range as the Virgo galaxies. Additionally, in the inner 30 percent, some NGC 5846 galaxies are at the uppermost extreme compared to isolated galaxies. In the outer 70%, NGC 5846 galaxies fall towards the lower range of the isolated sample. This suggests that truncation

of the star-forming disk is the explanation for reduced star formation rates of some NGC 5846 galaxies.

In Figure 23 the NGC 5846 sample's surface brightness radial profiles (solid lines) are plotted alongside profiles from isolated spiral galaxies (dashed lines) from the sample of Koopmann & Kenney (2004). Surface brightness traces the ratio of star formation to stars in the disk. The galaxies are grouped together into 4 boxes based on C_{30} concentration and chosen by Koopmann & Kenney (2004) to roughly trace S0, Sa, Sb, and Sc galaxies, respectively. Most of the NGC 5846 galaxies are of lower concentration and lower mass than the isolated sample of Koopmann & Kenny (2004). In Figure 23, it is evident that a number of galaxies in the NGC 5846 sample have radial profiles that are more truncated than those of the isolated galaxies. This is interesting because lower mass galaxies tend to have higher overall star formation rates. However, there have been few studies of the typical radial extents of lower mass galaxies and thus this result should be confirmed by comparing similar mass galaxies.

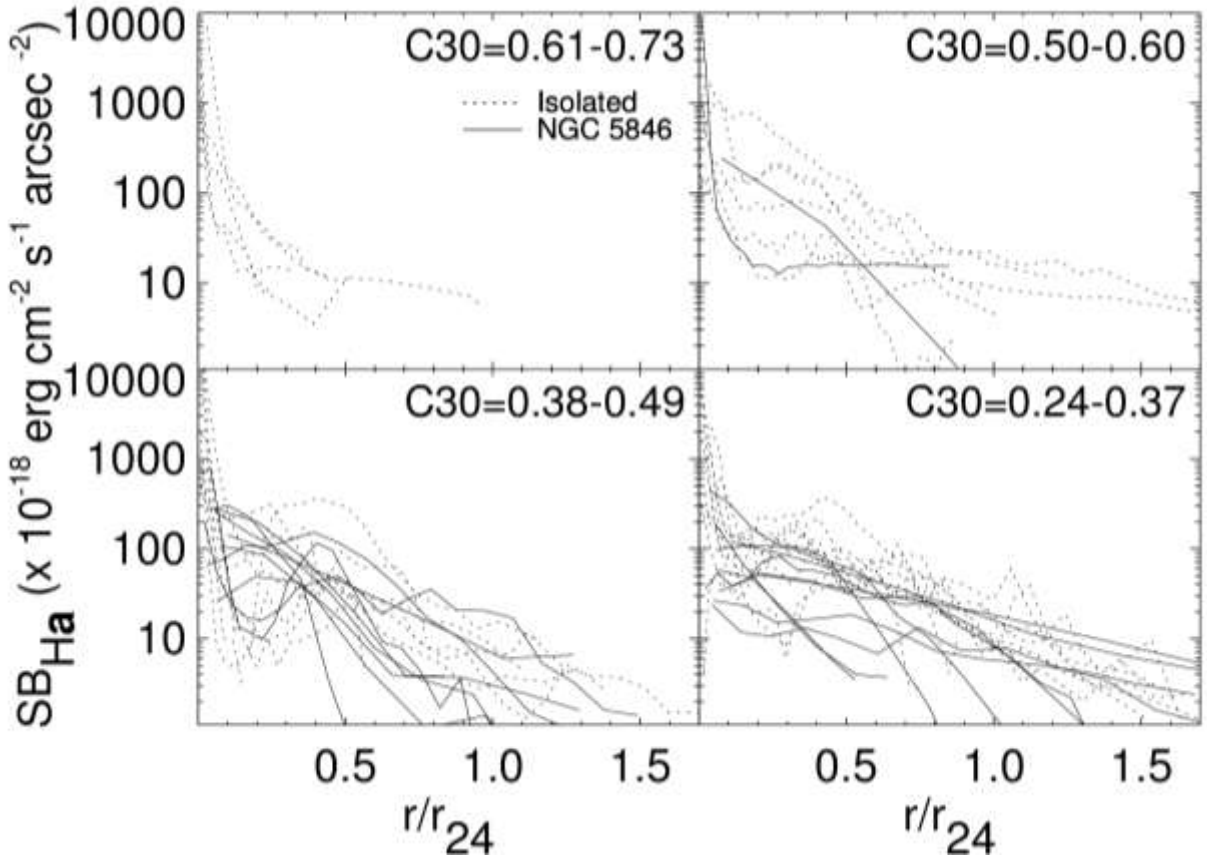

Figure 23: *The radial profiles, normalized by r_{24}, for our sample (solid lines) are compared to radial profiles from isolated galaxies (dashed lines) from the sample of Koopmann & Kenney (2004). A number of galaxies display truncated profiles compared to the isolated sample.*

While a visual inspection of Figure 23 indicates truncation of some NGC 5846 galaxies, a more quantitative approach to determine truncation can be calculated by dividing the star formation radius, r_{17}, by r_{24}. If this ratio is less than 1, then the star formation region is smaller than the optical extent. To be conservative we classify any galaxy with a r_{17} to r_{24} ratio of less than 0.5 as truncated. Table 4 shows this ratio for the NGC 5846 sample.

With our defined truncated ratio, we see that ACG 250105, 9655, 241018, 241022, 254078, and 251419 are all truncated. Figure 24 shows a histogram of the r_{17} to r_{24} ratio for our sample of NGC 5846 galaxies. From Figure 24 it is apparent that the sample includes both truncated and non-truncated galaxies. Also, many of the galaxies in the sample have an r_{17} to r_{24} ratio of between 0.5 and 0.6.

Galaxy	r_{24} (arcsec)	r_{17} (arcsec)	r_{17}/r_{24}
9746	37	32	0.86
9751	16	N/A	N/A
9760	11	9	0.82
252399	12	12	1.00
250105	20	10	0.50
250103	22	12	0.55
252555	19	17	0.89
252550	6	6	1.00
9573	37	29	0.78
9574	53	57	1.08
243743	11	8	0.73
9645	95	56	0.59
9655	160	28	0.18
9661	37	26	0.70
241018	25	8	0.32
241022	38	16	0.42
254078	8	4	0.50
9787	22	12	0.55
243026	13	8	0.62
251419	17	5	0.29
252211	19	11	0.58
252519	14	17	1.21
241031	17	10	0.59

Table 4: *The ratio of r_{24} to r_{17} is examined in order to help classify which galaxies are truncated. Note that the r_{17} of AGC 9751 was not calculated by the photometry program due to the galaxy's edge on nature and faint Hα emission.*

3.7. Imaging Using 4 Dithers vs. 5 Dithers

As explained in Section 2.2, the MOSAIC images were obtained through the use of taking several images, called dithers, that were offset and then stacked. Typically, this process uses 5 dithers to create the final image. Since it is not unusual that one image has defects or is unusable (for example problems with the guide star during the 20 to 30 minute Hα exposures), investigating the possibility of MOSAIC imaging with 4 dithers is a useful idea. Additionally, if imaging with 4 dithers is practical, then observation time could be reduced. Since one of the

dithers in the most recent night of KPNO observing had much worse seeing (see Table 5) these observations presented an opportunity to experiment with imaging using just 4 dithers. The procedure outlined in Section 2 was done twice on the Field 4 images, once using the standard method with 5 dithers, and once using just the 4 dithers of best seeing. Please note that all results in other sections were obtained from photometry base on the images created using the standard 5 dither process.

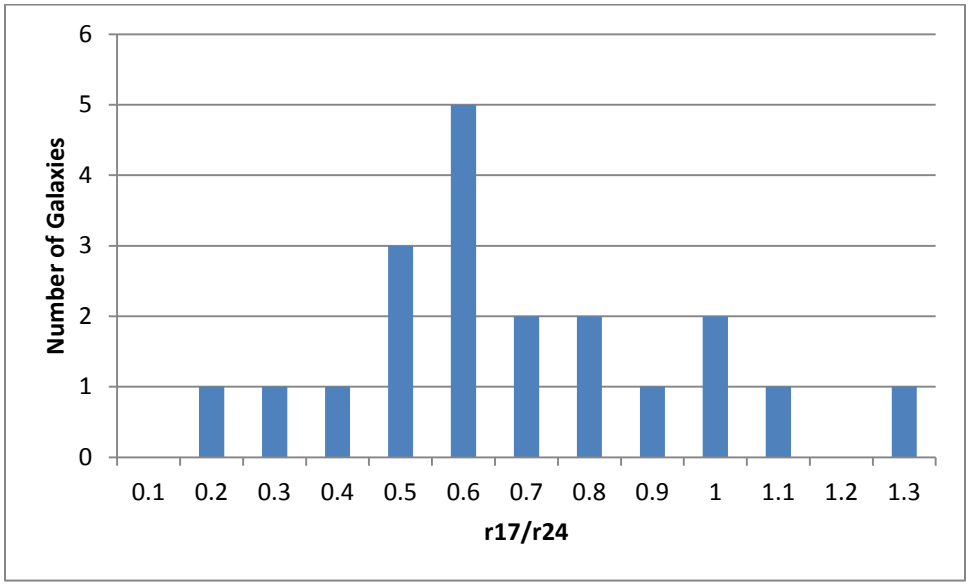

Figure 24: *A histogram for the r_{17} to r_{24} ratio. The lower the value, the more truncated a galaxy's star forming disk is.*

Galaxy AGC Number	Seeing (arcsec)		Sky Uncertainty R (counts)		Sky Uncertainty Hα (counts)		Standard Deviation R (counts)		Standard Deviation Hα (counts)	
	4 Dither Image	5 Dither Image	4 Dither Image	5 Dither Image	4 Dither Image	5 Dither Image	4 Dither Image	5 Dither Image	4 Dither Image	5 Dither Image
252211	3.7	4.7	5	4	2	3	3.8	2.4	2.6	1.8
252519	3.7	4.8	5	4	4	2.5	4.1	2.8	2.7	2.0
241031	3.9	4.9	6	5	4	3	6.0	3.8	3.2	2.3

Table 5: *The seeing, sky uncertainty, and standard deviation is compared for the images created with 4 dithers and the images created with 5 dithers.*

As, expected, the images made from the 4 dithers have better seeing, since they were created by stacking the 4 dithers of the best seeing. However, the uncertainty in the sky background is higher for the 4 dither images (for the R filter) and in both the R and Hα filter the

standard deviation is higher for the 4 dither images. This is also an expected result. Since the 4 dither image has less exposure time, then the signal to noise ratio should be lower (more noise per signal). The longer the total exposure time of the final stacked image, the higher we would expect the signal to noise ratio to be. So, it is not surprising that in each of the images the 4 dither image had a higher standard deviation. Additionally, while each of these three galaxies came from the same 1 square degree MOSAIC images, they all have slightly different seeings due to the fact that for a CCD chip the size of MOSAIC the seeing will vary across the field.

Tables 6 and 7 show the basic photometry results for each galaxy, comparing the images made by stacking 4 dithers and the images made by stacking 5 dithers.

Galaxy AGC Number	r_{24} (arcsec) (4 dithers)	r_{24} (arcsec) (5 dithers)	Total R Flux (4 dithers) (x 10^{-18} erg cm^{-2} s^{-1})	Total R Flux (5 dithers) (x 10^{-18} erg cm^{-2} s^{-1})	R radius (arcsec) to 5 σ (4 dithers)	R radius (arcsec) to 5 σ (5 dithers)	C_{30} (4 dithers)	C_{30} (5 dithers)
252211	19	19	(1.93±0.02)x10^6	(1.86±0.01)x10^6	20.2	21.8	0.29	0.30
252519	14	14	(0.88±0.01)x10^6	(0.85±0.01)x10^6	14.4	15.9	0.18	0.19
241031	17	17	(3.12±0.01)x10^6	(3.16±0.01)x10^6	15.5	16.5	0.47	0.49

Table6: *The r_{24} values, total R flux, R radius out to 5 sigma, and concentrations for each galaxy and for each method of stacking.*

Galaxy AGC Number	r17 (arcsec) (4 dithers)	r17 (arcsec) (5 dithers)	Total Hα Flux (x 10^{-18} erg cm^{-2} s^{-1}) (4 dithers)	Total Hα Flux (x 10^{-18} erg cm^{-2} s^{-1}) (5 dithers)	Log(SFR) (M_{solar}/year) (4 dithers)	Log(SFR) (M_{solar}/year) (5 dithers)
252211	11	11	(2.0±0.3) x10^4	(1.9±0.4) x10^4	-1.794	-1.831
252519	16	17	(6.5±0.6)x10^4	(6.8±0.5) x10^4	-1.290	-1.272
241031	10	10	(3.2±0.8) x10^4	(2.6±0.7)x10^4	-1.300	-1.390

Table 7: *The total Hα fluxes and star formation rates for each of the galaxies and for each method of stacking the images.*

As seen in Tables 6 and 7, for each method of stacking, the value of r_{24} was the same, r_{17} was identical in 2 of the galaxies and only differed by 1 arcsecond in the third galaxy, and the values for C_{30} were also very similar. For the total R flux, AGC 252211 and 252519 have higher fluxes for the 4 dither image, with percent differences of 3.6% and 3.4% respectively. AGC 241031 had a higher R flux for the 5 dither image, with a percent difference of 1.3 percent. For

the Hα flux, the calibration scale factors were the same in each image and the Hα flux values calculated using 4 dithers and 5 dithers were the same within the range of uncertainty.

With regards to the star formation rates, AGC 252211 and 241031 have higher star formation rates for the images created by stacking 4 dithers while AGC 252519 has a higher star formation rate for the image created using 5 dithers (yet since SFR is based on Hα flux, these values are also both acceptable). As mentioned previously, this analysis is complicated by the large amount of error involved in Hα continuum subtraction (see Waller 1990 references in Section 2.3).

For each galaxy, radial profiles were made, examining the surface brightness as a function of radius for the R and Hα continuum subtracted images. Figure 25 compares the radial profiles made using 5 dithers and the profiles made using 4 dithers.

It does not appear that there is any significant differences in the overall shape or extent of the radial profiles in R or Hα. Additionally, the photometry results are comparable, with r_{24} values being the same, C_{30} values being nearly identical, Hα and R fluxes are comparable, and the star formation rates are similar using either method. Therefore, based on this small sample size, imaging with 4 dithers instead of 5 appears to be a reliable method and can yield higher resolution. While the sample size was too small to be conclusive, the results are promising and merit further study.

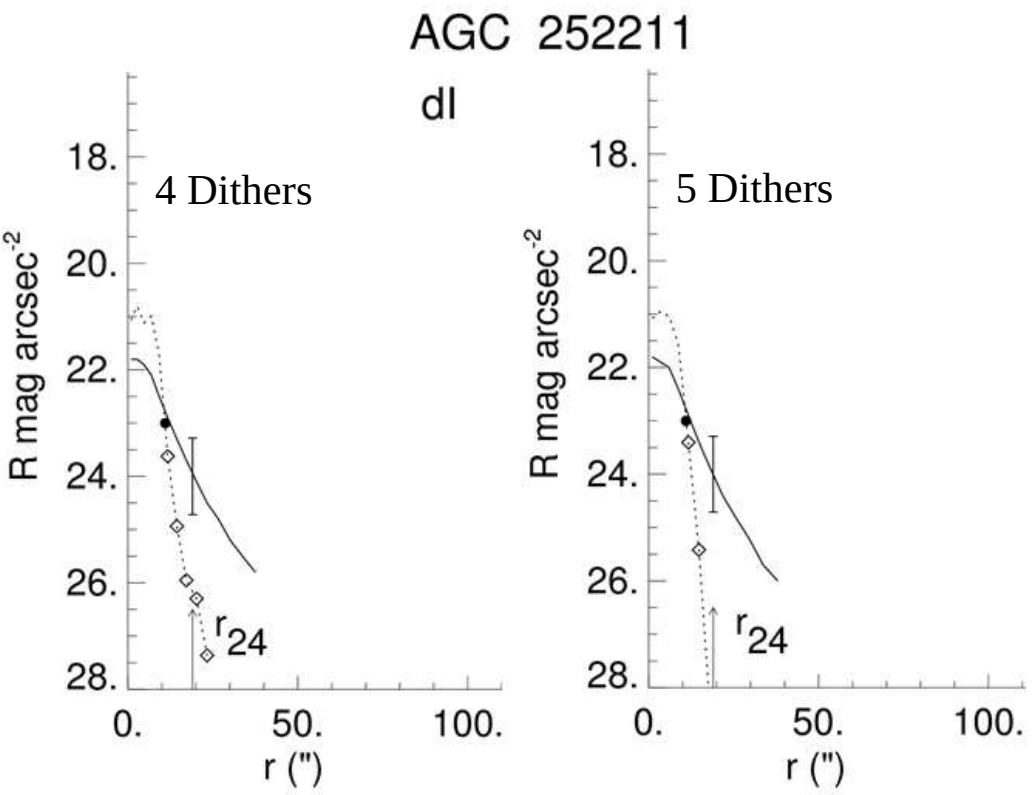
AGC 252211
dI
4 Dithers
5 Dithers
R mag arcsec^{-2}
18.
20.
22.
24.
26.
28.
0.
50.
100.
r (")
r_{24}

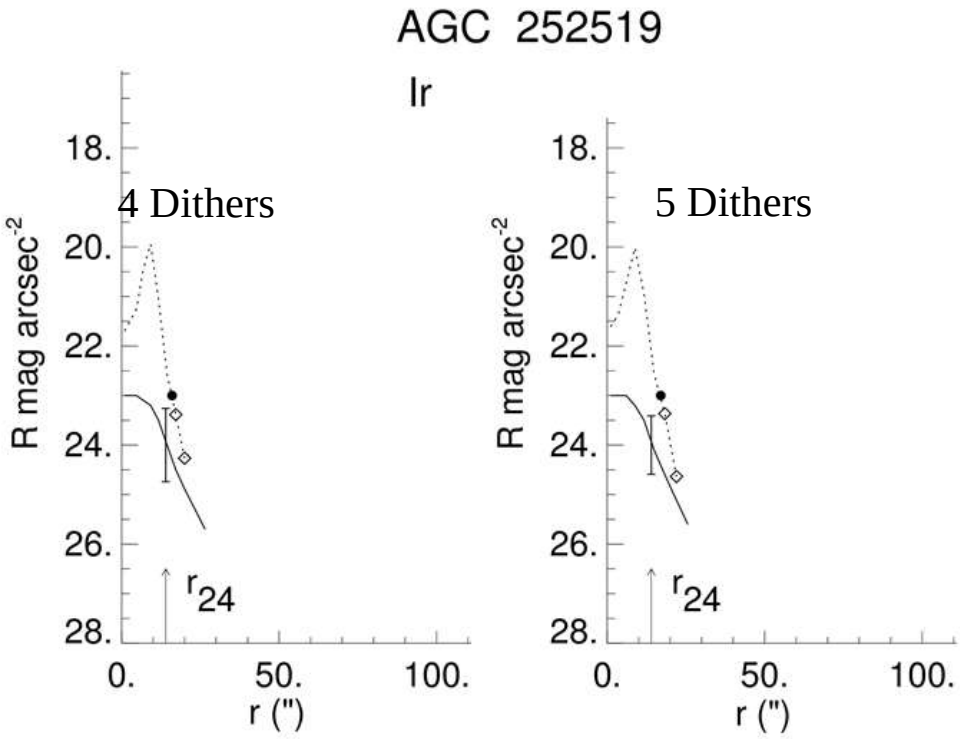
AGC 252519
Ir
4 Dithers
5 Dithers
R mag arcsec^{-2}
18.
20.
22.
24.
26.
28.
0.
50.
100.
r (")
r_{24}

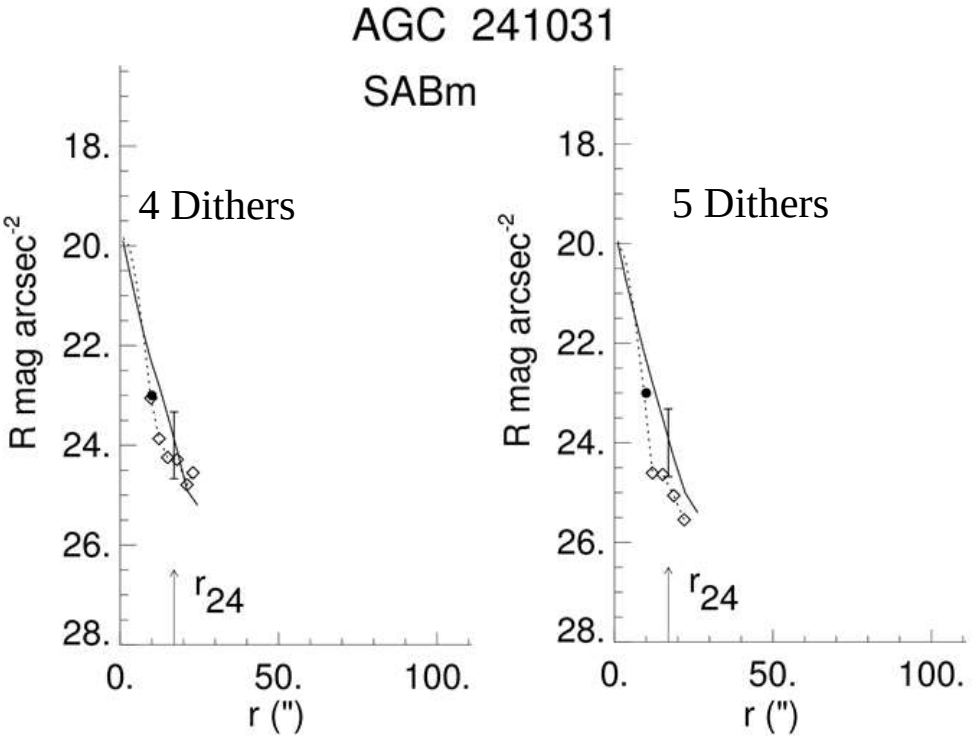

Figure 25: *Radial Profiles Comparing the Different Stacking Methods*

4. Conclusion and Discussion

The results in Section 3 allow us to reach several conclusions regarding the star formation properties of NGC 5846 group galaxies. For much of our sample star formation rates were lower than those found in isolated galaxies (from the van Zee et al. 2001 sample) and more similar to galaxies in the Centaurus A group (from the Cote et al. 2009 sample). There were however, some galaxies with enhanced star formation rates, possibly caused by tidal interactions.

By comparing our NGC 5846 galaxies to isolated galaxies and Virgo Cluster galaxies (from the Koopmann & Kenney 2004 sample) we also see evidence of truncated star forming disks. This truncation is also evident through visual examinations of the R and Hα images and radial profiles, as well as through a comparison of r_{17} and r_{24}. These results indicate that the intragroup medium may be having an effect on star formation of the NGC 5846 group galaxies. Additionally, star formation rates and HI deficiency appear to be independent of a galaxy's

distance from the center of the NGC 5846 group. It is also worth noting that AGC 9655 appears to have some sort of outflow, possible AGN activity.

The Hα detection rate for the sample is also of interest. Of the KPNO fields, only 32% of the galaxies in the main group area are detected in Hα, while the rest have ceased star formation. While this is not unexpected given the fact that the NGC 5846 group has such a high percentage of early type galaxies, some process had to cause this high proportion of early types. The objects that have been classified as early type may have been designated as early type due to this lack of star formation activity (Koopmann & Kenney 1998). The truncation of early type star formation disks supports the possibility of incorrect classification. Therefore, future work should carefully investigate the galaxies without star formation (looking at properties such as concentration) and determine if their stellar distributions are more similar to early type or late type galaxies. The dwarf galaxies should also be investigated to better understand why clusters and dense groups have high dE populations and how these dE galaxies form. It would be useful to compare the NGC 5846 dE population to other dE populations and investigate the role of the group environment.

Future goals of this research include investigating 3 other fields that have been observed in the outskirts and surroundings of NGC 5846 and comparing the more complete sample to other groups, with the goal of better characterizing the radial star formation properties of the low-mass galaxies in group and more isolated environments. It might also be of interest to investigate the relationship between star formation rate and distance to the nearest neighbor. Additionally, comparing our group results to other galaxy groups being investigated by members of the UAT will help confirm if our findings are typical of galaxy groups.

5. Acknowledgements

I would like to thank Dr. Koopmann and Dr. Marr for agreeing to be my thesis readers and editors, the members of the UAT, especially Benjamin Hendrickson, whose instructions were used to reduce the MOSAIC data, my Union College collaborators Katie O'Brien, Halley Darling, and Michael Warrener, and Ryan Muther whose computer programs made the reduction process much smoother. I would also like to thank Union College for the facilities and resources I used to conduct this research, the ALFALFA Team, and the Undergraduate ALFALFA Team.

6. References

Baldwin, J. A., Phillips, M. M., & Terlevich, R. 1981, PASP, 93, 5
Bauer, A. E., Drory, N., Hill, G. J., & Feulner G. 2005, ApJ, 621, L89
Boselli, A., & Gavazzi, G. 2006, PASP, 118, 517
Buat, V., Boissier, S., Burgarella, D., Takeuchi, T. T., Le Floc'h, E., Marcillac, D., Huang, J., Nagashima, M., & Enoki, M. 2008, A&A, 483, 107
Bundy, K., Ellis, R. S., Conselice, C. J., Taylor, J. E., Cooper, M. C., Willmer, C. N. A., Weiner, B. J., Coil, A. L., Noeske, K. G., Eisenhardt, P. R. M. 2006, ApJ, 651, 120
Bushouse, H. 1985, NOAO Newsletter, No. 4, p. 14
Catinella, B. et al. 2010, MNRAS, 403, 683
Cavagnolo, K., Donahue, M., Voit, M., & Sun, M. "ACCEPT: Archive of Chandra Cluster Entropy Profile Tables" Michigan State University. 2009. <http://www.pa.msu.edu/astro/MC2/accept/>
Cote S., Draginda, A., Skillman, E. D., Miller, B. W. 2009, AJ, 138, 1037
Cowie, L. L., Songaila, A., Hu, E. M., & Cohen, J. G. 1996, AJ, 112, 839
Darling, H. 2013 Union College Senior Thesis
Dressler, A. 1980, ApJ, 236, 351
Gavazzi, G. 1987, ApJ, 320, 96
Gavazzi, G. 1989, ApJ, 346, 59
Gavazzi, G., Catinella, B., Carrasco, L., Boselli, A., & Contursi, A. 1998, AJ, 115, 1745
Giovanelli, R., et al. 2005, AJ, 130, 2598
Giovanelli, R., et al. 2005, AJ, 130, 2613
Giovanelli, R., Haynes, M. P. 1985, ApJ, 292, 404
Gunn, J. E., & Gott, J. R. 1972, ApJ, 176, 1
"Halpha Observations". ALFALFA Ugrad Groups. Feb. 24, 2014, Site Visited March 2014 <sites.google.com/site/alfalfaugradgroups/halpha-observations>
Hamuy, M., Walker, A.R., Suntzeff, N.B., Gigoux, P., Heathcote, S.R., & Phillips, M.M. 1992, PASP, 104, 533
Haynes, M. P., & Giovanelli, R. 1986, ApJ, 306, 466
Hendrickson, Ben and Dr. Adriana Durbala. "H-α Reduction of Mosaic 1.1 Images in IRAF's MSCRED Package". University of Wisconsin-Stevens Point.
Huang, S., Haynes, M. P., Giovanelli, R., Brinchmann, J., Stierwalt, S., & Neff, S. G. 2012, AJ,

143, 133
Hubble, E. P. 1926, ApJ, 64, 321
Hunter, D. A., & Elmegreen B. G. 2004, AJ, 128, 2170
Karachentsev, I. D., et al. 2007, AJ, 133, 504
Kenney, J. D. P., van Gorkom, J. H., Vollmer, B. 2004, AJ, 127,3361
Kennicutt, R. C., Jr. 1983, AJ, 88, 483
Kennicutt, R. C., Jr. 1998, ARA&A, 36, 189
Koopmann, R. A., & Kenney, J. D. P. 1998, ApJ, 497, L75
Koopmann, R. A., & Kenney, J. D. P. 2004, ApJ, 613, 851
Koopmann, R. A., & Kenney, J. D. P. 2006, ApJ, 162, 97
Koopmann, R. A., Kenney, J. D. P., Young, J. 2001, ApJ, 135, 125
Larson, R. B., Tinsley, B. M., & Caldwell, C. N. 1980, ApJ, 237, 692
Licquia, T., & Newman, J. 2013, Bulletin of the American Astronomical Society: AAS Meeting #221, #254.11
Loveday, Jon. "Astronomical Techniques: Lectures 2&3: Flux Measurement", University of Sussex, Dept. of Physics and Astronomy, Autumn 2007, Site Visited March 2014, <http://www.phys.susx.ac.uk/~loveday/astroTech/lect2_3.pdf>
Mahdavi, A., Trentham, N., Tully, R. B. 2005, AJ, 130, 1502
Massey, P., Strobel, K., Barnes, J. V., & Anderson, E. 1988, ApJ, 328, 315
Mulchaey JS, Davis DS, Mushotzky RF, Burstein D. 1993. ApJ. 404:L9-12
Muther, R. Union College Summer Research Paper (and python programs)
O'Brien et al. 2011, Bulletin of the American Astronomical Society, 43, #149.28
O'Brien, K. 2012 Union College Senior Thesis
"The Hubble Tuning Fork". Sloan Digital Sky Survey / SkyServer, Site Visited March 2014 <http://cas.sdss.org/dr3/en/proj/advanced/galaxies/tuningfork.asp#endoftable>
Toomre A. & Toomre J. 1972, ApJ, 178, 623
van den Bergh, S. 2000, AJ, 119, 609
van der Marel, Roeland P., "The Large Magellanic Cloud: Structure and Kinematics", Space Telescope Science Institute April 8 2004. Site Visited March 2014 <http://www.stsci.edu/~marel/pdfdir/LMC_maysymp03_vdm3.pdf>
van Zee, L. 2001, AJ, 121, 2003
Waller, W. H. 1990, PASP, 102, 1217
Warrener, M. Union College Summer Research Paper